This electronic thesis or dissertation has been downloaded from Explore Bristol Research, http://research-information.bristol.ac.uk

Author:
Bain, Matthew

Title:
Exploring novel excited state dynamics using multi-mass ion imaging and universal ionisation

Exploring novel excited state dynamics using multi-mass ion imaging and universal ionisation

Matthew Bain

A dissertation submitted to the University of Bristol in accordance with the requirements for award of the degree of Doctor of Philosophy in the School of Chemistry, Faculty of Science.

August 2019

University of BRISTOL

School of Chemistry

University of Bristol

United Kingdom

Dedicated to my grandparents, Andy, Elsie, Kate and Hector.

Abstract

Velocity map imaging has been coupled to the Pixel Imaging Mass Spectrometery camera to enable cutting edge multi-mass imaging experiments to be performed following pulsed laser excitation of jet-cooled gas phase molecular samples. These experiments exploit different forms of universal ionisation to make novel measurements of molecular dynamics or as an ultrafast diagnostic of molecular structure.

Single photon ionisation using vacuum ultraviolet photons is investigated as a method of universal ionisation and a comparison is made with traditional resonance enhanced multiphoton ionisation methods which are fragment and state selective. The method is benchmarked on the photolysis of dimethyl sulfide at 227.5 nm, successfully demonstrating the simultaneous detection and imaging of both fragments (methyl and methyl sulfide) and the effects of space charging, dissociative ionisation and photofragment angular alignment are discussed.

The multi-mass imaging capabilities are then utilised in conjunction with single photon ionisation to investigate the excited state dynamics of an asymmetric thioether t-butyl methyl sulfide wherein all four primary fragments are imaged in a single experiment. This reveals that the competition between dissociation of the two C–S bonds in the excited state is twice as likely to proceed via fission of the t-butyl–S bond at an excitation wavelength of ~ 225.0 nm. Further investigation of the potential energy surfaces imply that this is most likely dominated by non-adiabatic coupling between excited states.

Strong field ionisation is then used as the basis for a Coulomb explosion imaging experiment. The dynamics of ground state Coulomb explosions in methyl iodide, trifluoro methyl iodide and 2-bromothiophene are investigated and the recoil frame covariance analysis technique is employed to correlate the ion trajectories and back out the neutral structure. This sets up future experiments to investigate the evolution of molecular structure on excited states.

Acknowledgements

First and foremost I would like to thank my supervisor Mike Ashfold for his mentorship and friendship over the last four years. I've thoroughly enjoyed my time working with Mike at Bristol (even when he enlists me to help him paint the office!) and I know I will continue to benefit from his tutelage and wise words in the future.

I would also like to thank Chris Hansen who has been instrumental in me reaching the end of my PhD. Chris was a wonderful postdoc to work with in the lab who constantly inspired me with his work ethic, enthusiasm, and ability to turn a phrase! However, he has also been an incredible friend outside of work and I'm so glad that we've had the opportunity to get into all of these crazy adventures together, perhaps most notably the bag of mystery tea in Delhi.

My deepest thanks go to Luke Hedley and Ross White who I am incredibly fortunate to count as my closest friends and confidantes. It is difficult to overstate the impact they've had on my life or put into words how much our friendship means to me as we've been through so much together. Here's to more lasagna, more gigs, and fewer theses to write!

I must also thank Alison Campbell and Melanie Hedley for their friendship and for making visits back to Edinburgh extra fun!

Special thanks are due to Mitch Quinn, there are very few people who could share both a workplace and an apartment yet, somehow, we managed! I'm incredibly grateful for his unwavering support, especially when times were tough where he

demonstrated his quality as a friend.

I owe a great deal of thanks to Tom Oliver. Not only for his help and advice with my experiments and calculations, but also for his friendship and for supporting and encouraging me when I was ready to give up. I'm extremely grateful.

Thanks are also due to Andrew Orr-Ewing and Colin Western for all the insight and advice you've given me during my PhD and for what must now be well into the hundreds of pints you've bought me and the rest of the group on Friday evenings.

Thank you to Philip Coulter and Rabi Chhantyal-Pun, for being my first flatmates in Bristol. I have many fond memories throwing around frisbees and rugby balls at Durdham Court.

During my PhD I've been fortunate to be surrounded by friends who have enriched my time in Bristol. In no particular order I'd like to thank:

Marta Duchi, for making the laser group infinitely cooler with her very presence!

Victoria Taylor, for making working on Sundays much more pleasant with tea and biscuits.

Giordano Amoruso for being the kind of friend who stays out long enough on a Friday to watch the sunrise with cold chips.

Luke Lewis-Borrell, for keeping me company in the office on too many Saturday nights - usually with Oowee!

Becca Walters, for constantly and without fail making me double over with laughter.

Craig Weir, for the great gigs, good food, and the strangest guest singers!

Maev Moran, for making wonderful memories with me during my time in Bristol and for her incredible support during my PhD. I will forever be grateful.

Ben Carwithen, for being the best Masters student I could have asked for. He made the end of my time in lab as a graduate student much more fun and exciting.

I've had the privilege to share my time in the Bristol Laser Group with a superb group of PhD students and postdocs. Tolga Karsili, Hugo Marroux, TJ Preston, Michael Grubb, Balazs Hornung, Katharina Roettger, Daisuke Koyama, Graham Cooper, Subhrangshu Pandit, Barbara Marchetti, Stuart Crane, Xu-Dong Wang,

Author's Declaration

I declare that the work in this dissertation was carried out in accordance with the requirements of the University's *Regulations and Code of Practice for Research Degree Programmes* and that it has not been submitted for any other academic award. Except where indicated by specific reference in the text, the work is the candidate's own work. Work done in collaboration with, or with the assistance of, others is indicated as such. Any views expressed in the dissertation are those of the author.

SIGNED: ...██████████████████....   DATE: ......3 / 12 / 2020......

Contents

List of Figures

List of Tables

Chapter 1

Introduction

1.1 Photochemistry

Molecular processes driven by light are important throughout the natural world. These processes determined the molecular fragments that composed the prebiotic soup,[1] support life in the the plant world though photosynthesis,[2] and enable our ability to view our surroundings with the eye.[3] It is desirable to develop a rich understanding of the underlying photophysics of these processes so that we might detect early signs of life on other planets or learn from the extremely high efficiency processes nature has perfected to incorporate in synthetic molecular design[4] and solar light harvesting.[5]

Following absorption of light, there are a variety of pathways available through which a molecule might rid itself of the excess energy gained. It may simply eject the energy as light, relax non-radiatively by dissipating its energy into the surroundings through intermolecular collisions or dissociating into smaller fragments. The complex competition between these pathways (as well as between the multiple different sub-pathways) is challenging to unravel, scaling exponentially with the size of the molecular structure. The gas phase provides a thorough testing ground for prototypical photophysical systems wherein possible collisional non-radiative relaxation pathways are closed off by the absence of solvent molecules. This allows exquisite investigation of how molecules explore potential energy surfaces uninhibited by intermolecular interactions.

The focus of this thesis is on bond cleavage as a means of energy dissipation in a so called "photodissociation". While photodissociation is a topic which has been thoroughly investigated, this thesis aspires to present novel experimental approaches
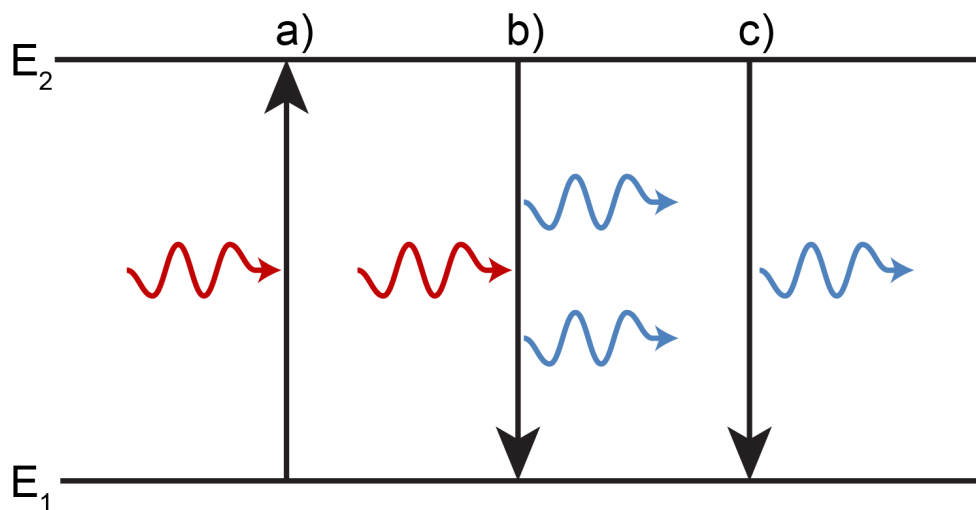
Figure 1.1: Illustration of the three radiative processes associated with photons interacting with a two level system a) photon absorption, b) stimulated emission, and c) spontaneous emission.

to characterise aspects of photodissociation, such as the competition between two bonds to cleave, or non-fragmenting dissociation processes (such as a molecular ring opening) which have been long term challenges for the molecular dynamics community.

1.2 Background Concepts

1.2.1 Light–Matter Interactions

The radiative transfer of population between two arbitrary molecular states by interaction with a photon can occur via three principal mechanisms as illustrated in figure 1.1. These three pathways - a) Absorption, b) Stimulated Emission, and c) Spontaneous Emission - can each be described as a change in population of state n_1 as a function of time as shown in equation 1.1 where $\rho(\nu)$ is the energy density of the incident light, n_{m} is the population of the mth state and A and B are the so-called Einstein A and B coefficients. The absorption and stimulated emission processes are both driven by interaction with a photon which has an energy tuned to the difference

between the energies of the relevant states 1 and 2 (E_2 - E_1).

$$(\tfrac{dn_1}{dt}) = -B_{12}n_1\rho(v) \qquad (\tfrac{dn_1}{dt}) = B_{21}n_2\rho(v) \qquad (\tfrac{dn_1}{dt}) = A_{21}n_2$$
$$\text{Absorption} \qquad \text{Stimulated Emission} \quad \text{Spontaneous Emission}$$

(1.1)

In the stimulated emission process, the incoming photon is not absorbed but interaction of the electric field of the photon with the dipole of the molecule induces emission. The dependence on the incoming photon ensures that the emitted photon will propagate in the same direction and with a defined phase relationship with the incoming photon. This will be important later on when discussing laser theory in section 1.2.6. If an electronically excited system is allowed to exist unperturbed it will eventually relax to its ground state by liberating a photon through spontaneous emission. Unlike stimulated emission, there is no preferential direction for the photons emitted spontaneously and so, across an ensemble of molecules, the distribution of these photons will be isotropic. This also assumes that the timescale for rotation is greater than the timescale for fluorescence which is typical for the types of small molecules studied in this thesis.

The interaction energy (E_{int}) of a system of charged particles with an incoming electric field (typically a photon of light) is given by $E_{\text{int}} = -\mu\cdot\epsilon$, where ϵ is the electric field and μ is the dipole moment of the system given by the sum of all charged particles in the system - $\mu = \sum_i q_i r_i$. In a non-classical picture, where particles described as point charges are acknowledged to be a poor representation for calculating molecular systems, the interaction energy of a given molecule state with the field is given as an expectation value over the wavefunction of the molecular system as shown in equation 1.2.

$$\langle E_{\text{int}} \rangle = \langle \Psi_n | -\hat{\mu} \cdot \hat{\epsilon} | \Psi_n \rangle$$

(1.2)

For a typical excitation photon in the uv or visible region, the wavelength is long on the scale of the molecule (100s of nanometers in contrast to 10s of Angstroms, respectively) and the electric field can be approximated to be constant and so an expression for the expectation value of the dipole can be written as follows.

$$\langle \mu \rangle = \langle \Psi_n | \hat{\mu} | \Psi_n \rangle$$

(1.3)

This expression can then be used for a transition dipole moment, $\langle \mu \rangle_T$, which can be thought of as the strength of the interaction that causes one wavefunction to

be transformed into another. This is extremely similar to the expression for the permanent dipole of a molecule in a given state, shown in equation 1.3, except the integral is between different initial Ψ_i and final states Ψ_f as shown in equation 1.4.

$$\langle \mu \rangle_T = \langle \Psi_f | \, \hat{\mu} \, | \Psi_i \rangle \tag{1.4}$$

1.2.2 The Born–Oppenheimer Framework

Absorption of light in the visible or ultraviolet regime excites electronic transitions in molecules. In principle, a full quantum mechanical treatment would involve constructing a molecular wavefunction $\Psi(\mathbf{r} \, ; \, \mathbf{R})$ which describes both the electronic ($\mathbf{r}$) and nuclear ($\mathbf{R}$) components of a molecular system and interrogating the energy using a molecular Hamiltonian operator as shown in equations 1.5 and 1.6. The wavefunction, when operated on by the Hamiltonian acts as an eigenfunction, with the corresponding eigenvalues manifesting as the observable spectroscopic energy levels (E).

$$\hat{H}\Psi(\mathbf{r};\mathbf{R}) = E\Psi(\mathbf{r};\mathbf{R}) \tag{1.5}$$

$$\hat{H} = \hat{T}_{\mathrm{nuc}}(\mathbf{R}) + \hat{T}_{\mathrm{elec}}(\mathbf{r}) + V(\mathbf{r};\mathbf{R}) \tag{1.6}$$

This operator includes a kinetic energy operator which returns the kinetic energy of all particles in the system ($\hat{T}$ as shown in equation 1.7) and the Coulombic interaction (V as shown in equation 1.8) which describes the interaction between all pairs of charged particles in the system.

$$\hat{T} = -\frac{\hbar^2}{2m}\nabla^2 \tag{1.7}$$

$$V = \frac{q_1 q_2}{4\pi\epsilon_0 r} \tag{1.8}$$

In practice, this is an extremely difficult or potentially impossible equation to solve due to the interdependence of the electronic and nuclear components of the wavefunction. Luckily, the timescales on which the electronic and nuclear wavefunctions respond to changes in the system are very different and so it is a valid assumption that we can separate them out and make the approximation that the electronic wavefunction responds instantaneously to any change in the nuclear wavefunction. This is known as the Born–Oppenheimer (BO) Approximation.[6] As such the total wavefunction $\Psi(\mathbf{r};\mathbf{R})$ can be separated into independent nuclear $\chi(\mathbf{R})$ and electronic $\psi(\mathbf{r};\mathbf{R})$ wavefunctions which can then be substituted into equation 1.5 and expanded

by equation 1.6 to give equation 1.9.

$$\hat{H}\psi(\mathbf{r};\mathbf{R})\chi(\mathbf{R}) = \hat{T}_{nuc}\chi(\mathbf{R}) + \left(\hat{T}_{elec}\psi(\mathbf{r};\mathbf{R}) + V(\mathbf{r};\mathbf{R})\psi(\mathbf{r};\mathbf{R})\right)\chi(\mathbf{R}) = E\psi(\mathbf{r};\mathbf{R})\chi(\mathbf{R})$$
(1.9)

This demonstrates that not only is the electronic wavefunction a function of the electron positions and of the nuclear positions as expected, but that the nuclear component of the wavefunction is independent of the $\mathbf{r}$. There is another assumption operating implicitly here which is that the electronic states are adiabatic in nature, or that there is no coupling between the states. This is valid for great swathes of parameter space but certain crucial regions exhibit significant non-adiabaticity and the Born-Oppenheimer approximation breaks down.

1.2.3 Potential Energy Surfaces

One consequence of operating in the Born–Oppenheimer Framework is that we can picture the evolution of electronic energy levels with respect to all of the nuclear degrees of freedom as a smooth-continuous surface - a potential energy surface (PES). At any point on this PES, the negative of the derivative of the energy with respect to nuclear coordinate gives the forces acting on each atom. The simplest example of a photodissociation involves an excitation to a directly dissociative state, as shown in figure 1.2. The energy of the wavefunction associated with the excited state is asymptotically minimised when the molecular fragments are separated thus driving the dissociation.

Energy is, of course, conserved and so in the simple case given for the 'AB' molecule the excitation energy is partitioned entirely into three components: the energy required to overcome the preference for A and B to be bound (the dissociation energy D_0), the kinetic energy of the two fragments (Total Kinetic Energy TKER), and any energy in the internal degrees of freedom of A and B such as rotational, vibrational or electronic excitation energy (E_{int}).
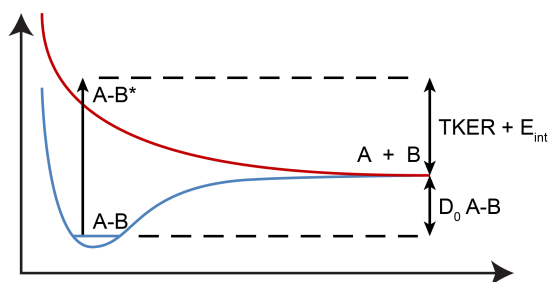
Figure 1.2: A simple direct dissociation following excitation from a bound ground state (blue) to a repulsive excited state (red).

The reality is that the potential energy surfaces which describe a molecule are much more complicated, particularly when bound or quasi-bound excited states are

involved. Many more pathways become available for rearranging the energy, some of which are dependent on the environment of the molecule. Figure 1.3 depicts some of the common pathways and processes that molecules can undertake to rearrange their internal energy. This depiction eschews any description of the shape of the potential energy surfaces. Photoexcitation is restricted to states of the same spin multiplicity
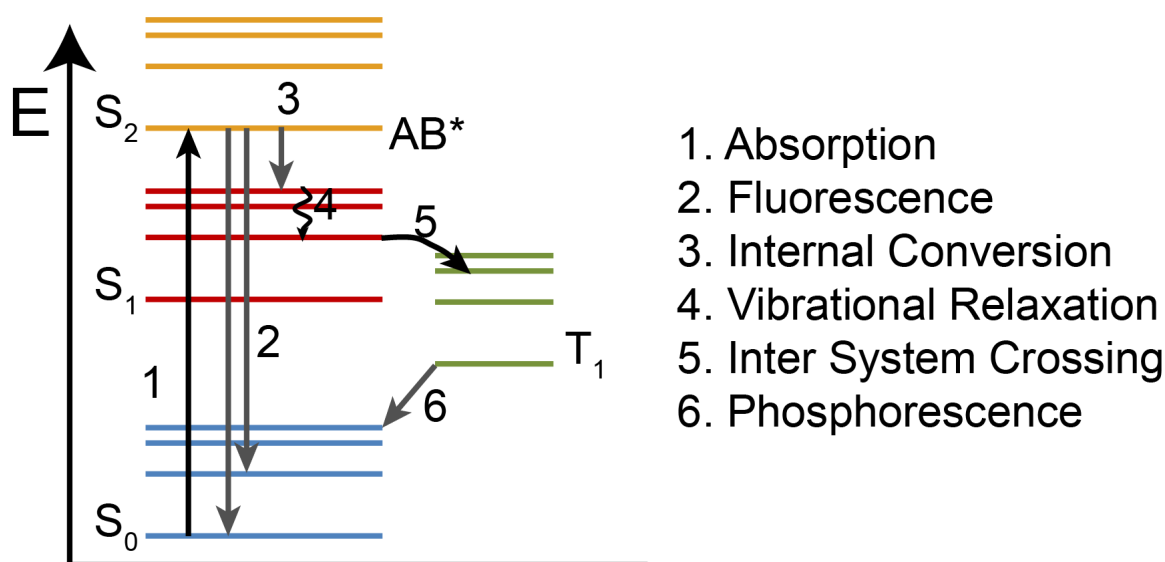
Figure 1.3: A Jablonski diagram showing a variety of possible fates of a molecule following photoexcitation. The grey arrows indicate processes which emit a photon.

(*e.g.* singlet to singlet etc). Without undergoing any rearrangement of nuclear configuration or transitioning to a different electronic state the molecule can spontaneously deexcite to the ground electronic state while releasing a photon of energy. This is known as fluorescence as shown by pathway 2 in figure 1.3. Where potential energy surfaces approach degeneracy, a coupling can occur depending on the symmetry of the two states. If the molecule is excited to a vibrational state above the barrier formed by the state crossing (as shown by the manifold of vibrational states highlighted in purple) then the molecule can predissociate by exploring different potential energy surfaces until it finds a dissociative coordinate into which to irreversibly dispose of its energy as shown in pathway 3.

In the presence of a solvent, vibrational excitation can be relaxed by coupling the energy to the solvent through collisions, this vibrational cooling is shown in pathway 4.

If a bound state exists for a long time then spin flips can occur leading to a crossing to a correlated state, for example conversion from a singlet state to a triplet state in

a process known as inter system crossing as shown in pathway 5. Finally, pathway 6 only opens up following the inter system crossing process, which involves spontaneous emission of a photon as a result of deexcitation from an excited state to a lower state which involves a spin flip, i.e. from a triplet state down to a singlet ground state.

1.2.4 Conical Intersections

As nuclei move, it is possible for electronic states to approach one another to near degeneracy whereupon treatment of the states in isolation (as per the BO approximation) fails to capture the interaction between the two states. In the Born Oppenheimer framework these states are most easily described as the solutions of diagonalising the electronic Hamiltonian to produce two non-interacting diabatic states shown schematically by the blue and red crossing lines in figure 1.4 a) and mathematically in equation 1.10. The eigenvectors $\begin{pmatrix} 1 \\ 0 \end{pmatrix}$ and $\begin{pmatrix} 0 \\ 1 \end{pmatrix}$ return the individual states and no eigenvectors exist which convert one state into the other or represent a mixture of the states.

$$H = \begin{pmatrix} \hat{H}_1 & 0 \\ 0 & \hat{H}_2 \end{pmatrix} \tag{1.10}$$

A model which includes the interaction between the two states provides a better approximation here as it allows funneling of flux from one state to another on an ultrafast timescale. These non-adiabatic couplings are crucial in describing a wealth of fascinating chemistry, for example conical intersections are crucial in the cis-trans isomerisation that mediates vision.[7] The coupling between these states must be de-
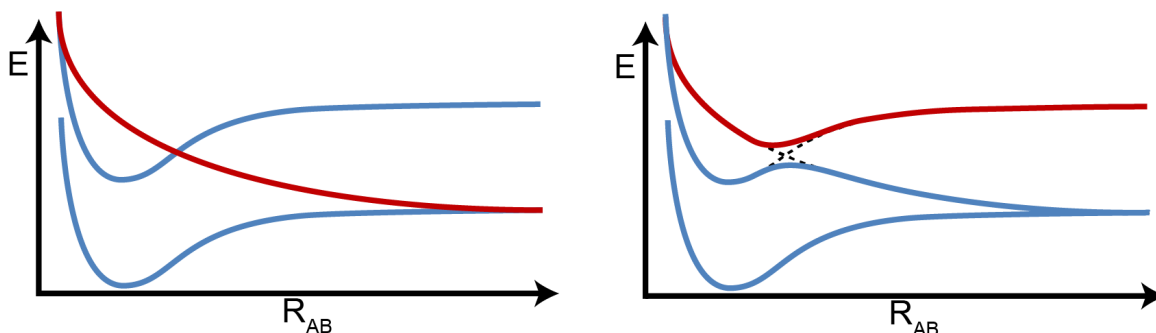
Figure 1.4: Panels a) and b) show diabatic and adiabatic representations of the crossings between two excited states as a function of an arbitrary reaction coordinate. The adiabatic potentials have the non-adiabatic crossings superimposed in dashed lines alongside the coupling between the states.

scribed as a perturbation of the existing adiabatic states as shown in equation 1.11. As the perturbation describes the coupling exclusively, the eigenfunction contains exclusively off-diagonal elements as shown in equation 1.11.

$$\hat{H}^p = \begin{pmatrix} 0 & \hat{H}_{12} \\ \hat{H}_{21} & 0 \end{pmatrix} \tag{1.11}$$

As the diabatic Hamiltonian ($\hat{H}^0$) and the perturbed Hamiltonian $\hat{H}^p$ both operate on electronic wavefunctions they can be summed as shown in equation 1.12.

$$\hat{H} = \hat{H}^0 + \hat{H}^p \tag{1.12}$$

Thus yielding an overall expression for the system $\hat{H}$:

$$\hat{H} = \begin{pmatrix} \hat{H}_{11} & \hat{H}_{12} \\ \hat{H}_{21} & \hat{H}_{22} \end{pmatrix} \tag{1.13}$$

Here the individual expressions $\hat{H}_{ij}$ are the expectation values for the Hamiltonian operating on two states: $\langle \psi_j | \hat{H} | \psi_i \rangle$. Hence, when $i=j$ the expression is equal to the energy of the state, and when $i \neq j$ it is equal to the coupling between the states. This expression for the Hamiltonian now has a new set of eigenvalues as shown in equation 1.14.

$$E_{ij} = \frac{1}{2}(\hat{H}_{ii} + \hat{H}_{jj}) \pm \sqrt{\frac{(\hat{H}_{ii} - \hat{H}_{jj})^2}{4} \hat{H}_{ij}^2} \tag{1.14}$$

Note that when the coupling interaction $\hat{H}_{ij}$ is zero, the eigenfunctions in equation 1.14 are still valid and return the energies of the diabatic states (as shown in figure 1.4 a). As the coupling of the states increases they separate to form an avoided crossing as shown in figure 1.4 b) with the interaction between the states marked by dashed lines. This type of coupling between states is known as a conical intersection. These conical intersections are complex in nature, due to the presence of the character of multiple wavefunctions and represent a region of nuclear space where the Born–Oppenheimer approximation breaks down. This is because the BO approximation assumes that the derivatives of the electronic wavefunction with respect to space are negligible in comparison to those of the nuclear wavefunction. Around a conical intersection however, the highly coupled electronic and nuclear wavefunctions cannot be separated. By describing the adiabatic states in the matrix formalism shown in equation 1.13 and, crucially, separating out the diabatic states and the coupling, the

transition probability between adiabatic states can be calculated by the Landau-Zener formula[8] as shown in equation 1.15.

$$P = \exp\left[-\frac{2\pi E_{12}^2}{\left(\hbar\nu\frac{\partial(E_2-E_1)}{\partial R}\right)}\right]$$

(1.15)

where P is the probability of transitioning non-adiabatically between two surfaces, E_1 and E_2 are the energies of the two diabatic crossing PESs, and v is the velocity along the reaction coordinate.

1.2.5 Uncertainty Principle

To study photoexcitation dynamics effectively, as is the goal of this thesis, molecules must be prepared in either a well defined energetic state, or at a well defined point in time. Although it would be ideal to study a system defined accurately in both energy and time this is well impossible to achieve due to a phenomenon of waves which is dictated by the uncertainty principle as shown in equation 1.16.

$$\sigma_\nu\sigma_t \geq \frac{1}{4\pi}$$

(1.16)

where σ_ν is the uncertainty in the frequency of a photon and σ_t is the uncertainty in the position in time of a photon. There are many ways to think about this phenomenon and a simple interpretation is offered in figure 1.5. The left hand panel shows a series of waves (for example electromagnetic waves) in the time domain, while the right hand panel shows these same waves in the frequency domain, related through the Fourier transform. The temporal and frequency domains are related through the uncertainty principle in equation 1.16. The top five waves are very well defined in the frequency domain, and this manifests as continuous waves in the time domain in which the frequency does not change as a function of time. Here the uncertainty in the time is high and the uncertainty in the frequency of the wave is low. To produce a temporally short wave, waves of different frequency must be added together so that they constructively interfere at one point in time, this is shown by the wave at the bottom of the time panel in figure 1.5. As the temporally short pulse is constructed from waves of a range of frequencies, the Fourier transform signal in frequency space is spectrally broad. Here, the uncertainty in the temporal position of the wave is low and the uncertainty in its frequency is high.
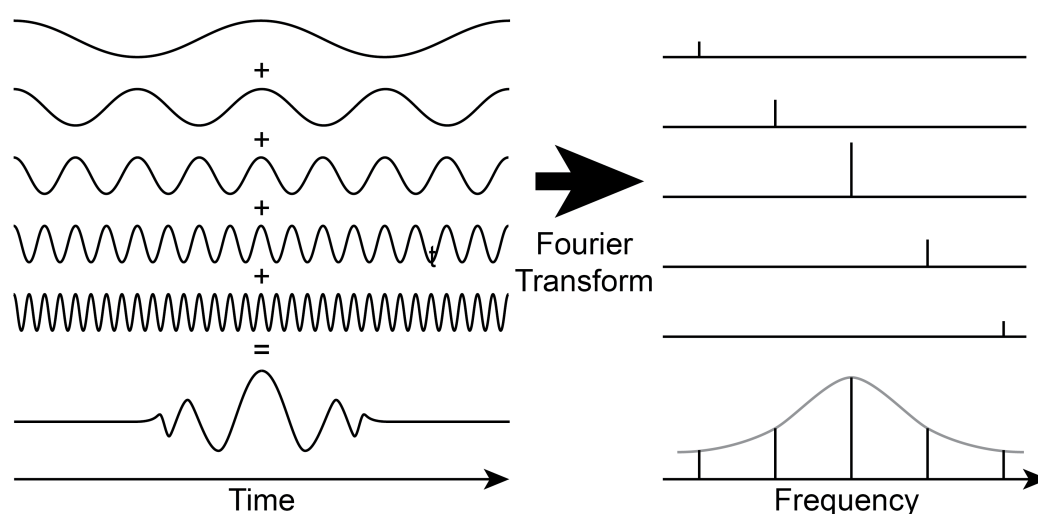
Figure 1.5: Diagrams showing continuous and pulsed waves in time (left panel) and frequency (right panel) domains.

1.2.6 Laser Theory

Lasers are a crucial technology in modern scientific research. They are used in applications as broad as superresolution microscopy - to understand nanoscale structure,[9] ablation to etch surfaces,[10] or spectroscopy to measure the quantum states of a molecule.[11]

A laser is an ideal way to achieve the precise preparation of molecular states or well defined reaction start times necessary to probe dynamics as different types of laser generate temporally short or energetically high resolution laser pulses as the situation requires. This thesis will exploit both regimes of laser for different purposes.

All lasers require a medium in which a population inversion can be created such that when a photon that we desire to amplify interacts with it, the stimulated emission process is dominant. With reference back to Einstein's equations as described in section 1.2.1 this is impossible to create for a two level system because as soon as the system reaches 50% excitation the probability of an incoming photon inducing stimulated emission is exactly as likely as inducing a photoexcitation before even considering the extra effect of spontaneous emission. To overcome this, a multi-level system is desirable. Consider a three level system, as shown in figure 1.6 a). Here, the molecule is excited from state 1 to state 3 upon which the population in state 3 prefers to quickly transfer non-radiatively to state 2, rather than to slowly spontaneously emit down to state 1. Because the non-radiative transfer process from state 2 to state 1 is
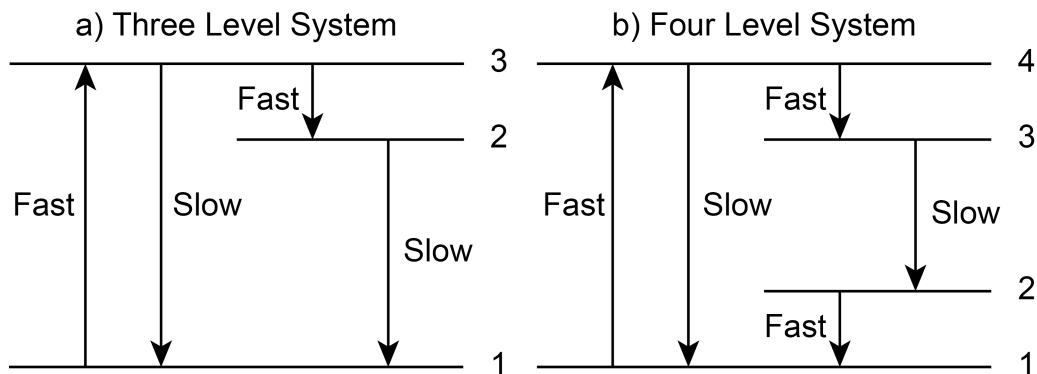
Figure 1.6: Schematic if the a) three level and b) four level systems used to create population inversion for laser gain media.

slow, this creates a population inversion between states 2 and 1 which can be used to amplify light which is energetically tuned to stimulate emission from state 2 down to state 1.

The drawback of this system is that as the stimulated emission process begins, state 1 begins to fill up while the population in state 2 is perpetually replenished by the pump process and so the ratio of population in state 2 to state 1 decreases thus decreasing the rate of stimulated emission in line with the equations in section 1.2.1. This is the mechanism which takes place in chromium ions, which form the basis of ruby lasers.

This is improved upon by a four level system as shown in figure 1.6 b). Here, the initial pumping is identical to the three level system, except that the excitation is from state 1 to state 4 rather than state 3, followed by fast non-radiative relaxation to state 3 rather than state 2. The stimulated emission step begins in the same way, inducing radiative relaxation of the system from state 3 to state 2. However, rather than suffering a build up of population in state 2, there is fast non-radiative process channeling population quickly from state 2 back to state 1 and maintaining the optimum population inversion with respect to states 3 and 2. This is the configuration which dominates modern laser gain media such as neodymium ions or laser dyes.

This allows the light we wish to amplify to be distinct from the generation of the population inversion. For example, the gain medium can be pumped by readily available laser light from a simpler laser system, or by electrical discharge as in an excimer laser. Crucially, the stimulated emission process maps the properties of the light which induces the emission (*e.g.* propagation direction and polarisation vector)

exactly onto the emitted photons. Herein lies the amplification process. Typical laser systems in modern experimental laboratories consist of a variety of lasers coupled together to pump specific gain media and manipulate light pulses to either a very specific wavelength or to be particularly temporally short. Both configurations are employed in this thesis and will be discussed in further detail in chapter 2.

1.2.7 Ionisation of Molecules

The detection and identification of molecules or their fragments has been a continual challenge since the beginning of modern science. This has driven the field of spectroscopy to develop exquisitely sensitive and sophisticated techniques to determine molecular structure such as Nuclear Magnetic Resonance (NMR) or x-ray diffraction as well as absorption techniques in the UV-visible, infrared or microwave regions to fingerprint electronic, vibrational or rotational transitions. This thesis is, as the title suggests, concerned with the dynamics of molecules - that is to say how they move and evolve. As such, the measurement of the ballistic trajectories of a molecule or its fragments is important. Techniques such as those listed above can give information about internal energy distributions but are, for the most part, blind to the dynamics of the system. Measurements of the trajectories of neutral particles are, in general, difficult to make. To overcome this, an effective approach is to ionise the particle and make the assumption that the measurement of the ion trajectory is a good approximation of the neutral trajectory. There are a wealth of techniques suitable for ionising molecules, each with their own features which might be considered either merits or faults depending on the goal.

Resonance Enhanced Multiphoton Ionisation

One of the most commonly applied techniques is resonance enhanced multiphoton ionisation (REMPI).[12] The ionisation potential of most molecular fragments equates to a photon with a wavelength deep into the vacuum ultraviolet ($100 < \lambda < 200$ nm) and so a method which uses less energetic photons is desirable. REMPI methods are a two stage process, the first of which is a resonant excitation to an intermediate state followed by a non resonant absorption into the cation continuum at energies above the ionisation potential. Not only does this use photon wavelengths which are more readily accessible with a bench top laser but also allows population analysis by tuning the resonant step to sample different (ro)vibrational states of the molecules. REMPI processes are notated as (x + y) schemes, where the x value denotes how
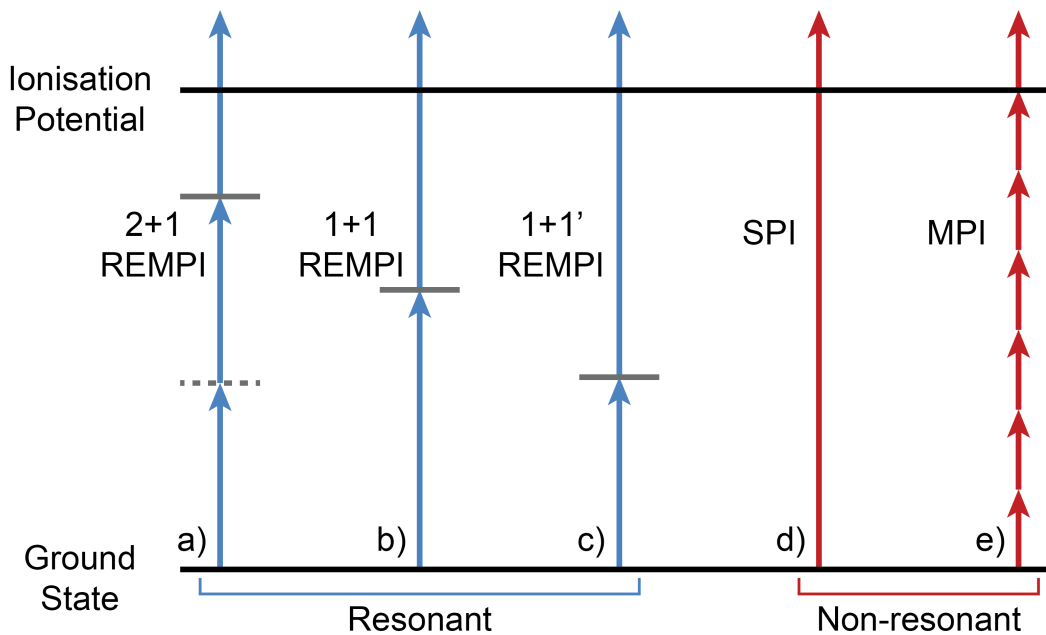
Figure 1.7: Five possible photoabsorptive processes leading to the ionisation of an atom or molecule. The resonant schemes in blue are a) a 2+1 REMPI scheme beginning with a two photon absorption to an intermediate state (in grey) via a virtual state (dashed line) followed by absorption of a third photon which exceeds the ionisation potential. b) A 1+1 REMPI scheme which first absorbs one photon in a resonant process to an intermediate state followed by a second photon of the same frequency to exceed the ionisation potential. c) A 1+1' REMPI scheme in which a photon is first absorbed to an intermediate state which is then ionised by absorption of a photon of a different frequency. The non-resonant schemes in red are d) Absorption of a single highly energetic photon from the ground state directly into the ionisation continuum. e) Absorption of many low energy photons to overcome the ionisation potential.

many photons are involved in the resonant process and the y value denotes how many are involved in the ionisation step. If the wavelength of the y photons is different from that of the x photons then this is denoted by a tick (*e.g.* (2+1')). Figure 1.7 a) - c) show examples of REMPI processes for arbitrary molecular systems. The primary drawback of REMPI processes is that the schemes are molecule specific and the schemes only exist for relatively few, typically small, molecules.

Multiphoton Ionisation

More universal methods of ionisation exist, but generally lose quantum state speci-

ficity. One such method is to subject the molecule to a moderate to high intensity $(10^7 - 10^{13}$ W / cm$^2)^{13;14}$ of visible or infrared light, whereupon the molecule absorbs multiple low energy photons to exceed the ionisation potential.[15] While this is a technique which can universally ionise all molecules, the molecule will absorb a different number of photons depending on which portion of the laser pulse it is subjected to. A molecule in a low energy part of the pulse manifold may barely exceed the ionisation threshold whereas a molecule subjected to the most intense portion of the beam profile might absorb enough photons to undergo dissociation on the cation surface.

Single Photon Ionisation

Single photon ionisation (SPI) involves absorption of a single photon which is sufficiently energetic to overcome the ionisation potential of a fragment in a so called "soft" ionisation. The choice of wavelength can be tuned to overcome the ionisation potential of most molecules or molecular fragments - a particularly handy feature when a laser pulse needs to ionise multiple species simultaneously. The excess energy above the ionisation potential of the molecules is of little consequence as it will primarily be deposited into the kinetic energy of the departing electron. To ionise molecules and molecular fragments using single photons means generating photons in the vacuum ultraviolet - a challenging feat due to their absorption by air. Excimer/exciplex lasers uses rare gases and/or reactive gases which are pumped to excimers or exciplexes by discharging high voltage through the gas before the charge recombination releases a photon. The choice of gas used determines the wavelength of the output. These lasers can generate several, narrowly defined, wavelengths across the VUV but at relatively low photon fluxes.

Vacuum ultraviolet generation in gases can take two forms, either frequency tripling resonantly or non-resonantly,[16–18] or through four wave mixing by exciting a two photon transition and then tuning the third photon to generate a VUV photon by difference frequency mixing (as shown in figure 1.8 a)). In principle, the four wave mixing approach can tune continuously across the VUV by changing the gas mixture but generally has a low flux unless the tuning photon happens to be resonant.[19] VUV generation by frequency tripling can generate high photon fluxes but requires more rigorous conditions to achieve than four wave mixing. The tripling must occur at a frequency where the frequency of the tripled photon (ω_{VUV}) lies slightly to the blue of the resonance peak to exploit the lower refractive index at this point as shown in figure 1.8 b).

a) Four Wave Mixing

b) Frequency Tripling
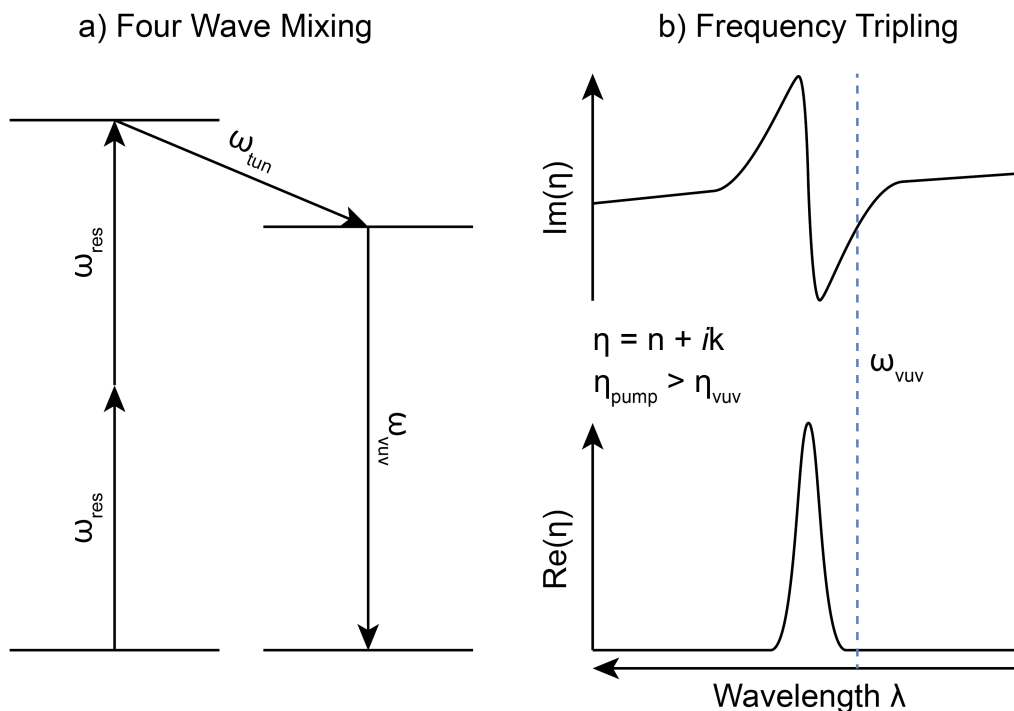
Figure 1.8: The left panel demonstrates a typical scheme for four wave mixing by difference frequency mixing by exciting through a two photon resonance (ω_{res}) before pumping down to a lower state or manifold of states (ω_{tun}). This then relaxes to the ground state by emitting a photon of frequency ω_{VUV}. The right hand panel shows the response of the refractive index of a medium to changing wavelength. The refractive index generally increases as the wavelength decreases but around resonances the refractive index rises on the red side of the resonance and decreases on the blue side with respect to the baseline refractive index. This is a necessary condition for successful third harmonic generation as employed in chapters 3 and 4.

Strong Field Ionisation

When molecules are subjected to extraordinarily intense laser fields ($\sim 10^{15}$ W cm^{-2}), their behaviour in response to the light changes dramatically from that observed in the photoabsorptive processes observed in photoexcitation or REMPI. Instead the dominant effect is a perturbation of the electric fields which define the most probable location for an electron. Figure 1.9 shows an incoming ultrashort laser pulse with an intensity on the order of 500 TW cm^{-2}. In the absence of an external field the electrons are most probably found at some position in the molecule dependent on the interactions with other electrons and nuclei. A simple schematic of this is shown in figure 1.9 a). As the strength of the laser field reaches its apex, the electric fields of the molecule can be sufficiently deformed to allow an electron to tunnel through the

barrier as shown in figure 1.9 b). As the laser field rolls over it temporarily returns to the unperturbed fields as a charged species before the laser field reverses and the electric fields are perturbed in the opposite direction ejecting a second electron as shown in figure 1.9 c) and d). This is a highly efficient way to access highly charged states of atoms or molecules. The propensity for a system to undergo strong field ionisation is described by the Keldysh parameter[20;21] as shown in equation 1.17,

$$\gamma = \sqrt{\frac{E_B}{2U_p}} \tag{1.17}$$

where E_{B} is the binding energy of the most readily removed electron and U_{p} is the "ponderomotive" energy which is a ratio of the intensity of the laser field (I) to twice the frequency of the laser field (ω) squared as shown in equation 1.18.

$$U_p = \frac{I}{(2\omega)^2} \tag{1.18}$$

The propensity for tunnelling increases as $\gamma \to 0$ implying that tunneling is achieved when the binding energy is low, the laser field intensity is high and the frequency of the laser field is low. While the former two conditions are intuitive, the preference for tunneling under low laser field frequencies (or low energy photons) is counter intuitive. This can be explained with reference to the description of the process in figure 1.9. As displayed in panels b) and d), the longer the molecular electric fields spend deformed to the point where tunnel ionisation can take place the higher a chance of an electron tunneling through the barrier.

1.2.8   Velocity Map Imaging

The development of time of flight analysis of molecular photofragments led to a revolution in probing reaction dynamics either following molecular collisions[22] or photodissociation[23]. The translational energy of photofragments can be measured with quantum state specific resolution and the measurements can be made with respect to different orientations of the electric vector of the photoexcitation laser beam to characterise anisotropies in the molecular photodissociation process.[24] These analyses have revealed complex interplay between excited state potential energy surfaces in even the simplest of photodissociations.[25;26] The ion imaging method is an extension to the time of flight mass spectrometry method which projects the three dimensional distribution of the particles coming from a photodissociation down the time of flight
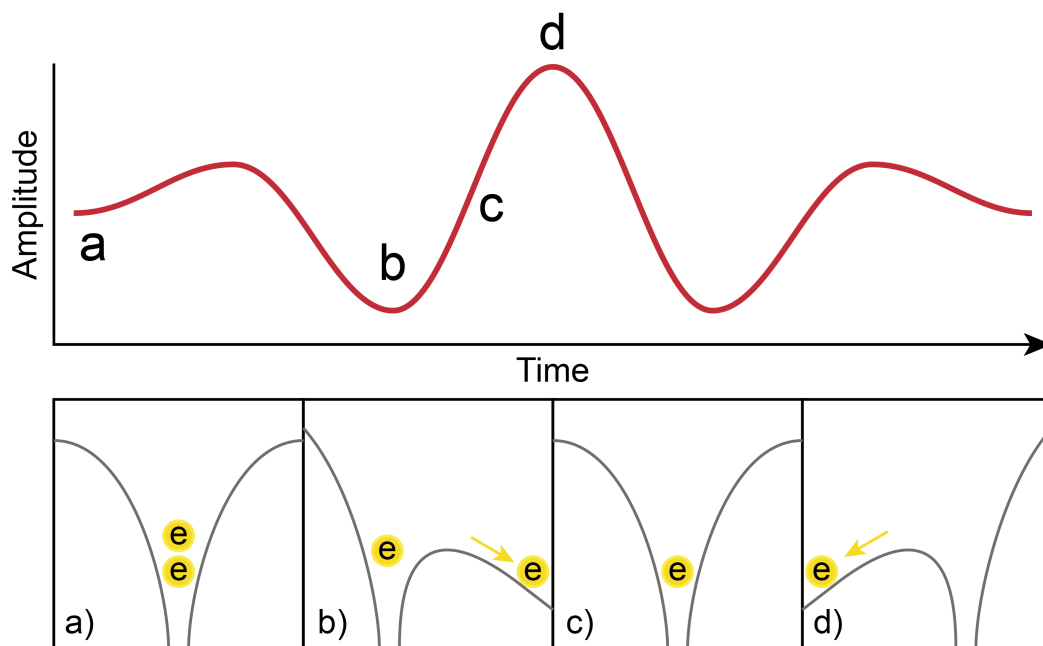
Figure 1.9: The perturbation of the internal electric fields of a molecule under the influence of an extremely strong field laser pulse shown schematically by the red trace. The panels a) - d) show the tunnel ionisation process for two oscillations of the laser field.

axis and onto a two dimensional position sensitive detector.[27] In this set up, the nascent photofragments are ionised by a laser beam. The cations are repelled by a plate held at a bias voltage and accelerated across a potential until they pass a grounding ring electrode into a field free region where they are allowed to further mass separate. The ions then impact on a position sensitive detector where the three dimensional distribution is "pancaked" and imaged by a camera. This allows the retrieval of the speed distribution for each photofragment and the anisotropy of each feature.

The main limit on the resolution of the ion imaging method is the blurring associated with the size of the Newton sphere at the point of ionisation. This is overcome by the Velocity Map Imaging[28] (VMI) method where an extraction electrostatic optic (and an optional focusing optic) is added between the interaction region and the ground electrode. By tuning the ratios of bias voltages applied to the electrodes the fields are shaped into an electrostatic lens which guides the particles in such a way that they are mapped onto the detector according to their velocities regardless of where they originated. This is shown in figure 1.10, the main panel of which shows a cut through the centre of a set of VMI optics extracting particles towards a position sensitive detector. Panel a) shows how the electric fields collect particles regardless of the direction they are ejected from a dissociation event. Panel b) shows the particles being born at three different points in space (represented in three different colours) and the early stages of their trajectories where they are being mapped as a function of their velocity component in the x,y plane. Panel c) shows the latter stage of their trajectories where the particles have coalesced according to their x,y trajectories regardless of their point of origin. The three final trajectories represent i) zero velocity ii) moderate velocity, and iii) the limiting velocity that can be measured by the detector, in the x,y plane.

VMI has been the subject of further modification, for example, by addition of an Einzel lenses to magnify low velocity features,[29] by adding a focusing electrostatic lens to stretch the Newton sphere out along the time of flight axis[30] (see section 1.3.2), or by adaptation to accommodate liquid or solid surfaces off which to scatter molecular beams.[31] Figure 1.11 shows a typical ion image. This particular image corresponds to oxygen atoms which have been ejected from molecular oxygen following absorption of photons of 224.998 nm. Information is contained in both the radial (r) and angular components (θ) of a detected particle as denoted. Here the radial component gives the speed imparted into a particle and, with respect to a constant polarisation of pho-
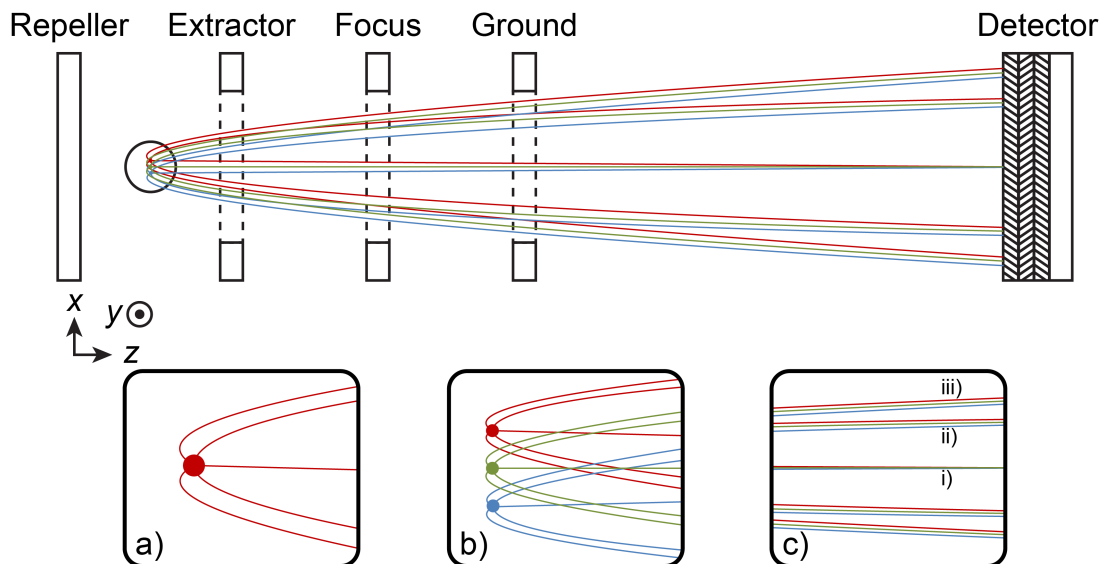
Figure 1.10: The upper picture shows the relative locations of the repeller, extractor, focus and grounding electrodes in a typical velocity map imaging setup as well as the position sensitive detector at the end of the time of flight region. The circle between the repeller and extractor electrodes designates the interaction region where the molecules or fragments are ionised. The horizontal axis is defined as z, the vertical axis as x and the out of plane axis is defined as y in accordance with the key beside the repeller plate. The inset panels show various stages along the ion trajectories to illustrate the velocity mapping process. Panel a) shows the the initial ion trajectories for particles born at a distinct point in the interaction region and how they are all directed towards the detector. In this diagram, the ions are born with three possible perpendicular speeds: high, low, and zero. Panel b) shows the evolution of the ion trajectories starting from different ionisation points and how they begin to coalesce regardless of the point of origin. Panel c) shows the ion trajectories towards the end of their flight paths, where the trajectoreis are well separated according to their perpendicular velocity and the difference in their point of origin manifests as a slight spread in the detection position for a given perpendicular velocity.
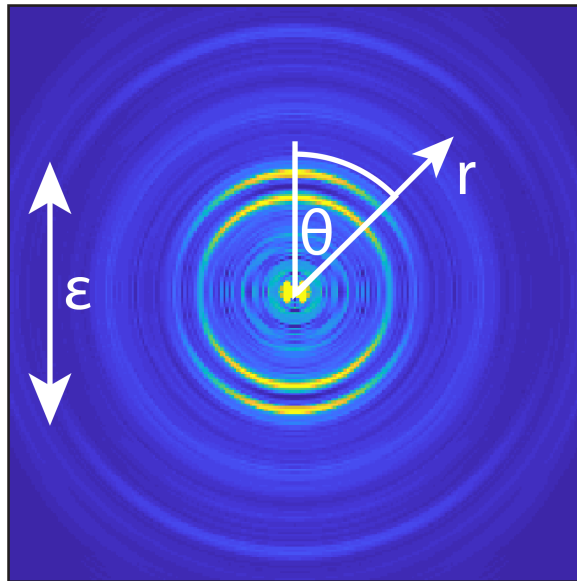
Figure 1.11: Ion image of oxygen atoms produced following photodissociation of molecular oxygen and subsequent resonant enhanced multiphoton ionisation of the oxygen atoms at 224.999 nm. The double headed arrow describes the electric vector of the light ϵ.

toexcitation laser, the angular distribution for a given kinetic energy feature can give information about the nature of the excited state in terms of its electronic symmetry or lifetime. In this specific ion image, the different rings represent photodissociation following absorption of a combination of different numbers of photons and to varying electronic states.

1.2.9   Covariance

Velocity Map Imaging is largely a statistical method, with the ion images (as shown in figure 1.11) being the product of summation over $\sim$ tens of thousands of laser shot. As such, when the images of two ions can be monitored in the same experimental cycle (the ability to do so will be the backbone of this thesis) statistical correlations between the two images can be drawn out.

Covariance is a statistical measure of the joint variability of two stochastic variables, that is to say when one measurement is made of a random phenomenon, what is the likelihood of another measurement being made at the same time. Strong covariance implies that the two measurements are somehow correlated and their appearance depends on the same random phenomenon. The covariance between two variables, X and Y, is described mathematically as the difference between the expectation value

for the product of the two variables $\langle XY \rangle$ and the product of the expectation values for the individual variables $\langle X \rangle \langle Y \rangle$.

$$\text{cov}(X, Y) = \langle XY \rangle - \langle X \rangle \langle Y \rangle \tag{1.19}$$

Covariance relies on the ability to repeat a measurement enough times to satisfactorily approach the statistical limit and that, while an individual measurement of the two variables may contain a true or false coincidence - or, indeed, no coincidence - , the real correlations will be borne out over time given appropriate treatment. The covariance between two variables can take any number between $-\infty$ and ∞, where a positive value indicates that as one variable increases/decreases the other variable also increases/decreases. A negative value for covariance implies that an increase in one variable is linked to a decrease in the other variable, and *vice versa*. A value of 0 indicates that there is no covariance between the variables.

Take for example a series of N humans for whom four values are measured - height, weight, intelligence quotient (IQ) and fitness. Intuitively, we can see that this data set, in the statistical limit, will have positive covariances (*e.g.* between height and weight), negative covariances (*e.g.* between weight and fitness) and no covariance (*e.g.* between intelligence and height) although certain individuals may not conform to any specific trend. A linear set of measurements such as this may be represented as a vector of variables (labelled H, W, I, and F, respectively) and multiplied to give a product matrix as shown in equation 1.20.

$$\begin{bmatrix} H \\ W \\ I \\ F \end{bmatrix} \times \begin{bmatrix} H & W & I & F \end{bmatrix} = \begin{bmatrix} HH & HW & HI & HF \\ WH & WW & WI & WF \\ IH & IW & II & IF \\ FH & FW & FI & FF \end{bmatrix} \tag{1.20}$$

Summing this over all measurements will give the matrix of expectation values for all combinations (equation 1.21) *i.e.* an expectation value for the XY pairs - $\langle XY \rangle$.

$$\sum_{i=1}^{\infty} \begin{bmatrix} HH & HW & HI & HF \\ WH & WW & WI & WF \\ IH & IW & II & IF \\ FH & FW & FI & FF \end{bmatrix}_i = \begin{bmatrix} \langle HH \rangle & \langle HW \rangle & \langle HI \rangle & \langle HF \rangle \\ \langle WH \rangle & \langle WW \rangle & \langle WI \rangle & \langle WF \rangle \\ \langle IH \rangle & \langle IW \rangle & \langle II \rangle & \langle IF \rangle \\ \langle FH \rangle & \langle FW \rangle & \langle FI \rangle & \langle FF \rangle \end{bmatrix} \tag{1.21}$$

Simultaneously we sum the vector over all i humans to produce a vector of expectation

values for each human to arrive at the vector shown in equation 1.22. By doing this for each human i and summing over all humans we get a sum of all the products of the variables.

$$\sum_{i=1}^{\infty} \begin{bmatrix} H & W & I & F \end{bmatrix}_i = \begin{bmatrix} \langle H \rangle & \langle W \rangle & \langle I \rangle & \langle F \rangle \end{bmatrix} \tag{1.22}$$

This can then be multiplied out to get a matrix of products of expectation values as shown in equation 1.23 *i.e.* the product of each pair of individual variable expectation values - $\langle X \rangle \langle Y \rangle$.

$$\begin{bmatrix} \langle H \rangle \\ \langle W \rangle \\ \langle I \rangle \\ \langle F \rangle \end{bmatrix} \times \begin{bmatrix} \langle H \rangle & \langle W \rangle & \langle I \rangle & \langle F \rangle \end{bmatrix} = \begin{bmatrix} \langle H \rangle \langle H \rangle & \langle H \rangle \langle W \rangle & \langle H \rangle \langle I \rangle & \langle H \rangle \langle F \rangle \\ \langle W \rangle \langle H \rangle & \langle W \rangle \langle W \rangle & \langle W \rangle \langle I \rangle & \langle W \rangle \langle F \rangle \\ \langle I \rangle \langle H \rangle & \langle I \rangle \langle W \rangle & \langle I \rangle \langle I \rangle & \langle I \rangle \langle F \rangle \\ \langle F \rangle \langle H \rangle & \langle F \rangle \langle W \rangle & \langle F \rangle \langle I \rangle & \langle F \rangle \langle F \rangle \end{bmatrix} \tag{1.23}$$

The covariance matrix can then be calculated as the difference between these two as follows

$$\begin{bmatrix} \langle HH \rangle & \langle HW \rangle & \langle HI \rangle & \langle HF \rangle \\ \langle WH \rangle & \langle WW \rangle & \langle WI \rangle & \langle WF \rangle \\ \langle IH \rangle & \langle IW \rangle & \langle II \rangle & \langle IF \rangle \\ \langle FH \rangle & \langle FW \rangle & \langle FI \rangle & \langle FF \rangle \end{bmatrix} - \begin{bmatrix} \langle H \rangle \langle H \rangle & \langle H \rangle \langle W \rangle & \langle H \rangle \langle I \rangle & \langle H \rangle \langle F \rangle \\ \langle W \rangle \langle H \rangle & \langle W \rangle \langle W \rangle & \langle W \rangle \langle I \rangle & \langle W \rangle \langle F \rangle \\ \langle I \rangle \langle H \rangle & \langle I \rangle \langle W \rangle & \langle I \rangle \langle I \rangle & \langle I \rangle \langle F \rangle \\ \langle F \rangle \langle H \rangle & \langle F \rangle \langle W \rangle & \langle F \rangle \langle I \rangle & \langle F \rangle \langle F \rangle \end{bmatrix} \tag{1.24}$$

$$= \begin{bmatrix} \mathrm{Cov}(H,H) & \mathrm{Cov}(H,W) & \mathrm{Cov}(H,I) & \mathrm{Cov}(H,F) \\ \mathrm{Cov}(W,H) & \mathrm{Cov}(W,W) & \mathrm{Cov}(W,I) & \mathrm{Cov}(W,F) \\ \mathrm{Cov}(I,H) & \mathrm{Cov}(I,W) & \mathrm{Cov}(I,I) & \mathrm{Cov}(I,F) \\ \mathrm{Cov}(F,H) & \mathrm{Cov}(F,W) & \mathrm{Cov}(F,I) & \mathrm{Cov}(F,F) \end{bmatrix} \tag{1.25}$$

Outside of academia, this analytical technique is used in a wide variety of applied problems such as analysing the stock market for correlations in the prices of different stocks and is effective because it requires no implicit bias in the analysis. In chemical dynamics this can used to draw out correlations between measurements, for example, features in complicated photoelectron spectrum arising from multiple products and photofragments can be linked with individual features in the relevant mass spectra if both are measured simultaneously.

1.3   Excited state dynamics

As a general rule, dissociation following electronic excitation of a molecule can be described by the equation 1.26 as previously shown in figure 1.2.

$$AB + h\nu \rightarrow AB^* \rightarrow A + B \qquad (1.26)$$
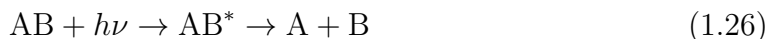
The total energy of the system (the molecule and the photon) must be conserved, and so for the photodissociation of any molecular system, denoted AB, the energy is accounted for by equation 1.27 where $E_{h\nu}$ is the energy of the incoming photon, D_0 is the dissociation energy of the bond, and E_{T_X} is the translational energy of atom X. The internal energy of any molecular fragments, electronic, vibrational or rotational, must be accounted for as well, where E_{int_X} is the internal energy of any molecular or atomic fragments which result from the photodissociation process.

$$E_{h\nu} = D_0 + E_{T_A} + E_{T_B} + E_{int_A} + E_{int_B} \qquad (1.27)$$

In a collision-free environment, the products will recoil with exactly equal and opposite momenta in the reference frame of the molecule. Sampling repeatedly over multiple experiments will build up a distribution of measured momenta from the Newton sphere which are fitted to circular distributions (either isotropic or anisotropic as discussed later in section 1.3.2) which can be related to their spherical origin. The measurement of the momentum of a recoiling particle can be decomposed into a radial and angular component. It is helpful to understand the radial component, which defines the kinetic energy of the particle first, as this is consistent for all types of experiment whereas treatment of the angular component will differ for different types of experiment. If it is only possible to measure the kinetic energy of one fragment, the total kinetic energy of the system can still be extracted according to the conservation of momentum by assuming that the system dissociates into only two fragments, as in equation 1.26. The expression for the conservation of momentum $m_A v_A = m_B v_B$ can be substituted into the simple expression for the TKER as a linear sum of the kinetic energies of both fragments (equation 1.28a) to yield a formulation for the TKER that is independent of the velocity of one of the fragments (equation 1.28b).

$$TKER = \frac{1}{2}m_A v_A^2 + \frac{1}{2}m_B v_B^2 \qquad (1.28a)$$

$$TKER = \frac{1}{2}m_A v_A^2 \left(1 + \frac{m_A}{m_B}\right) \tag{1.28b}$$

1.3.1 $n\sigma^*/\pi\sigma^*$ States

The molecules in this thesis are predominantly small organic, closed shell systems such as thioethers and thiophenes within which the highest occupied molecular orbital is either a non-bonding "n" or bonding π type orbital depending on the presence of an aromatic system or not. The orbital most important in a photodissociation event, such as those studied in this thesis, is invariably the σ^* orbital along the dissociating bond and therefore excitation processes which can populate the σ^* orbital must be carefully considered.

The ground electronic state in all cases is a singlet state, with no unpaired electrons. Excitation with a single photon forms an excited state with two unpaired electrons. The spins may be anti-parallel (singlet state) or parallel (triplet state). While the triplet state is lower in energy due to the lower exchange energy, in the absence of spin-orbit coupling a singlet to triplet excitation is electric dipole forbidden and so the only accessible excited states by photoabsorption are singlet states.

In molecules belonging to the C_{2V} point group, excitation from the highest occupied out of plane orbital to an orthogonal σ^* orbital, creating a so called $n\sigma^*$ or $\pi\sigma^*$ state, is formally forbidden. This applies to both planar non aromatic systems (such as thiothers) and planar aromatic systems (such as thiophenes) where the excitation begins on a π and p orbital, respectively. This provokes a mystery as to why photoexcitation so readily results in dissociation. Herein lies a classic example of the role CIs can play in photochemical processes. Specific examples of this behaviour will be discussed in more detail in chapters 3 and 4 and this section will be restricted to a more general discussion.

In reality, the excitation is weakly allowed by any distortion away from the optimum geometry in a coordinate which breaks the rotational symmetry of the molecule, reducing the point group to C_S. Excitation to an $n\pi^*$ or $\pi\pi^*$ state however, is symmetry allowed and, as has been shown by a wealth of experiments, conical intersections which funnel flux between the $n\pi^*$ or $\pi\pi^*$ state and the respective $n\sigma^*$ or $n\sigma^*$ state are ubiquitous in small organic molecules.[32]

1.3.2   Angular Distributions of Photodissociations

Modelling Angular Distributions

In a photodissociation experiment, the angular distribution of photofragments is typically measured with respect to the polarisation vector of the photons responsible for the excitation. The angle between the polarisation vector of the light and the ejected particle is henceforth defined as θ (and shown in figure 1.11). At any given radius, the degree of anisotropy is characterised by fitting to a sum of even ordered Legendre polynomials where the order is truncated at $2n$, where n is the number of photons involved in the excitation step.

$$I(\theta) \propto \frac{1}{4\pi}[1 + \beta P_2(cos(\theta))] \qquad (1.29)$$

In much of the work contained in this thesis, the photoexcitation is a single photon process and so all distributions follow the functional form shown in equation 1.29 where $I(\theta)$ is the intensity at a given angle, P_2 is the second order Legendre polynomial which has the form shown in equation 1.30, and β is the fitting parameter which weights the degree of anisotropy.

$$P_2(cos(\theta)) = \frac{1}{2}(3cos^2\theta - 1) \qquad (1.30)$$

Limiting values for the β parameter that describe molecular photodissociation were derived to be between $+2$ - a parallel transition where the photofragments recoil along the polarisation axis - and -1 - a perpendicular transition in which the fragments recoil perpendicular to the polarisation axis.[24] Encoded within these values is information about the nature of the photoexcitation with respect to symmetry. The β parameter is not restricted to its limits though, and non-limiting values can provide a wealth of information about the dissociation of molecules. For example, a dissociation which is slow in comparison to the rotational period of the molecule can have its possible photodissociation trajectories smeared out leading to a non-limiting β value.

Reconstruction

A Newton sphere impinging on a two-dimensional detector is typically detected in its entirety and crushed, or pancaked, upon the detector. In the plane of the detector, the true kinetic energy spectrum, and corresponding "true" angular distributions are contained within the infinitesimally thin central slice. A crushed image is corrupted

from this by the content of out of plane components. Thankfully, the transformation of a crushed Newton sphere to its central slice is analytically soluble for a general, cylindrically symmetric function through the Abel transformation. Photofragment angular distributions may be accurately modeled and reconstructed in this manner based on a few valid assumptions. The first is that the distribution around the polarisation axis of the photoexcitation light is cylindrically symmetric. For the one photon excitation processes that drive photodissociation in this thesis, this is always valid and, provided the polarisation vector is exactly parallel or orthogonal to the plane of the detector the resulting distribution is always cylindrically symmetric.

The earliest approach to reconstruction of the central slice was via the Fourier-Hankel method[33] wherein the two dimensional projection first underwent Fourier transform to back out the three dimensional sphere before undergoing an inverse Hankel transform to the central slice. While effective, the primary drawback of this method is its sensitivity to noise.

Onion Peeling[34] introduces a second assumption to the analysis which is that for the maximum radius, within some radial binning, the only contribution to that radius must come from the central slice. This is valid as any particles ejected with the maximum available kinetic energy will either occupy the maximum radius in the two dimensional projection or contribute to a smaller radius in the plane of projection as their velocity is partially deposited in the out of plane component. The intensity at this radius is then used as a guide for the contribution of that particle around the sphere as it deposits more of its kinetic energy into the out of plane components and these can then be subtracted from the total image. The resulting two dimensional projection is then subtracted from the original image, the radius is stepped in and the process is repeated for the next "layer" of the onion/image. This method is computationally fast but suffers from introduction of significant noise arising from applying an inherently polar technique to a Cartesian grid of intensities.

The weak spot in the Fourier-Hankel transformation method is the noise sensitive transformation to the 3D distribution. An iterative method by Vrakking and coworkers[35] disposes with the problematic transform of noisy data from the 2D projection to the 3D distribution. Instead, it fits the 2D projection as a 3D distribution and uses this as an initial guess for an iterative method which converges on a 3D distribution which forward projects to give a 2D projection which can be compared with the experimental 2D data.

The BASEX method[36] is similar in implementation to the Fourier-Hankel method

but rather than working with raw data, employs the transformation of known, well behaved, Gaussian like basis functions to more reliably transform the 2D projection to the 3D distribution. Assuming the projection is not so noisy as to be impossible to fit to a sum of Gaussians - an unlikely scenario - the distribution is transformed reliably, with the advantage that the transforms can be precomputed to save time in transforming the actual image.

All of the methods discussed so far have focused on analysing the events in Cartesian space, either by treating each pixel individually or by describing each pixel as a sum of Gaussian basis functions. In reality, the problem is polar in nature, as the intensity functions which describe the distributions are angle dependent. The pBASEX method[37] recognises this and applies it to the highly effective BASEX method. Instead of representing each pixel as a Gaussian basis function, the Cartesian pixels are transformed into polar coordinates. These intensities can then be fit to two dimensional functions whose radial component is described by a Gaussian profile and angular component is described by a suitably chosen combination of Legendre polynomials (*i.e.* second order for a one-photon process as shown in equation 1.29). In a similar manner to the BASEX method, the transformations can be precomputed for the polar functions employed by pBASEX with the added advantage that each polar function describes a wider region of space (the full circular distribution for a given r rather than a single polar/Cartesian coordinate). As a result, fewer functions are required to describe the data to the same level as BASEX and the transform is either faster or a larger number of functions per unit data can be used to give a higher quality transformation of the image.

The polar onion peeling[38] (POP) method - used extensively in this thesis - combines elements of the pBASEX and onion peeling methods. The high speed of the onion peeling method is appealing but starting from outer pixels and working inwards is shown to lead to spurious intensities as errors gather. Rather than working on a pixel by pixel basis the POP method draws inspiration from pBASEX and treats the onion to be peeled as successive layers of Legendre polynomials. Like in the BASEX and pBASEX methods, the analytical Abel and inverse Abel transformations can be precalculated for the polar basis functions. In a similar fashion to onion peeling, the outermost layer is used to guide construction of a three dimensional distribution of particles which is Abel transformed to yield the two dimensional projection. The out of plane components (*i.e* any signal at radii smaller than the outer circle) is subtracted to yield the infinitesimal central slice. The full two-dimensional projection of

this component is subtracted from the original image and the process is repeated with the radius incrementing ever inwards. The error accumulation that plagues Cartesian onion-peeling persists here, but due to the nature of the operation the errors are accumulated towards the center, where the quality and importance of the image are less anyway.

Towards the end of this author's time working with reconstructable ion images a modification of the pBASEX algorithm worthy of note was reported: DAVIS A Direct Algorithm for Velocity-map Imaging Systems.[39] DAVIS attempts to provide a solution for the problematic inverse Abel transformation step, which has proven so tricky in previous attempts due to its noise sensitivity. The algorithm mimics pBASEX in its initial fitting of the experimental data to a series of polar basis functions with a Gaussian profile in the radial axis and sensibly chosen order(s) of Legendre polynomials for the angular distributions. Where the pBASEX then implements a relatively slow numerical integration to project the 3D distribution, DAVIS employs an analytical solution which is computationally significantly faster and more accurate.

Slice Imaging

Rather than rely on reconstruction algorithms, some groups have chosen to access the central slice experimentally. One of the early approaches was to manipulate the ionisation laser into a sheet parallel to the detector rather than the traditional cylindrical beam of light.[40] Here, the Newton sphere was allowed to expand for up to a microsecond before being ionised to ensure that the molecules had expanded far enough to ensure the sheet sampled a sufficiently thin segment of the Newton sphere. The drawback of this is of course, that the photon densities required for higher order multiphoton ionisation processes were difficult to achieve, but given the technology available this is a remarkable experimental result.

With the advance of fast high voltage pulsing units, the MCP/Phosphor screen detectors typically used for ion imaging could be switched on and off on a timescale of nanoseconds. By modifying ion optics to stretch the Newton sphere along the propagation axis, Kitsopoulos and co-workers demonstrated that the detector could be switched on selectively to record just the central slice of the Newton sphere.[41]

1.4 Objectives

The overall objective of this thesis is to explore excited state dynamics that have previously proven difficult to measure. Velocity map imaging is a mature and established method for studying dynamics but the description given in this introduction implicitly considers VMI as a method for imaging a single species at a time which is separable from the precursor parent by mass. As such it has been impossible for VMI to characterise the relative efficiency of rival pathways leading to different photofragments or to study photoproducts which are inseparable from their parent precursor by mass. This thesis describes coupling VMI to a multiplexing camera capable of making correlated measurement of multiple photofragments at once and, in three chapters, details the set up of two different multi-mass velocity map imaging experiments. Chapters 3 and 4 both cover the experiment coupled to SPI and investigate, respectively, the possible pitfalls in contrast to REMPI and report novel measurements of competitive bond dissociation. Chapter 5, describes a new Coulomb Explosion Imaging apparatus for ultrafast structural determination. A brief survey of these three results chapters follows. The thesis then concludes with a short summary chapter which considers whether the objectives were achieved, what the findings were and ponders future avenues for extending this research.

1.4.1 Single Photon Ionisation for Multi-Mass Imaging

The use of vacuum ultraviolet photons as an ionisation method for multi-mass imaging is a source of unexpected observations. Chapter 3 investigates the photodissociation of dimethyl sulfide at 227.5 nm and explores how careful treatment of polarisation laser alignment to the axis of photoproduct detection is required to avoid misrepresenting angular distributions. This chapter also considers how the simultaneous ionisation of multiple products, as well as the parent molecule, can have an adverse affect on the radial velocity resolution due to interactions between the different charged particles.

1.4.2 Competitive Bond Dissociation

The advent of fast framing cameras has paved the way for making correlated measurements of photofragments produced simultaneously in an experiment. Chapter 4 resolves to develop a generalised technique to characterise dissociation processes which break bonds competitively following photoexcitation, to accurately measure

the preference for one bond cleavage versus another, and to rationalise the regions of the potential energy surface that lead to this. The chapter focusses on the photodissociation of t-Butyl Methyl Sulfide in the region between 227.5 and 222.5 nm and reports the ratio of S–Methyl to S–t-Butyl dissociation as a function of wavelength.

1.4.3   Ultrafast Structural Determination

Photodissociation processes which do not lead to photofragmentation are challenging to study in the gas phase as their photoproduct is a structural isomer of the parent molecule and thus is inseparable from the parent by mass. Chapter 5 charts the beginnings of a new experiment in Bristol: Coulomb Explosion Imaging. This technique employs the same multi-mass imaging technology to turn ion imaging on its head to monitor the vectors of fragments resulting from multiply ionising the parent and letting it explode according to Coulombic repulsion. The resulting vectors can be used to chart back the structure of the molecule within a time window of a few tens of femtoseconds for a ground state, one colour explosion. By coupling this probe technique with excitation using similarly ultra short pulses of UV light, this serves as the basis of a probe of molecular structure on a time frame short enough to watch it evolve on the excited state - ideal for charting photoisomerisation and photoinduced ring opening reactions.

Bibliography

[1] Y. L. Yung, M. Allen, and J. P. Pinto, Astrophys J Suppl. S. **55**, 465 (1984), ISSN 0067-0049.

[2] N. H. C. Lewis, N. L. Gruenke, T. A. A. Oliver, M. Ballottari, R. Bassi, and G. R. Fleming, J. Phys. Chem. Lett **7**, 4197 (2016).

[3] G. Wald, Science **162**, 230 (1968), ISSN 0036-8075.

[4] T. Bach and J. P. Hehn, Angew. Chem. Int. Ed. **50**, 1000 (2011), ISSN 1433-7851.

[5] J. R. Tritsch, W.-L. Chan, X. Wu, N. R. Monahan, and X.-Y. Zhu, Nat. Commun **4**, 2679 (2013), ISSN 2041-1723.

[6] M. Born and R. Oppenheimer, Annalen der Physik **389**, 457 (1927), ISSN 0003-3804.

[7] D. Polli, P. Altoè, O. Weingart, K. M. Spillane, C. Manzoni, D. Brida, G. Tomasello, G. Orlandi, P. Kukura, R. A. Mathies, et al., Nature **467**, 440 (2010).

[8] C. Wittig, J. Phys. Chem. B **109**, 8428 (2005), ISSN 1520-6106.

[9] S. W. Hell and J. Wichmann, Opt. Lett. **19**, 780 (1994), ISSN 0146-9592.

[10] B. N. Chichkov, C. Momma, S. Nolte, F. Alvensleben, and A. Tünnermann, Appl. Phys. A. **63**, 109 (1996), ISSN 0947-8396.

[11] T. W. Hänsch, Appl. Opt **11**, 895 (1972), ISSN 0003-6935.

[12] M. N. R. Ashfold and J. D. Howe, Annu. Rev. Phys. Chem. **45**, 57 (1994), ISSN 0066-426X.

[13] J. Lavancier, D. Normand, C. Cornaggia, and J. Morellec, J. Phys. B: At. Mol. Opt. Phys. **23**, 1839 (1990), ISSN 0953-4075.

[14] G. Mainfray and C. Manus, Appl. Opt. **19**, 3934 (1980), ISSN 0003-6935.

[15] P. M. Johnson and C. E. Otis, Annu. Rev. Phys. Chem. **32**, 139 (1981), ISSN 0066-426X.

[16] G. Bjorklund, IEEE J. Quantum Electron. **11**, 287 (1975), ISSN 0018-9197.

[17] R. Mahon, T. McIlrath, V. Myerscough, and D. Koopman, IEEE J. Quantum Electron. **15**, 444 (1979), ISSN 0018-9197.

[18] R. H. Page, R. J. Larkin, A. H. Kung, Y. R. Shen, and Y. T. Lee, Rev. Sci. Instrum. **58**, 1616 (1987), ISSN 0034-6748.

[19] G. Hilber, A. Lago, and R. Wallenstein, J. Opt. Soc. Am. B **4**, 1753 (1987), ISSN 0740-3224.

[20] L. V. Keldysh, Soviet Physics JETP **20**, 1307 (1965).

[21] H. R. Reiss, Phys. Rev. Lett. **101**, 043002 (2008), ISSN 0031-9007.

[22] Y. T. Lee, J. D. McDonald, P. R. LeBreton, and D. R. Herschbach, Rev. Sci. Instrum. **40**, 1402 (1969), ISSN 0034-6748.

[23] G. E. Busch, J. F. Cornelius, R. T. Mahoney, R. I. Morse, D. W. Schlosser, and K. R. Wilson, Rev. Sci. Instrum. **41**, 1066 (1970), ISSN 0034-6748.

[24] R. N. Zare and D. R. Herschbach, Bull. Amer. Phys. Soc. **7**, 458 (1962).

[25] M. N. R. Ashfold, B. Cronin, A. L. Devine, R. N. Dixon, and M. G. D. Nix, Science **312**, 1637 (2006), ISSN 0036-8075.

[26] M. N. R. Ashfold, K. Yuan, and X. Yang, J. Chem. Phys. **149**, 080901 (2018), ISSN 0021-9606.

[27] D. W. Chandler and P. L. Houston, J. Chem. Phys. **87**, 1445 (1987), ISSN 0021-9606.

[28] A. T. J. B. Eppink and D. H. Parker, Rev. Sci. Instrum. **68**, 3477 (1997), ISSN 0034-6748.

[29] H. L. Offerhaus, C. Nicole, F. Lépine, C. Bordas, F. Rosca-Pruna, and M. J. J. Vrakking, Rev. Sci. Instrum. **72**, 3245 (2001), ISSN 0034-6748.

[30] D. Townsend, M. P. Minitti, and A. G. Suits, Rev. Sci. Instrum. **74**, 2530 (2003), ISSN 0034-6748.

[31] D. J. Hadden, T. M. Messider, J. G. Leng, and S. J. Greaves, Rev. Sci. Instrum. **87**, 106104 (2016), ISSN 0034-6748.

[32] M. N. R. Ashfold, G. A. King, D. Murdock, M. G. D. Nix, T. A. A. Oliver, and A. G. Sage, Phys. Chem. Chem. Phys. **12**, 1218 (2010), ISSN 1463-9076.

[33] R. N. Strickland and D. W. Chandler, Appl. Opt. **30**, 1811 (1991), ISSN 0003-6935.

[34] C. Bordas, F. Paulig, H. Helm, and D. L. Huestis, Rev. Sci. Instrum. **67**, 2257 (1996), ISSN 0034-6748.

[35] M. J. J. Vrakking, Rev. Sci. Instrum. **72**, 4084 (2001), ISSN 0034-6748.

[36] V. Dribinski, A. Ossadtchi, V. A. Mandelshtam, and H. Reisler, Rev. Sci. Instrum. **73**, 2634 (2002).

[37] G. A. Garcia, L. Nahon, and I. Powis, Rev. Sci. Instrum. **75**, 4989 (2004), ISSN 0034-6748.

[38] G. M. Roberts, J. L. Nixon, J. Lecointre, E. Wrede, and J. R. R. Verlet, Rev. Sci. Instrum. **80**, 053104 (2009), ISSN 0034-6748.

[39] G. R. Harrison, J. C. Vaughan, B. Hidle, and G. M. Laurent, J. Chem. Phys. **148**, 194101 (2018), ISSN 0021-9606.

[40] K. Tonokura and T. Suzuki, Chem. Phys. Lett. **224**, 1 (1994), ISSN 0009-2614.

[41] C. R. Gebhardt, T. P. Rakitzis, P. C. Samartzis, V. Ladopoulos, and T. N. Kitsopoulos, Rev. Sci. Instrum. **72**, 3848 (2001), ISSN 0034-6748.

Chapter 2

Experimental and Theoretical Methods

This chapter covers the underpinning theory required to understand the velocity map imaging apparatus which underpins the experimental work in this thesis, as well as a variety of theoretical methods which are employed to support the interpretation of these experiments. The experimental section includes but is not limited to, the preparation of molecules for study in high vacuum conditions, the generation of laser pulses with high spectral resolution as well as ultrashort femtosecond laser pulses, equipment for detection ions and the analysis methods required to extract meaningful data. The theoretical section covers the basis of *ab initio* quantum chemisty calculations in Hartree-Fock theory and extends this through multireference complete active space methods.

2.1 Vacuum Systems

In order to make measurements of molecules in the absence of intermolecular effects, high vacuum conditions need to be maintained where the mean free time between molecular collisions greatly exceeds the lifetime of the measurement. In order to achieve this, the ion imaging experiments that form the backbone of this thesis are performed in a sealed vacuum chamber capable of sustaining high vacuum conditions, defined as being on the order of 10^{-7} – 10^{-8} mbar. The VMI apparatus in Bristol consists of three vacuum chambers as shown in figure 2.1. These three chambers are defined, as the "source", "interaction" and "detection" chambers in the order that molecules traverse the system. These three chambers are differentially pumped

- which is to say that the vacuum conditions in each chamber are predominantly sustained by independent pumps. The source and interaction chambers are separated by a baffle with only a skimmer orifice as a point of connection between the two. When an experiment is running, the detection and interaction chambers are open to one another and they are completely isolated from one another via closure of a gate valve when the experiment is out of operation to try to maintain the highest vacuum conditions on the detector at all times. Standard pumps such as rotary or scroll pumps are insufficient for achieving high vacuum conditions alone, bottoming out at 10^{-3} mbar. Below a certain pressure (typically around 10^{-3} mbar) the pumping regime changes from a "viscous flow" regime - well described by conventional fluid dynamics - to a molecular flow regime - where a particle description is more appropriate as the mean free path length becomes greater than the size of the chamber. In this regime, turbomolecular pumps are required. These operate on a principle of making the passage of any given particle into the turbo pump an irreversible process. This is achieved by layering a set of spinning blades close together. The angle of the blades in one disc and the relative phasing of the blades of one disc with respect to the next, is optimised so that a particle which makes it through the first disc is immediately knocked downwards and through the next blades, where it is knocked downwards again thus creating the desired irreversibility. The Bristol VMI rig has three turbo pumps backed by two scroll pumps which are common to all three turbopumps. This creates a system where the failure of any given pump will not raise the pressure of a given chamber above 10^{-3} mbar.

2.2   Sample Preparation

The molecules in this thesis are prepared by freeze pump thaw purification using a Schlenk line before being loaded into a glass bulb. A vial with a rubber O-ring is loaded with the molecule to be studied and attached to a Schlenk line arm with a binary tap via an o-ring and clamp. The Schlenk line is held under vacuum by a rotary pump and the tap which connects the sample vial is left closed. The sample vial is immersed in liquid nitrogen to freeze the sample and, once frozen, the tap is opened to vacuum to remove the gaseous portion that was not frozen. The tap is then closed, the liquid nitrogen removed, and the sample vial is allowed to warm to room temperature. A sample contaminated with air begins to bubble as it melts. Once completely melted, the sample vial is reimmersed in the liquid nitrogen and the

process is repeated until no bubbles are observed on melting, thus eradicating the sample of air contamination. Once the sample is purified, a glass bulb with an O-ring connection is attached to a separate arm with a binary tap on the Schlenk line by an o-ring and clamp. The bulb tap is opened and vacuumed out before the Schlenk line is closed to the rotary pump, leaving the system under vacuum. The tap to the sample vial is opened slowly and the vapour of the sample is drawn off up to a certain pressure, typically around 10 - 100 mbar, as monitored by a pressure gauge attached to the Schlenk line. The sample tap is closed and Helium gas (N 6.0 BOC) is bled into the system until it reaches the desired total pressure, typically 1 bar to make a 10% concentration sample.

2.3   Molecular Beams

Molecules are introduced to the chamber for study in the form of a pulsed molecular beam. Described most eloquently by John B. Fenn in his foreword to Scoles' comprehensive textbook on the subject,[1] and emphasised by van der Meerakker and coauthors in their 2012 review on the subject[2] "Born in leaks, the original sin of vacuum technology, molecular beams are collimated wisps of molecules traversing the chambered void that is their theatre...". Ion imaging experiments often rely heavily on molecular beam methods. By "leaking" gas phase molecules held at pressures approaching or significantly above atmospheric pressure into a high vacuum ($\sim 10^{-7}$ mbar) they undergo a supersonic expansion. In the throat of the expansion they collide frequently to cool the molecules to their rotational and vibrational ground states and begin to expand with a $\cos^2\theta$ distribution where θ is the angle between the velocity vector of the molecules and the central axis of the molecular beam.

The source chamber contains a pulsed valve (General Valve, Series 9) which consists of a spring loaded solenoid which drives a poppet in and out of a faceplate which faces into the vacuum chamber. The faceplate has a 60° conical aperture to encourage the supersonic expansion and preparation of a cold molecular beam in the chamber.

The molecules are allowed to expand for approximately 4.5 cm before they meet a skimmer (Beam Dynamics, 1 mm aperture). The coldest portion of the molecular beam is the exact centre, where the molecules are internally coolest. The skimmer selects this central portion, rejecting the warmer off axis molecules, and also collimates the beam as the central molecules have the least off axis velocity. The surviving molecules are introduced to the interaction chamber, where they immediately travel
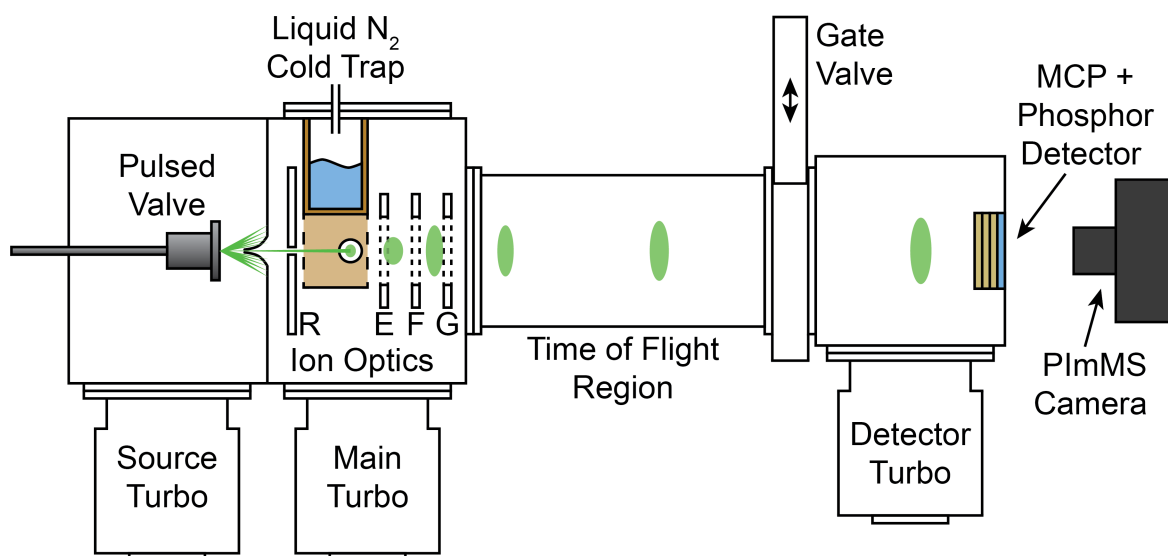
Figure 2.1: Schematic of the vacuum chamber employed for Velocity Map Imaging experiments. Three main sections are detailed from left to right. The source chamber where molecules are introduced, the main chamber where the photochemistry is initiated, and the time of flight tube/detector chamber, where the photofragments are mass separated and detected.

through an aperture in the centre of the ion optics repeller plate.

2.4   Laser Systems

The population inversion required for lasing (as discussed in section 1.2.6) can be created in a medium by a variety of methods, such as electrical discharge – as in an excimer laser – or, most commonly, by optical pumping by a separate laser or flash lamp. Nd:YAG and Nd:YLF lasers act as the respective pump methods for the dye and titanium sapphire lasers used in this thesis and thus are discussed first. The lasing medium is either an Ytterbium Aluminium garnet crystal ($Y_3Al_5O_{12}$) or Yttrium Lithium Fluoride ($LiYF_4$) garnet crystal doped with neodymium, which provides the energy levels for lasing. Nd:YAG is a four level lasing system with an emission band centered at 1064 nm in YAG or 1054 nm in YLF wherein the initial pumping is induced by either solid state diodes or flashlamps.

 This is an example of tuning the exact laser wavelength by subtle adjustment

of the crystal structure. While the neodymium ions still support the population medium, the fundamental wavelength can be adjusted by changing the host medium. These fundamental wavelengths of 1064 and 1054 nm can be converted to higher harmonics (typically the second and third) by passing through appropriate crystals - typically lithium triborate (LBO). Two different Nd:YAG lasers are used in this thesis, a flashlamp pumped Spectra-Physics GCR-250 (15 W, 1064 nm, 10 Hz) used for pumping the dye laser, a flashlamp pumped Continuum Surelite II (6.5 W, 1064 nm, 10 Hz) and one Nd:YLF diode pumped Coherent Revolution (40 W).

2.4.1   Tuneable UV Dye Lasers

Dye lasers are prized for their broad range of tunability, spectral resolution, and output power. They cover the entire visible spectrum and well into the UV, delivering pulses which have sub-wavenumber bandwidth and energies up to a few millijoules. Dye lasers take advantage of the spectrallyh quantum yield fluorescence of a variety of classes of molecules such as coumarins or rhodamines. A schematic of a typical dye laser is shown in figure 2.2. The population inversion is created by optical pumping of a dye cuvette with either the second (532 nm) or third harmonic (355 nm) laser pulse from a Nd:YAG depending on the dye. The dye fluoresces isotropically and in one axis the light is reflected by a diffraction grating and mirror pair, the geometries of which are tuned so that monochromatic light is selected. The monochromatic light is then directed back through the original dye cuvette causing further stimulated emission in the oscillator. Prior to this the pump light is split into three portions, the first of which caused the initial population inversion. The second pulse is delayed via taking a longer path and repumps the dye cuvette. This time, rather than surviving long enough to fluoresce, the monochromatic light from the grating stimulates emission in the dye. As the stimulated emission is in the same direction and coherent with the light that induces the emission (as discussed in section 1.2.6) this serves to amplify the monochromatic light pulse. The laser light from the first dye cell then travels into a second dye cell, which is pumped by the third portion of the Nd:YAG output, to stimulate emission in this second amplification cell.
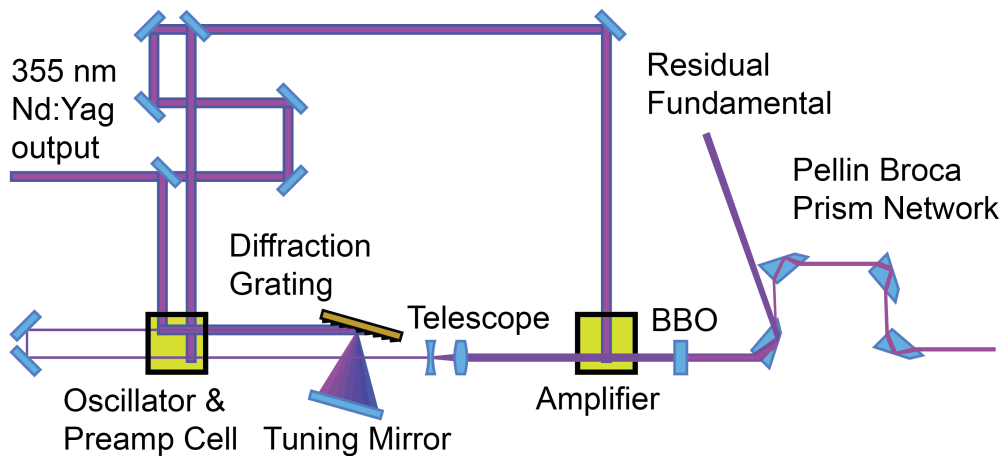
Figure 2.2: Schematic of a tuneable dye laser with an optional BBO SHG crystal and Pellin Broca prism network for generation of UV light.

2.4.2 118 nm VUV Generation by Third Harmonic Generation

As discussed in section 1.2.7 theory, generation of VUV light of wavelength $\lambda = 118$ nm can be achieved by frequency tripling the 355 nm laser light produced as the third harmonic of a Nd:YAG laser.[3;4] The tripling cell used in the Bristol experiments is shown in figure 2.3 and consists of a long primary tube capped on one end by a fused silica window and on the other end by a custom made lithium fluoride lens with a predicted focal length of 14 cm at 118 nm. The xenon transition which is exploited for tripling is the $5p \rightarrow 5d$ transition at 119.2 nm (83889.971 cm^{-1})[5] and the mixing gas used to achieve the phase matching condition is argon.[6] To achieve efficient VUV generation, the chamber must be clear of impurities and so before loading the chamber with the tripling gases the chamber is brought down to high vacuum conditions ($\sim$ 1x10^{-7} mbar) via a turbomolecular pump attached to the bottom. A gate valve in front of the turbomolecular pump is used to isolate the cell from the turbo and hold the cell at low vacuum conditions. The xenon and argon are bled into the chamber via needle valves to partial pressures of 32 mbar and 368 mbar respectively to satisfy the phase matching condition of 1:11.5 xenon to argon.[7] Attached to the bottom of the tripling cell is a system of pipes which act as a cooling loop. The central pipe is encased in a bath containing a mixture of methanol and dry CO_2 which maintains a temperature of -70° C.[8] This has two effects which improve the tripling efficiency. The
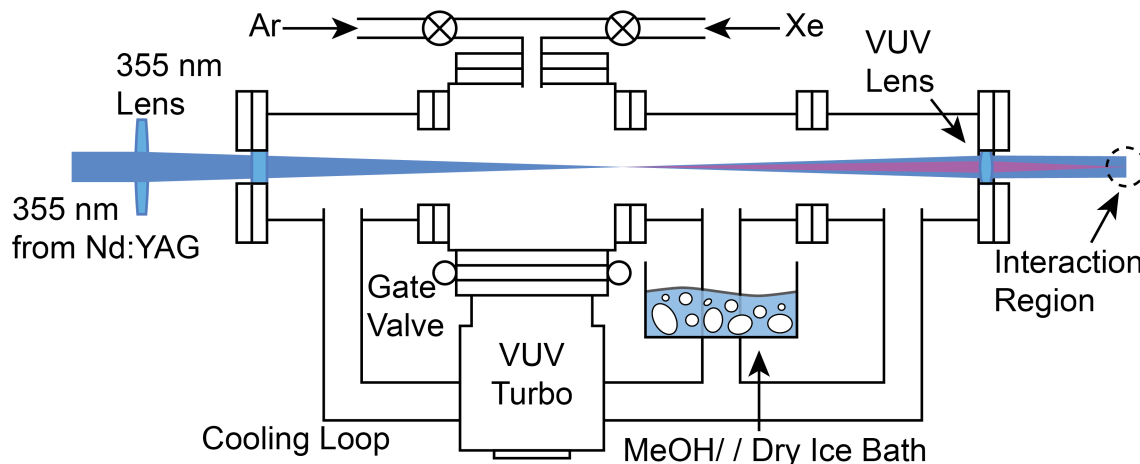
Figure 2.3: Schematic of the VUV tripling cell and adjoining mixing/cooling tubes.

first is that it creates a local cold point inside the chamber to freeze out any residual impurities, particularly water vapour, that survived the low vacuum conditions or were introduced along with the gases. The second is that it helps create a thermal current inside the cell which ensures complete and consistent mixing of the gases, avoiding any local pockets of either gases where the tripling might be less efficient.

2.4.3 Ultrafast Ti:sapphire Lasers

Generation and amplification of femtosecond laser pulses is non-trivial but draws on the same underlying principles of creating a population inversion and then stimulating emission to achieve amplification. In this case the pulse that stimulates the emission must already be extremely short. This is achieved through a phenomenon known as modelocking.

To generate temporally short laser pulses, light of broad spectral frequency must be phase locked so that the overall interference of the waves is only constructive within a small portion of the pulses in time to produce a short pulse envelope. For a cavity of a given length, only light with a wavelength which is a mode of the cavity can be stabilised producing a resonator which has a narrow spectral bandwidth, regardless of how broadband the pump light is. To produce a broadband cavity a pair of prisms are introduce to the cavity path, the prisms spatially disperse the light during its cavity roundtrip and, with carefully design of the geometries, light at every portion of the spectrum experiences its own cavity length thus stabilising multiple frequencies in the same cavity. The cavity is pumped by a broadband, pulsed laser source and initially, although these individual modes are stabilised within the cavity, they are

not modelocked. In amusing contrast to the careful design of the broadband cavity, to achieve the modelocking the cavity must undergo a sudden jolt, typically by firmly tapping one of the cavity mirrors (or by banging the table next to it). This causes a momentary spike in intensity in the cavity. At this peak intensity, non-linear effects begin to become important, one of which is the optical Kerr effect. The Kerr effect is a change in the refractive index of a medium in response to the intensity of the light field passing through it. Because the spatial intensity of a light pulse is non-uniform (*e.g.* a Gaussian shaped pulse) the refractive index of the medium also becomes non uniform, creating a lensing effect called Kerr lensing. This brings the modes of the cavity into phase at a given point in the cavity, typically the focal point of the lensing, creating the short pulse. Once the pulse has been initially created the lensing effects becomes more intense locking more and more modes together until it runs out of cavity modes to lock, saturating the effect. The result is a short pulse travelling back and forth within the cavity.

While mode locking is highly effective at producing short pulses of light, there is a limit to the energy of these pulses as dictated by the damage threshold of the optics. As such the short pulses produced by the oscillator must be amplified multiple times in order to achieve pulses of suitably high energy for tabletop experiments.

In order to amplify the short pulses they are injected into a second cavity capped on either end by combining a Pockels cell - an electro-optic which rotates the polarisation of the light in response to an electric field - with a thin film polariser. The cavity, set up in a Z configuration with a Titanium Sapphire crystal in the centre, then allows the short pulses to bounce back and forth in the cavity. The Ti:Sapphire crystal is pumped by pulsed laser light at 537 nm (the second harmonic of a Nd:YLF laser) and on each round trip more and more coherent light is produced by stimulated emission - this is known as regenerative amplification. After a given number of round trips (as close to the cavity saturation point as possible), the exit Pockels cell is triggered to dump the light from the Z cavity. Due to their temporally short pulses, the peak power of ultrafast laser pulses is extraordinarily high. To avoid burning the cavity, the seed pulse is stretched in time prior to injection into the amplifier cavity and then the amplified pulse is recompressed following ejection from the cavity.

2.4.4 Laser Configurations

There are two distinct experimental set ups which are utilised throughout this thesis, both centred on the same vacuum apparatus described above 2.1. The nanosecond

set up consists of a Sirah Cobra Stretch dye laser configured with a 2400 lines/mm grating. The dye laser is pumped by the third harmonic of a Spectra Physics GCR-250 Nd:YAG (355 nm) which produces approximately 4 W of pump power for the dye laser at a repetition rate of 10 Hz. In two colour experiments, the ionisation laser consists of 118 nm photons produced by frequency tripling the third harmonic of a Continuum Surelite II Nd:YAG laser. In this case, the 355 nm light from the Nd:YAG laser is first attenuated by reflection off of two 20 % reflective beamsplitters with the transmissive portion terminating in a beam dump. Attenuation via beamsplitters is more desirable than attenuating by detuning the delay between the flashlamp and Q-Switch as the delay attenuation can cause larger shot to shot variation in power.

2.5 Velocity Map Imaging

2.5.1 Ion Optics

The velocity map imaging optics in the Bristol experiment have not been varied since they were reported in the literature.[9] Briefly, they include a variety of modifications over more traditional ion optic assembly designs.[10] These include a thicker extractor plate which shields the interaction zone from extra fields and a curved bezel in the aperture of the extractor plate which lowers the gradient in the field lines and reduces spherical aberrations. The overall stack of lenses is slightly longer and intermediate stabilisation plates are installed between the electrodes (one between extractor and lens and two between the lens and ground) which are held at intermediary voltages via potential divider circuits. These maintain the integrity of the field lines as the ions are accelerated and also protect against stray external fields.

2.5.2 Detectors

The detection of individual charged particles in high vacuum with temporal and spatial accuracy is a formidable technological challenge. Microchannel plates (MCPs) are made of highly resistive material with an array of channels of 5-10 micrometers in diameter, centered around 15 micrometers apart. The channels are slightly angled at 8-10 degrees to ensure that impinging charged particles strike the interior wall of the channel. A positive bias voltage is held across the plate with the spectrometer facing side grounded to 0 V. When a photon or ion strikes the wall of the plate a secondary electron is released. The primary electron is accelerated down the pore

by the bias voltage, with each collision with the walls releasing more and more electrons creating a cascade. This leads to greatly increased signal for the detection of one particle. Depending on the detection efficiencies, multiple MCPs can be stacked together to increase amplification in either a chevron configuration (two MCPS) or z-stack configuration (three MCPs).

In order to image the electrons produced by the microchannel plate, the electrons must be converted into photons. This is achieved by positioning a screen at the end of the MCP stack coated with a material which phosphoresces on impact of an electron, typically P47. The phosphor screen is held at a much higher bias voltage in order to accelerate the clouds of electrons produced by the MCP up to speeds suitable to trigger the phosophor screen. This releases a burst of light which can be detected by a camera.

2.5.3   Camera Technology

The most common type of camera commercially available is based on Charge Coupled Device (CCD) technology[11]. This consists of an array of pixels (reaching into the thousands in both dimensions) each of which consists of a semiconductor which liberates electrons upon absorption of photons and so building up a charge on the pixel. When the camera is triggered, the charge collection begins, at some time later (the aperture time) the camera stops collecting and the lines of pixels are read off one by one. Because this array is sensitive to the amount of charge built up, the relative intensity each pixel was illuminated at is preserved and the information is read off to an external device as a two dimensional array of values with a range corresponding to the bit depth of the camera. The repetition rate of this type of camera is limited by the type of bus used to transport the data to the external device. With typical USB technology, a 1000 x 1000 pixel array could be read off at a rate on the order of hundreds of Hz. As a typical ion imaging experiment using nanosecond lasers operates at a repetition rate of tens of Hz this allows the spatial resolution to be increased a little and for very high quality images to be recorded. As a time of flight spectrum arrives on the order of ten microseconds and the separation of masses occurs on the scale of tens to hundreds of nanoseconds, the repetition rate of CCD cameras is not capable of resolving different mass channels.

The MCP Phosphor Screen assembly can be pulsed on and off on the order of nanoseconds by quickly increasing and decreasing the voltages applied. This allows the experimental sensitivity to be time gated to select, typically, one mass peak to

be imaged at high quality using the CCD camera. In order to image multiple mass peaks simultaneously it is clear a new technology is required. Enter the Pixel Imaging Mass Spectrometry Camera (PImMS).[12–14] PImMS is based upon the Complementary Metal Oxide Semiconductor (CMOS) design as opposed to CCD which allows it to operate as an event-triggered time stamping camera.

While the PImMS camera still contains a 2d array of pixels, the pixels are very different in design to those found in conventional cameras. Rather than building charge, they contain four photodiodes acting as four separate registers. When the camera is triggered alongside the experiment, a master clock is started which ticks 4096 times. The duration of these ticks can be as as short as 6.25 ns but is practicably set to 25 ns to reduce artefacts in the images. When a packet of light (typically between 1-10 photons from a scintillation event on the phosphor screen) strikes the photodiode, if the threshold is greater than a set amount, then the timing of that event is recorded (as a number of 'ticks' passed). This photodiode is then dead for the remainder of the experimental cycle and so each pixel can only record four events per experimental cycle. While this is in principle a limitation of the technology, for the practice of ion imaging where signal levels must be kept relatively low to avoid space charging effects, it is not one.

As well as the timing of the event being recorded, the x, y, coordinates of the pixel are, of course, also recorded. At the end of the experimental cycle an event list is read out through the bus to the computer. This consists of a list of events each with four associated values; x, y, t, bin. Immediately this offers a significant bandwidth improvement for a particle counting experiment where the majority of pixels in a given experimental cycle never see photons and redundant zeroes are passed through the bus, slowing down the transfer of useful information. The 25 ns timing accuracy of the camera now allows the photons associated with each mass peak to be resolved and to be detected simultaneously. As a side note, the upper repetition rate of the experiment is now directly related to the number of events detected per laser shot and the bandwidth of the bus used to read off the data. Two iterations of the PImMS camera feature in this thesis, PImMS1 and PImMS2. Both cameras are almost identical, down to the USB 2.0 bus type, however in PImMS2 a larger sensor is employed increasing the resolution from 72 x 72 pixels (PImMS1) to 324 x 324.

2.5.4 Experimental Timing

Depending on the laser system used, there are two approaches for controlling the timing of the VMI experiments used in this thesis. In the nanosecond VUV ionisation experiment, the master timing is controlled from an eight channel digital delay generator (Berkeley Nucleonics Model 555). The molecular beam is first to be triggered followed by the probe and pump laser flash lamps 13.7 and 199.6 microseconds later. The flashlamp Q-switch delays for the pump and probe lasers were set to 180.0 and 265.8 microseconds, respectively. Because the electronics of the two lasers have different response times, these numbers do not directly reflect the pump probe delay times, however these were chosen to result in a 30 ns delay between the pump and probe laser pulses arriving at the beam (measured with a photodiode). The PImMS camera is triggered next, 331.3 microseconds after the molecular beam. The last two channels have variable time settings. One channel triggers an oscilloscope which displays the trace from a photomultiplier tube pointed at the detector. The final channel triggers the gating module and is regularly manipulated to select mass peaks of interest to image.

The timing of the ultrafast setup is largely the same as that for the nanosecond setup, however the digital delay generator is no longer the master trigger. The overall timing of the delay generator is susceptible to jitter on the picosecond timescale although this does not affect the timing of the channels with respect to one another. To ensure synchronisation with respect to the femtosecond laser pulse, the timing unit which controls the Pockels cells in the ultrafast amplifier is used as the master trigger for the digital delay generator.

2.6 Analysis

2.6.1 Centroiding

It is possible for photons arising from events on the phosphor screen of a scintillating detector to trigger more than one pixel on a camera at a time. In this case, the intensity is double counted, and has to be taken account of. With a two dimensional camera, such as a CCD, this can be done on the fly, however for a PImMS camera the neighbouring events extend not only into the x,y-plane but also in the time dimension. This is a significantly more computationally expensive process and must be done in post processing. The algorithm, adapted from Amini *et. al.* 2015,[15] proceeds as

follows and operates on each laser shot individually:

1. Search through all x,y,t events in a laser shot

2. Compare each event with a preexisting list of clusters (this will be 0 for the first event)

   - If the event is found to be within ± 1 pixel in both the x and y axes and within $\pm \Delta t$ (a value for Δt will be discussed at the end of this section) then add this event to the cluster and move onto the next event to be processed

   - If the event does not satisfy the conditions above for joining a cluster, create a new cluster initialised with this event

3. Iterate through the constructed clusters and centroid each one according to the following rules.

   - Set t_0 as the event in the cluster with the earliest available timecode

   - Calculate the spatial centre of mass of all events in the cluster with all events with each event's contribution to the centre of mass weighted by a factor of $\frac{1}{t-t_0}$

   - At this point the cluster can be rejected if it is outwith certain size limits (the reasons for this will be discussed below)

The exact implementation of centroiding written by myself and Christopher Hansen at Bristol employs various optimisation tricks to significantly increase the performance of the code. A working copy can be found on the research data repository associated with this thesis as well as in the appendix to this thesis.

When processing the centroided data, two parameters can be adjusted, the temporal window in which events are considered part of a cluster δt and the rejection of clusters outwith a certain size.

The inclusion window is typically set to $\Delta t < 3$ in order to allow for skipping over one time bin in the aggregation of clusters. In conversation with the manufacturers of the cameras, the PimMS 2 camera has been reported to sometimes skip a bin and register the event one time bin later. At sensible signal levels, clusters within one time bin are well separated enough to not overlap in time and/or space.

Once the clusters have been identified, the clusters containing only one event (*i.e.* single isolated events) are often rejected. Ions impinging on the phosphor screen are

almost exclusively bright enough to register in multiple pixels and show up as a cluster, particularly if the bias voltage across the phosphor screen is increased and the MCP bias voltage is lowered to keep the the same total signal levels. As such, signal events are more likely to be as a result of scattered photons or background radiation and are deleted.

2.6.2 Time of Flight/Mass Spectrum

As the ions are accelerated by an electric field, they separate according to their mass and, for a given length of spectrometer, arrive at different times as shown by equation 2.1.

$$t = \frac{L}{\sqrt{\frac{2V}{m}}} \tag{2.1}$$

where t is the time of flight of a given particle, m is the mass of that particle, L is the length between the point of ionisation, and V is the field across which the ions are accelerated. Mass spectra recorded as a function of time of flight must have their intensities corrected by an appropriate Jacobian as shown in equation 2.2.

$$f(m) \propto \frac{f(t)}{\sqrt{m}} \tag{2.2}$$

where $f(m)$ is the intensity in mass space, m is the mass and $f(t)$ is the intensity in time of flight space. The full derivation is given in appendix B.1.

2.6.3 Hot Pixels

The PImMS camera is susceptible to over reporting the intensity in certain pixels. The exact origin of this is unclear as it is independent of background light or the camera being coupled to the experiment. On the other hand, it does not appear to arise from background radiation. In the summed ion images these pixels are typically hundreds to thousands of times more intense than their neighbours and as such they can easily be dealt with by the following algorithm. Firstly, a thresholding value, typically 2, was set. The algorithm then scanned through the pixel array. For each pixel it calculates the average of the neighbouring eight pixels. If the value of the pixel is more than the thresholding value multiplied by the average of the neighbouring pixels then this is designated as a hot pixel. The hot pixel's value is discarded and it is set to the average of the neighbours. If the value of the pixel is below the thresholding value multiplied by the average of the neighbouring pixels then the algorithm moves on.

2.6.4   Reconstruction

In the analysis of ion images recorded following UV photodissociation in this thesis, the reconstruction method of choice was Polar Onion Peeling (POP)[16]. Although evidence has shown that the pBASEX method offers more reliable and accurate reconstructions, the speed up offered by POP (in return for a rather modest compromise in quality) is extremely desirable in a multi-mass imaging experiment where a great number of images can be acquired in a short period of time and require fast analysis in order to validate.

2.6.5   Calibration

The velocity map imaging experiment measures the relative positions of particles to their point of origin in polar coordinates. In order to correlate a radius with a velocity for a given fragment, a photodissociation scheme for a well known velocity distribution must be recorded such as the UV photodissociation of O_2. Since the energies of the possible dissociation pathways are known, the bond dissociation enthalpy is well defined and the excitation energy is carefully controlled, the observed radial peaks can be assigned a kinetic energy, and hence their velocities can be calculated and plotted as a function of radius. It should be noted that the velocity to radius ratio changes as a function of time of flight (and so with the mass to charge ratio) as for a given velocity imparted to a particle, heavier particles will take longer to reach the end of the spectrometer and so travel farther in the plane of the detector. The velocity calibration in m s^{-1} pixel^{-1} for a given mass can be transformed to the velocity calibration for another mass as shown in equation 2.3.

$$v_{frag} = v_{cal} * \sqrt{\frac{m_{cal}}{m_{frag}}} \qquad (2.3)$$

where v_{frag} is the velocity calibration of the desired fragment, v_{cal} is the velocity calibration of the fragment used to calibrate the spectrometer and m_{frag} and m_{cal} are their respective masses.

2.6.6   Transformation to TKER Space

As with the time of flight to mass space transformation mentioned in section 2.6.2, the transformation from velocity to TKER also requires the intensities to be transformed

according to a suitable Jacobian as shown in equation 2.4.

$$f(E) \propto f(v)\frac{1}{\sqrt{E}} \tag{2.4}$$

where $f(E)$ is the intensity in kinetic energy space, $f(v)$ is the recorded intensity at the corresponding velocity and E is the kinetic energy of the fragment. This derivation is given in appendix B.2.

2.7 Theoretical Methods

While the Hamiltonian operating on a molecular wavefunction (as shown in equation 1.5) will, in principle, return an exact solution, for many body systems (*i. e.* greater than 3 particles) analytical solutions to the equation are impossibly complex. As discussed in section 1.2.2, one approach to simplify this problem is the separation of the nuclear and electronic components of the wavefunction as in the Born-Oppenheimer equation discussed in section 1.2.2. The residual electronic wavefunction that must be solved is, however, still subject to the many body complexity. As such, approximate methods must be implemented.

2.7.1 Hartree-Fock theory

Hartree-Fock theory (HF) revolutionised *ab initio* quantum computational chemistry paving the way for the development of much more complex and accurate methods. It begins with a model for the wavefunction that stipulates that the total wavefunction $\mathbf{\Psi}$ can be represented as a product of individual one electron wavefunctions ψ as shown in equation 2.5, known as the Hartree product.[17;18]

$$\mathbf{\Psi} = \psi_1\psi_2\psi_3...\psi_N \tag{2.5}$$

This implies that the one electron wavefunctions are independent of one another, which is clearly an incorrect assumption. More specifically the one electron wavefunction is an electron in a given set of space and spin coordinates $\phi = (\mathrm{r},\ \omega)$, where ω can be spin up or spin down (sometimes referred to as α or β). For a two electron problem this manifests as follows

$$\Psi = \psi_1(\phi_1)\psi_2(\phi_2) \tag{2.6}$$

As electrons are fermions, swapping any two electrons should result in a change in the symmetry of the wavefunction as shown in equation 2.7.

$$-\Psi = \psi_1(\phi_2)\psi_2(\phi_2) \tag{2.7}$$

Within the simple Hartree product formulation, this is not guaranteed. By representing these wavefunctions as a Slater determinant, the wavefunction becomes antisymmetric with respect to exchange of any two electrons as shown for a two electron system in equation 2.8.

$$\Psi = \frac{1}{\sqrt{2}} \begin{vmatrix} \psi_1(\phi_1) & \psi_2(\phi_2) \\ \psi_1(\phi_2) & \psi_2(\phi_1) \end{vmatrix} \tag{2.8}$$

In the Born-Oppenheimer approximation, the energy of the system can be defined as a sum of four parts: The Coulombic repulsion between the nuclei which has no electronic wavefunction dependence; the kinetic energy of the electrons and the Coulombic attraction between the nuclei and the electrons which both have a 1-electron dependence; and finally, the Coulombic repulsion between the electrons which is a two-electron expression.

As the kinetic energy of the electrons and the Coulombic attraction between the electrons and the nuclei are both one electron terms, they can be compressed into a single one electron operator where the motion is calculated as a function of a field of the charge of the rest of the particles. This is known as the mean field approximation.

Thus the Hamiltonian can be expressed as follows

$$\hat{H} = \hat{V} + \sum_i^{N_{elec}} \hat{h} + \sum_{i<j}^{N_{elec}} \hat{g}_{ij} \tag{2.9}$$

where $\hat{V}$ is the internuclear repulsion operator, $\hat{h}$ is the one electron integral operator, and $\hat{g}$ is the two electron integral operator. Rearranging equation 1.5 by projecting through with $\langle\Psi|$ we arrive at an expression for the energy as shown in equation 2.10 which shows that the energy of the system is the expectation value of the integral over the wavefunction with respect to the Hamiltonian.

$$E = \langle\Psi|\,\hat{H}\,|\Psi\rangle \tag{2.10}$$

By inspection of equations 2.9 and 2.10 we can see that the expression for the energy can be modified exclusively by adjusting electronic coordinates. We also know that

the true energy of a system E_0 will be the lowest possible energy, and so for any given set of electronic wavefunction coordinates the computed energy will be greater than the true energy. Using this, we can find a solution to the electronic wavefunction iteratively by exploring the parameter space of the electronic wavefunction coordinates to find the lowest energy configuration. This is known as the "Variational Theorem" and solving for the lowest energy wavefunction in this manner is termed the "self consistent field" method.[19]

2.7.2   Basis Sets

Thus far we have discussed the method for optimising an arbitrary electronic wavefunction by computing the energy of the state. Here, we give consideration to the model used for these wavefunctions. In order for the self consistent field method to be successfully the initial wavefunction needs to be close to the correct answer in order to avoid finding low energy solutions which are non-physical. As the numbers of electrons and nuclei in the system increases, the complexity of the wavefunction increases steeply and thus we need a model for the molecular electronic wavefunction which is easily generated given a set of nuclear coordinates. Here we invoke the approximation that a given molecular orbital can be described as a linear combination of atomic orbitals (LCAO) as shown in equation 2.11.

$$\phi_i = \sum_j^N c_{ji}\alpha_j \tag{2.11}$$

where ϕ_i is the ith molecular orbital, N is the number of basis functions localised on a given nucleus, α_j is the atomic basis function and $c_{j,i}$ is the coefficient of the one electron atomic basis which describes the contribution of that specific atomic basis to the molecular orbital in question.

The molecular orbital is one of the one electron functions which, in turn, forms a basis function for describing the total wavefunction. Choosing a mathematical function for a basis set is based on two main considerations, firstly that the function should describe the radial distribution of the atomic orbital well and secondly that the integral of the function should be easy to compute, preferably analytically.

In early quantum chemistry programs Slater type orbitals were used, where the function consists of two parts: a radial dependence r^l where l is the angular momentum in that axis, and an $e^{\xi r}$, where ξ is the parameter which controls how diffuse the

orbital is. These functions are a very accurate model of atomic orbitals, however their integrals are slow to compute. To improve upon this, Gaussian type orbitals (GTOs) based on combinations of Gaussian functions became commonplace for quantum chemistry calculations. While Gaussians do not give a particular accurate description of atomic orbitals alone, their integrals are particularly quick to compute. This means that an approach which employs many Gaussians can achieve similar accuracy in describing a true atomic orbital as a single Slater function yet the integral is still much faster to compute overall. This resulted in the first widespread type of basis function termed STO-nG where the basis set scales with n - the number of Gaussians used to model a Slater orbital.[20;21]

To improve accuracy while minimising computational cost, the "split-valence" basis sets were developed by Pople.[22;23] These use a reduced number of basis functions for the core orbitals and an increased number for the valence orbitals.

The basis sets mentioned thus far are all optimised at the Hartree Fock level using a single reference wavefunction. For the calculation of excited states, these basis functions may not provide a suitable initial guess. Dunning basis sets are optimised using higher level methods capable of calculating excited states to provide basis sets which converge more quickly in excited state calculations. These are the basis sets used throughout this thesis.

2.7.3   Post-HF Methods

While Hartree Fock theory is a good starting point for electronic structure calculations it consistently over-estimates the energy of systems by failing to capture the full scope of the so called "electron correlation" energy. Electron correlation manifests in many ways, one of which, the anti-symmetry principle, is explicitly treated in HF. However there are at least two other assumptions which contribute to the missing electron correlation energy. One is the mean field approximation which says that the electron electron interaction is modelled by each electron interacting with a field of charge, while the other is that the wavefunction can be modelled by a single Slater determinant - more on that later.[24] Post Hartree Fock methods are a class of methods which extend HF theory to attempt to calculate, or compensate, for the electron correlation energy.

2.7.4   MP2

Möller-Plesset perturbation theory treats the correlation energy as a perturbation to the system where the true energy of the system is exactly equal to the sum of the unperturbed ($\hat{H}_0$) and perturbed ($\hat{H}_p$) Hamiltonians as shown in equation 2.12.

$$\hat{H} = \hat{H}_0 + \lambda\hat{H}_p \tag{2.12}$$

This can be reframed as a Taylor series expansion of the energy and the wavefunction in orders of the perturbation as shown by equations

$$E = E_0\lambda^0 + E_1\lambda^1 + E_2\lambda^2 + ... \tag{2.13}$$

and

$$\Psi = \Psi_0\lambda^0 + \Psi_1\lambda^1 + \Psi_2\lambda^2 + ... \tag{2.14}$$

If the expansion is truncated after the first two terms - first order expansion in the series - then this is exactly identical to the Hartree Fock theory described in section 2.7.1. By incorporating the third term, which varies with the square of the perturbation we arrive at the so called second order Möller Plesset equation (MP2).[25] In principle considering more and more terms should converge on the correct answer but the computational cost increases sharply with the order of the correction. It should be noted that while the first order expansion (HF theory) is an upper bound for the true energy of the system, there is no guarantee that the second order energy will not overestimate the correlation energy and be corrected by a higher order term. As such, the wavefunction cannot be optimised variationally under MP2.

2.7.5   Multireference Configuration Interaction

The methods described thus far have all been "single reference" methods, which is to say that they take a single reference wavefunction, in the form of a Slater determinant, and optimise the wavefunction. For the calculation of a single geometric point, this approach is often sufficient, however in exploring the possible geometric configurations of a molecule, different regions of the potential energy surface may be better described by different Slater determinants. As well as changing nuclear configurations, different electronic states are also best described by different Slater determinants.

To overcome this, the wavefunction is expanded as a sum of all possible Slater

determinants of a system referred to as configuration state functions (CSFs) and thus the energy of the system becomes a sum of the energies of the individual CSFs calculated using the same self consistent field approach as in Hartree Fock theory. This is known as the Multireference Configuration Interaction method (MRCI).[26]

As the size of the system increases, the computational effort required to solve for all these different configurations increases exponentially and so the method becomes intractable. Clearly for any given problem, not all CSFs will be relevant to an accurate solution and so, rather than sum over all CSFs for a system (a so called "Full Configuration Interaction" calculation), a subset of CSFs can be used. The subset of CSFs chosen are referred to as the "active space" of the system giving the Complete Active Space Self Consistent Field method (CASSCF). By careful consideration of the active space of a system, one can vastly reduce the number of CSFs, lowering the computational time while suffering only a minimal reduction in accuracy.

Choice of active space is a non-trivial and, to some extent, mysterious practice. Clearly choosing individual CSFs is meaningless and so instead a set of molecular orbitals are chosen, with the CSFs included being the determinants which contribute to the formation of those orbitals.

Selection of molecular orbitals is much more intuitive and can be readily adapted to the problem we wish to study. Consider the photodissociation of H_2S to yield H + SH. The highest occupied molecular orbital is an out of plane p orbital localised on the central sulfur and the dissociation must involve a σ^* orbital so these must be the basis of the dissociation. The excitation to the σ^* orbital is formally forbidden and happens via the π^* orbital and so these three orbitals form a minimum active space for describing the dissociation process. As it turns out, there is a significant contribution from the Rydberg-like sulfur centered 4s orbital and so inclusion of this within the active space will improve the quality of the calculation.[27;28]

2.7.6 Complete Active Space with a Perturbative Correction

Much in the same way the single reference Hartree Fock can be improved upon by estimating the correlation energy by treatment as a perturbation, multireference wavefunctions can also be expanded in a Taylor series to estimate the remaining correlation energy. As the CASPT2 methods are less robust with respect to poor initial guess wavefunctions, and computationally expensive, they are typically only used for single point energy calculations at specific geometries using wavefunctions previously optimised by CASSCF.

Bibliography

[1] G. Scoles, *Atomic and Molecular Beam Methods*, vol. 1 & 2 (Oxford University Press, 1988), ISBN 0195042808.

[2] S. Y. T. van de Meerakker, H. L. Bethlem, N. Vanhaecke, and G. Meijer, Chem. Rev. **112**, 4828 (2012), ISSN 0009-2665.

[3] G. Bjorklund, IEEE J. Quantum Electron. **11**, 287 (1975), ISSN 0018-9197.

[4] R. Mahon, T. McIlrath, V. Myerscough, and D. Koopman, IEEE J. Quantum Electron. **15**, 444 (1979), ISSN 0018-9197.

[5] E. B. Saloman, J. Phys. Chem. Ref. Data. **33**, 765 (2004), ISSN 0047-2689.

[6] A. H. Kung, J. F. Young, and S. E. Harris, Appl. Phys. Lett **22**, 301 (1973), ISSN 0003-6951.

[7] J. M. Gray, J. A. Bossert, Y. Shyur, and H. J. Lewandowski, Phys. Rev. A **96**, 023416 (2017), ISSN 2469-9926.

[8] G. S. Kell, G. E. McLaurin, and G. C. Ford, Rev. Sci. Instrum. **37**, 802 (1966), ISSN 0034-6748.

[9] B. Marchetti, T. N. V. Karsili, O. Kelly, P. Kapetanopoulos, and M. N. R. Ashfold, J. Chem. Phys. **142**, 224303 (2015), ISSN 0021-9606.

[10] E. Wrede, S. Laubach, S. Schulenburg, A. Brown, E. R. Wouters, A. J. Orr-Ewing, and M. N. R. Ashfold, J. Chem. Phys. **114**, 2629 (2001), ISSN 0021-9606.

[11] W. S. Boyle and G. E. Smith, Bell System Technical Journal **49**, 587 (1970), ISSN 0005-8580.

[12] A. Nomerotski, S. Adigun-Boaye, M. Brouard, E. Campbell, A. Clark, J. Crooks, J. J. John, A. J. Johnsen, C. Slater, R. Turchetta, et al., Nucl. Instrum. Methods Phys. Res., Sect. A. **633**, S243 (2011), ISSN 0168-9002.

[13] J. J. John, M. Brouard, A. Clark, J. Crooks, E. Halford, L. Hill, J. W. L. Lee, A. Nomerotski, R. Pisarczyk, I. Sedgwick, et al., J. Instrum. **7**, C08001 (2012), ISSN 1748-0221.

[14] A. T. Clark, J. P. Crooks, I. Sedgwick, R. Turchetta, J. W. L. Lee, J. J. John, E. S. Wilman, L. Hill, E. Halford, C. S. Slater, et al., J. Phys. Chem. A. **116**, 10897 (2012), ISSN 1089-5639.

[15] K. Amini, S. Blake, M. Brouard, M. B. Burt, E. Halford, A. Lauer, C. S. Slater, J. W. L. Lee, and C. Vallance, Rev. Sci. Instrum. **86**, 103113 (2015), ISSN 0034-6748.

[16] G. M. Roberts, J. L. Nixon, J. Lecointre, E. Wrede, and J. R. R. Verlet, Rev. Sci. Instrum. **80**, 053104 (2009), ISSN 0034-6748.

[17] D. R. Hartree and M. M. Black, Proc. Roy. Soc. A **139**, 311 (1933), ISSN 1364-5021.

[18] D. R. Hartree, W. Hartree, and B. Swirles, Philos. Trans. Royal Soc. A **238**, 229 (1939), ISSN 1364-503X.

[19] S. F. Boys, Proc. Roy. Soc. A **200**, 542 (1950), ISSN 2053-9169.

[20] W. J. Hehre, R. F. Stewart, and J. A. Pople, J. Chem. Phys. **51**, 2657 (1969), ISSN 0021-9606.

[21] W. J. Hehre, R. Ditchfield, R. F. Stewart, and J. A. Pople, J. Chem. Phys. **52**, 2769 (1970), ISSN 0021-9606.

[22] J. S. Binkley, J. A. Pople, and W. J. Hehre, J. Amer. Chem. Soc. **102**, 939 (1980), ISSN 0002-7863.

[23] M. S. Gordon, J. S. Binkley, J. A. Pople, W. J. Pietro, and W. J. Hehre, J. Amer. Chem. Soc. **104**, 2797 (1982), ISSN 0002-7863.

[24] P.-O. Löwdin, Phys. Rev. **97**, 1509 (1955), ISSN 0031-899X.

[25] C. Moeller and M. S. Plesset, Phys. Rev. **46**, 618 (1934), ISSN 0031-899X.

[26] B. Liu, J. Chem. Phys. **58**, 1925 (1973), ISSN 0021-9606.

[27] B. Heumann, R. Dren, and R. Schinke, J. Chem. Phys. **180**, 583 (1991), ISSN 0009-2614.

[28] B. Heumann, K. Weide, R. Dren, and R. Schinke, J. Chem. Phys. **98**, 5508 (1993), ISSN 0021-9606.

Chapter 3

Coupling Single Photon Ionisation and Multi-Mass Imaging[1]

3.1   Introduction

The ideal experiment for studying isolated chemical dynamics processes would be universal in nature, enabling detection and characterisation of all photofragment distributions with quantum state resolution. The experiment would operate in a manner which is entirely independent of the molecular structural motifs and of the type of process being studied, be it photodissociation or molecular collisions. The development of the photofragment translational spectroscopy experiment, for which Herschbach and Lee shared the Nobel prize (with Polanyi) in 1986, provided a platform which catalysed a vast field of research into the chemical dynamics of isolated gas phase molecules. Photofragment translational spectroscopy involves crossing a molecular beam with either another molecular beam - for collisional studies - or a laser pulse - for photodissociation studies - in the centre of a chamber held at high vacuum. In the original version, an electron impact mass spectrometer is then rotated around the molecular interaction point at a fixed radius with the time between the collision and the ionisation varied to collect a mass spectrum as a function of the time of flight (or velocity) of the particle. This was initially employed to monitor the products from molecular collisions[1,2] before Kent Wilson introduced pulsed ultraviolet lasers to study photodissociation processes.[3–5]

The photofragment spectrometer is similar to the crossed molecular beam apparatus with one of the collisional arms being replaced by a laser beam. The electron

---

impact mass spectrometer detector is shifted to sitting directly "above" the interaction region with respect to the plane defined by the molecular beam and laser beam and the angular information comes from rotating the polarisation of the laser beam.[3] As these methods were largely developed before or in parallel with the development of more sophisticated lasers which could ionise molecules and molecular fragments (either by a single high energy photon or with high enough photon densities for multiphoton ionisation - section 1.2.7) they initially relied heavily upon electron impact ionisation. Electron impact ionisation, while universal, is a 'hard' ionisation technique and as such is prone to causing secondary fragmentation of the species being detected thus considerably complicating the analysis. The resolution was improved upon by swapping the electron impact ionisation by ionisation using REMPI with microchannel plate detectors. This is a "soft" ionisation process unlikely to cause further dissociation but also has the benefit of being quantum state selective.[6] This quantum state specificity allows a reconfiguration of the experiment, where the ionisation step now takes place within the interaction region rather than following time of flight separation of the photolysis or collisional products according to the kinetic energy. A complementary approach to improve the measurement of the internal energy state populations is to monitor the laser induced fluorescence (LIF) emission following pumping of a sufficiently long lived fluorescent state in one of the photofragments or collision partners.[7] Both approaches, while enabling high resolution measurements, sacrifice the universal detection capability of electron impact ionisation. On top of this, fluoresecence spectra can quickly become complicated, while REMPI is limited in the number of atomic or molecular systems with sufficiently long lived excited states which it can probe and sometimes requires multiple laser pulses.[8;9]

The next significant development in the study of chemical dynamics was the ion imaging and subsequent velocity map imaging apparatus (section 1.2.8) wherein the entire angular distribution of the Newton sphere is recorded simultaneously. This already offers a significant improvement over the rotating mass spectrometer style design of Lee[1] and the polarisation rotation design of Wilson[4] wherein each angle had to be recorded separately, exposing a vulnerability in terms of experimental drifting. The VMI experiment coupled to REMPI represents a gold standard for interrogating photodissociation dynamics of small gas phase molecules and understanding the role and location of conical intersections and complex behaviour on potential energy surface such as roaming.[10;11]

The prospect of coupling a form of universal ionisation to velocity map imaging is a

tantalising one, allowing detailed investigation of dynamics independent of molecular fragment and requiring only one probe laser. While we can acknowledge up front the drawback of losing quantum state specific information (in contrast to a REMPI scheme or fluorescence for example), the advantage of being able to detect multiple masses simultaneously opens an avenue to testing the validity of previous assumptions - the subject of this chapter - and making novel measurements in photochemistry (see chapter 4).

As the ionisation potentials of most radical fragments lie deep into the vacuum ultraviolet (VUV), the generation of VUV photons is required. The earliest efforts to study dynamics using VUV photons relied upon generation via third harmonic generation through either non-resonant or resonant frequency tripling[12–15] or resonant four wave mixing in gases.[16] Although appealing, historically, these were never as widely adopted as they might have been as the efficiency, in terms of photons produced, is relatively low and was difficult to work with on the less sensitive detectors of the time. Synchrotons offered the predominant source of VUV photons for photofragment translational spectroscopy experiments[17;18] or for mass spectrometry studies[19] due to their broad tuneability and high photon fluxes but, obviously, were expensive and complex. Excimer lasers were adopted as cheaper, readily available and easy to use tabletop alternatives.[20–22] Unfortunately, excimer lasers were restricted in the number of wavelengths available and their output polarisation is poorly defined, the cleaning up of which can significantly reduce the photon flux. Beyond translational spectroscopy and mass spectrometric studies, VUV ionisation has seen an application to ion imaging,[23–25] predominantly to study mass channels not accessible by REMPI.[26] Nonresonant or resonant four wave mixing (although ostensibly an older experimental design) exemplifies the best qualities of synchrotron and excimer technologies for VUV generation - tuneability, clean polarisation, and benchtop availability.[27] The lower photon fluxes have been overcome by the design of more sensitive detectors in the form of double stack (chevron configuration) or - in the case of this thesis - triple stack (Z stack configuration) microchannel plate detectors. For imaging experiments, more efficient phosphor coatings (such as P47) have also improved the experimental sensitivity.

To take real advantage of the capability of universal ionisation in combination with VMI the experiment needs to be multiplexed in some way to allow simultaneous measurement of all molecular fragments. This has typically proven challenging because camera technology that can respond on the timescale of the time of flight separation

for molecular fragments ($\sim$ 100s of nanoseconds) has not existed until very recently (see section 2.5.3). Delay Line Detectors[28] offer a mechanism for recording extremely precise arrival times (100s of picoseconds) but allow very little multiplexing, typically being able to detect approximately 10 ions per laser shot. This is ideal for coincidence measurements of the sort used to measure radical photodissociation following photodetachment of anion precursors.[29]

One ingenious approach to multiplexing ion imaging by Lee and coworkers[30] was to extract the ions into a mass spectrometer which separates according to m/z not by time of flight but by deviation as a function of an electric field applied transverse to the extraction axis. This separates the m/z peaks spatially and projects them onto a two dimensional detector. This compresses the Newton spheres in the plane of the m/z plane but, crucially, retains the velocity distribution in the out of plane axis. This technique does not recover the entire angular distribution for a given mass peak in a single experiment but does allow characterisation of the velocity distributions of each fragment simultaneously. Technological developments have resulted in fast-framing event counting cameras capable of distinguishing particle events with temporal accuracy of better than 25 ns[31;32] and spatial resolutions of hundreds of pixels while enabling detection of up to thousands of events simultaneously (see section 2.5.3).

This chapter explores coupling single photon ionisation to multimass imaging as a route to a universal experiment for investigating unimolecular photodissociation processes. As can be seen from this introduction, all of the methods that have sought to expand the capabilities of dynamics experiments towards a universal experiment come with their individual drawbacks and this experiment is no exception. However, the coupling of single photon ionisation (SPI) and the pixel imaging mass spectrometry (PImMS) camera represents a marked step forward in simultaneous measurements and presents an exciting opportunity to explore new dynamics (see chapters 4 & 5). The particular focus of this chapter is to investigate the complications arising from single photon ionisation and the difficulties of coupling this to multimass imaging by investigating the photodissociation dynamics of Dimethyl Sulfide (DMS), the prototypical thioether. The UV photodissociation of DMS has been thoroughly investigated in the past by probing the methyl photofragment (M) which is amenable to REMPI but the methylsulfide (MS) photofragment is not and this chapter reports the first observation of the MS fragment.

3.2 Experimental

The individual components of the experiment have been described in chapter 2 and this section only aims to outline the specific configuration and conditions employed in the experiments detailed in this chapter. Dimethyl sulfide (DMS) (Sigma–Aldrich, >99 % pure) seeded in helium (1 % concentration, 800 mbar backing pressure) was expanded through a pulsed valve (General Valve Series 9) in to a source vacuum chamber held at a base pressure of 7×10^{-8} mbar. The central, coldest portion of the molecular beam was selected by a conical skimmer with a 1 mm orifice *en route* to a differentially pumped, cryogenically cooled, main chamber held at a base pressure of 9×10^{-8} mbar. The molecules then passed through an orifice (~ 3 mm) in the centre of a repeller plate into an interaction region between the repeller and extractor plates. The molecular beam, which defines the z-axis, was then crossed by a photolysis laser beam ($\lambda = 222.5 - 227.5$ nm) generated as the second harmonic of the output from a dye laser (Sirah Cobra Stretch) loaded with Coumarin 450 (Exciton) and pumped by the third harmonic ($\lambda = 355$ nm) of a Nd:YAG laser (Spectra-Physics GCR-250) and focussed using a lens with a focal length of 20 cm. 30 ns later, a Vacuum Ultraviolet (VUV) probe beam ($\lambda = 118.2$ nm) crossed the molecular beam, counter propagating the pump beam. The VUV beam was generated as the 9th harmonic of a Nd:YAG laser (Continuum Surelite II) by first generating the third harmonic ($\lambda = 355$ nm) of the Nd:YAG laser and focussing this through a lens with a 30 cm focal length into a tripling cell filled with a phase matched mixture of xenon (N5.0 grade, BOC Industrial Gases) and argon (N6.0 grade, BOC Industrial Gases) (expanded upon in section 2.4.2). The resultant 118.2 nm and residual 355 nm photons were then refocussed into the interaction region through a custom lithium fluoride lens (Eksma Optics) with a focal length of 14 cm at 118.2 nm and focussed 2 centimetres past the molecular beam. The axis containing both laser pulses was defined as y and both laser pulses were set up to be linearly polarised along the x axis (out of the yz plane formed by the laser beams and the molecular beam) by default. A double Fresnel rhomb was inserted in both beam lines in order to rotate the polarisation through the xz plane.

Nascent cations were extracted from the interaction region along the z-axis using a set of velocity map imaging optics (section 2.5) with the voltages set to Repeller = 3000 V, Extractor = 2460 V and lens = 1662 V before entering a 46 cm field free drift region. After separation according to their mass to charge ratio (m/z), the ions

impacted on a position sensitive detector comprising a triple stack of MCPs coupled to a P47 phosphor screen (Photek VID340). The voltage applied to the MCPs was pulsed by 500 V to switch the detector sensitivity on for the arrival times of ions of interest. The phosphor screen was imaged by a PImMS2 sensor[31;33;34] with the time resolution set to 25 ns which comprised 8-10 slices through each m/z of interest.

The (x, y, t) event list data were centroided according to the algorithm in section 2.6.1 to reduce clusters to single events. Mass spectra were created by binning all events into a 1 dimensional array with each element representing a time bin then converted from time of flight space to m/z space according to a known calibration and correcting the intensities according to an appropriate Jacobian transformation. Ion images were constructed by binning all events within the time slices associated with a single m/z peak into a two dimensional array according to their x, y coordinates. The resulting image was treated for disproportionately intense pixels by identifying pixels with more than twice the intensity of the average of their eight neighbours and setting the intense pixel to the average of their neighbours. Following this, the crushed images were reconstructed using a Polar Onion Peeling algorithm[35] to retrieve the infinitesimally thin central slice. The angular distribution of any feature of interest was fitted to a second order Legendre polynomial characterised by a single anisotropy parameter (β).

For the supporting calculations, the geometry of the DMS molecule was optimised using the ground electronic wavefunction using Møller-Plesset second-order perturbation theory[36] with the augmented correlation consistent double zeta basis set (aug-cc-pVDZ).[37] The molecular orbitals were then calculated using state-averaged complete active space self consistent field (SA-CASSCF).[38] The active space, shown in figure 3.1, contained six electrons distributed amongst five orbitals. The first three occupied orbitals consisted of two σ orbitals and an out of plane, sulfur centered, p orbital. The two unoccupied orbitals corresponded to two σ^* orbitals. This active space was used to calculate potential energy cuts at MP2 relaxed coordinates at the CASPT2 level[39;40] with a CASSCF reference wavefunction. An imaginary level shift of 0.5 E_H was applied to the CASPT2 calculation to protect against intruder states and encourage convergence. The thermochemical calculations for the MS–M bond enthalpy was computed using the complete basis set extrapolation methods (CBS-QB3)[41;42] The calculations were undertaken in Molpro 2018[43] and the CBS-QB3 calculations were undertaken in Gaussian 09. The orbitals were visualised using IBOView.[44]

3.3 Results & Discussion

3.3.1 The Electronic Structure of Dimethyl Sulfide

Dimethyl sulfide (DMS) at its ground state equilibrium geometry falls into the C_{2V} point group with its principal axis through the sulfur atom and bisecting the C–S–C plane. The valence orbitals have been investigated by photoelectron spectroscopy and assigned symmetry labels within the C_{2V} point group.[45;46] The highest occupied molecular orbital (HOMO) of the system is an out of plane, non-bonding, p orbital on the sulfur of b_1 symmetry. The HOMO-1 and HOMO-2 are both C–S σ bonding orbitals of b_2 and a_1 symmetry. These match the calculated molecular orbitals in figure 3.1 which also shows the first two unoccupied orbitals. The LUMO is a σ^* orbital extending across the C–S–C frame of b_2 symmetry and the LUMO+1 corresponds to an orbital with mixed σ^* and diffuse 4s Rydberg character located on the sulfur.

The first excited state corresponds to promotion of a b_1 HOMO electron to the b_2 σ^* orbital resulting in an excited state of $^1A_2$ symmetry. In the C_{2V} geometry this excitation is electric dipole forbidden but becomes allowed upon asymmetric stretching of the C–S bonds whereupon the molecular symmetry collapses to C_S symmetry and the symmetry of the excited state becomes A''. In the UV absorption spectrum of DMS shown in figure 3.2, this $\tilde{A}\leftarrow\tilde{X}$ excitation corresponds to a slight shoulder masked under a much stronger absorption feature slightly to the blue. This stronger feature is attributable to promotion of the b_1 HOMO electron to the diffuse 4s orbital of a_1 symmetry resulting in an excited state of symmetry $^1B_1$. This excitation is allowed but also reduces to A'' symmetry following asymmetric stretching of the C–S bonds allowing the two identified excited states to couple strongly. The structure progressing into the blue end of the spectrum is assigned to vibrational structure within the coupled $\tilde{A}/\tilde{B}$ manifold. Higher lying electronic states lie significantly to the blue, and having been identified as two photon resonances in the UV,[47] are outside the scope of this study.

$$CH_3SCH_3 \xrightarrow[\lambda=\ 222.5\ -\ 227.5\ nm]{h\nu} CH_3 + SCH_3 \qquad (3.1)$$
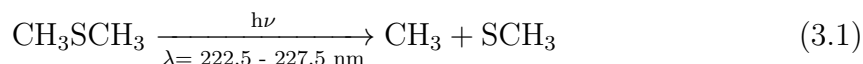
The photolysis of DMS in the region from 230 - 220 nm, as shown in equation 3.1, has been well characterised in the gas phase[48–52] having been interrogated using both TOF-MS and VMI to monitor the methyl fragment following REMPI. Photodissociation in this regime has been shown to involve prompt dissociation of the C–S bond
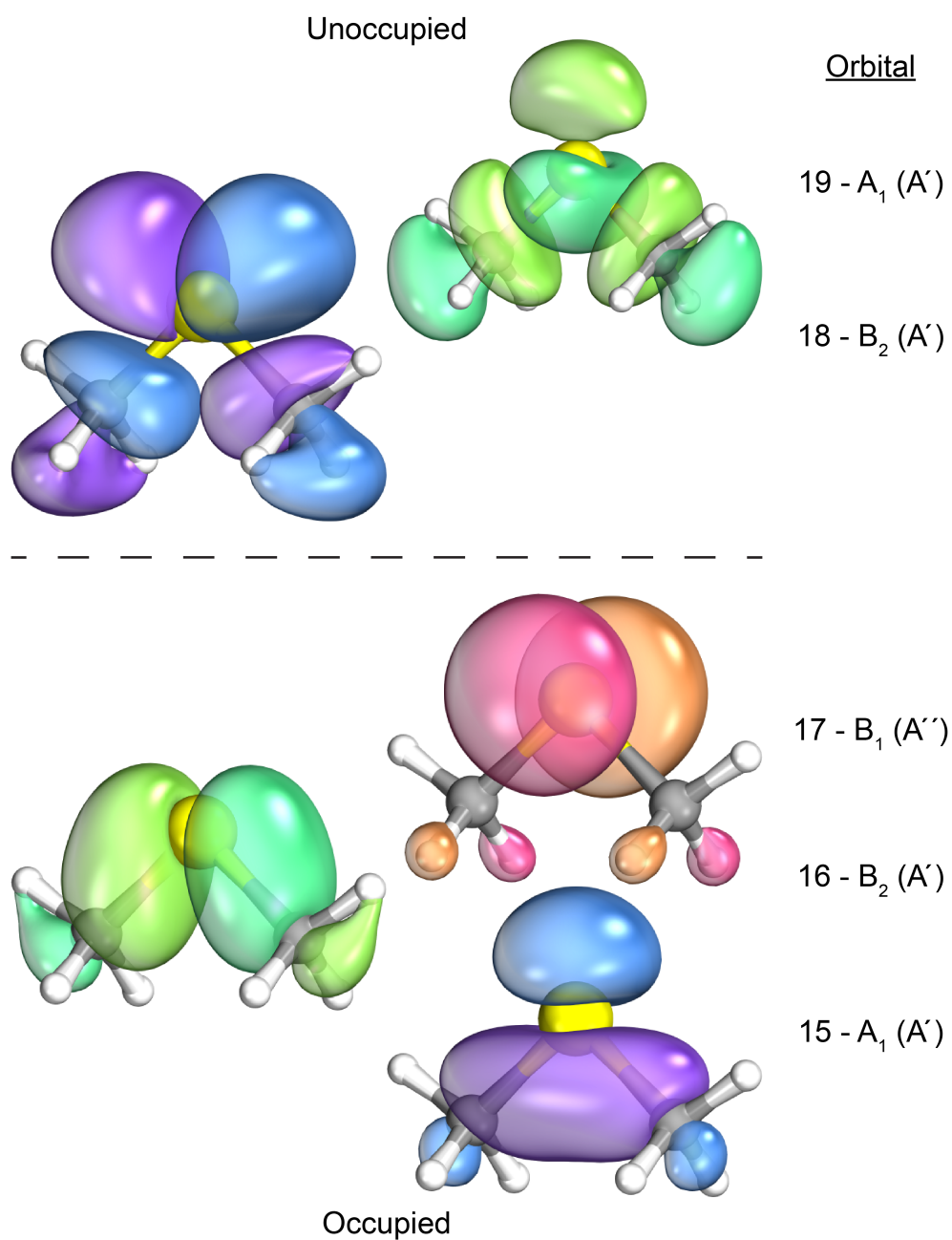
Figure 3.1: Three highest occupied molecular orbitals and two lowest unoccupied molecular orbitals of DMS in its ground electronic state. The orbitals were calculated at the complete active space self consistent field level with an aug-cc-pVDZ basis set based on a ground state geometry optimised at the MP2 level. The bottom and top sections represent the occupied and unoccupied molecular orbitals respectively. The right hand column denotes the ordering of the orbitals and the symmetry character for each orbital in the C_{2V} point group and in the C_S point group in brackets.
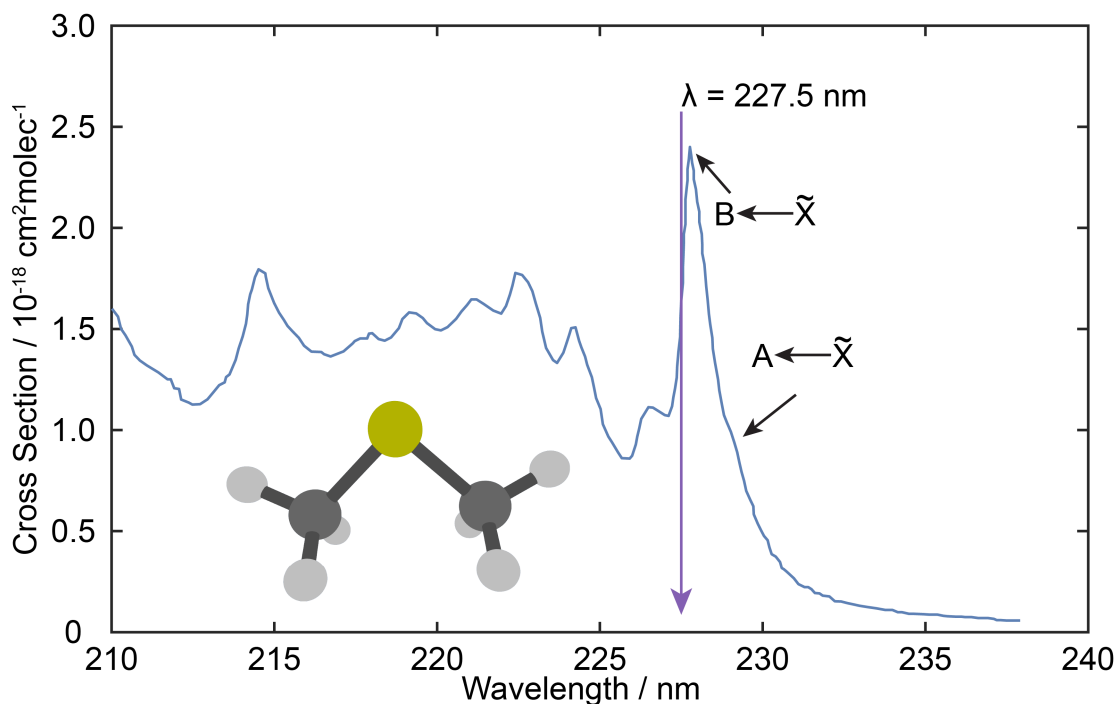
Figure 3.2: Absorption spectrum of Dimethyl Sulfide adapted from Williams *et. al.* 2004.[53] Briefly the DMS was prepared at a partial pressure mixed with N_2 and the absorption cross-sections were recorded between 209.0 and 237.5 nm in an absorption cell using a diode array spectrometer following irradiation by the output from a deuterium lamp. The total pressure was varied and the pressure was monitored via a manometer attached to the cell.

on a timescale which is short (< 100 fs) in comparison to the rotational period of the DMS and to produce methyl fragments almost exclusively in their ground vibrational state. This makes DMS an ideal molecule for an exploratory study of SPI coupled to multi-mass imaging. The primary photolysis products are all accessible via ionisation with a 118.2 nm (10.5 eV) photon as shown in table 3.1 and, while REMPI studies of the methyl provide confirmation and detailed information about the initial C–S bond fission, they remain blind to the CH_3S and to possible secondary decay channels.

3.3.2 Mass Spectrum

Figure 3.3 shows the m/z spectrum collected following photodissociation of DMS at $\lambda = 227.5$ nm and ionisation using a single photon at $\lambda = 118.2$ nm (in blue), alongside the m/z spectra associated with only the photolysis or ionisation lasers present (in green and red, respectively). These TOF spectra were recorded with the

	IP / eV	$\Delta_f H(n)$ / eV	$\Delta_f H(c)$ / eV
CH_3SCH_3	8.6903 ± 0.0009[54]	-0.22[55]	8.42[55]
CH_3S	9.262 ± 0.005[56]	1.346 ± 0.018[57]	10.62 ± 0.022[56]
CH_3	9.843 ± 0.002[58]	1.552 ± 0.001[59]	11.392 ± 0.001[60]
HCS	7.499 ± 0.005[61]	3.11 ± 0.09[61]	10.52 ± 0.09[61]

Table 3.1: ionisation potentials (IPs) and enthalpies of formation of DMS and of selected fragment species (neutrals and cations - $\Delta_f H(n)$ and $\Delta_f H(c)$, respectively) relevant to the present work.

detector sensitivity set high only for the acquisition period corresponding to the m/z 10 through 60 so as to mostly exclude the parent peak at m/z 62 which, otherwise, would have been disproportionately intense. Peaks in the two-colour spectrum which are coincident with those in either of the one-colour spectra are ignored as arising from dissociative ionisation of the parent. Those peaks that show an enhancement in the presence of both lasers are considered to have arisen from a pump probe process. The most dominant peaks in the two colour spectrum are observed at m/z 15 and 47 which are assigned to CH_3 and CH_3S arising from a direct cleavage of one of the C–S bonds in the parent CH_3SCH_3. As these are the species of most interest they shall be discussed later. There are two smaller features in the spectrum at m/z 45 and at 56/57. The former feature is assigned to HCS^+ arising from the unimolecular decomposition of CH_3S^+ ions (via two competitive pathways) following ionisation as shown in equation.[62;63]

$$CH_3S^+({}^3A_1) \rightarrow HCS^+({}^1\Sigma^+) + H_2({}^1\Sigma_g^+) \tag{3.2}$$
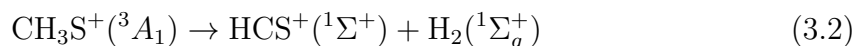
Aschi and coworkers[62] demonstrate theoretically that the elimination can take place via either concerted elimination of H_2 from CH_3S^+ or via first undergoing a 1,2 H migration to form CH_2SH^+ followed by a concerted 1,2 H_2 elimination. Furthermore they deduce that the concerted elimination from CH_3S^+ is most prevalent for cold molecules such as those prepared following molecular beam expansion. The ease of H_2 elimination should, perhaps, come as no surprise as table 3.1 shows that the formation of HCS^+ (10.608 eV) from CH_3S^+ (10.609 eV) is essentially thermoneutral. The study[62] identifies a barrier of 1.39 eV in the concerted H_2 elimination reaction coordinate and a barrier of 0.911 eV in the step wise migration elimination reaction coordinate. The same theoretical study does identify an alternative set of decomposition pathways (both concerted and stepwise migration-concerted) to elimination of
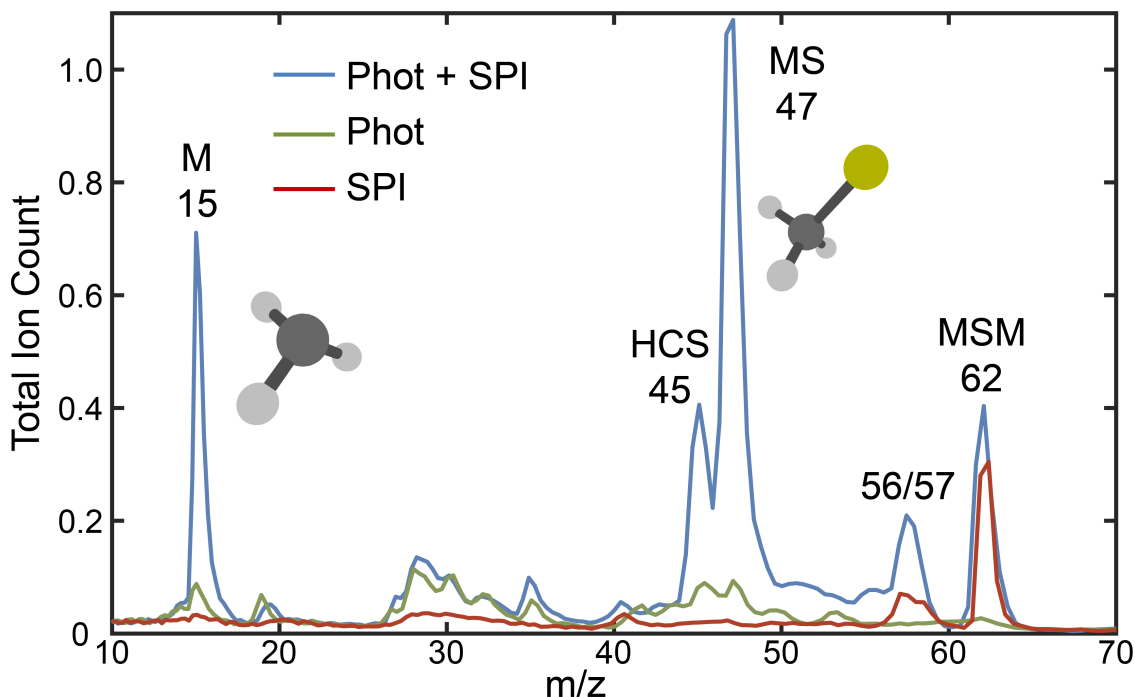
Figure 3.3: Mass spectra derived from TOF spectra measured with the photolysis (λ = 227.5 nm) and SPI (λ = 118.2 nm) laser pulses present in blue and with one or the other of these lasers blocked (red and green as indicated in the inset). The $\boldsymbol{\epsilon}$ vector in all cases was aligned along x, i.e., parallel to the front face of the detector, and the m/z scale has been derived from the measured TOFs assuming that the SPI laser pulse defines time zero. The most abundant ion under all conditions is the parent DMS$^+$ ion at m/z 62, but its detected signal is reduced by ensuring that the detector sensitivity is maximal only for the arrival times corresponding to m/z 10-60.

an H atom. However, these are unlikely as the CH$_2$S$^+$ + H products sit 2.34 eV above the CH$_3$S$^+$ precursor. The feature at m/z 57 is less easily explained. It has also been observed in previous photolysis experiments on 2-bromothiophene (2-BTP)[64] where it was tentatively assigned to the energetically accessible fragmention products HCCS$^+$ and H$_2$CCS$^+$ from the parent 2-bromothiophene.

3.3.3 Total Kinetic Energy Release Spectrum

Returning now to the main peaks of interest in the mass spectrum at m/z 15 and 47, figure 3.4 panels a) and b) show the ion images relating to the CH$_3$ and CH$_3$S photofragments collected following photodissociation of Dimethyl Sulfide at 227.5 nm and universal ionisation at 118.2 nm. Integration of the radial distribution around
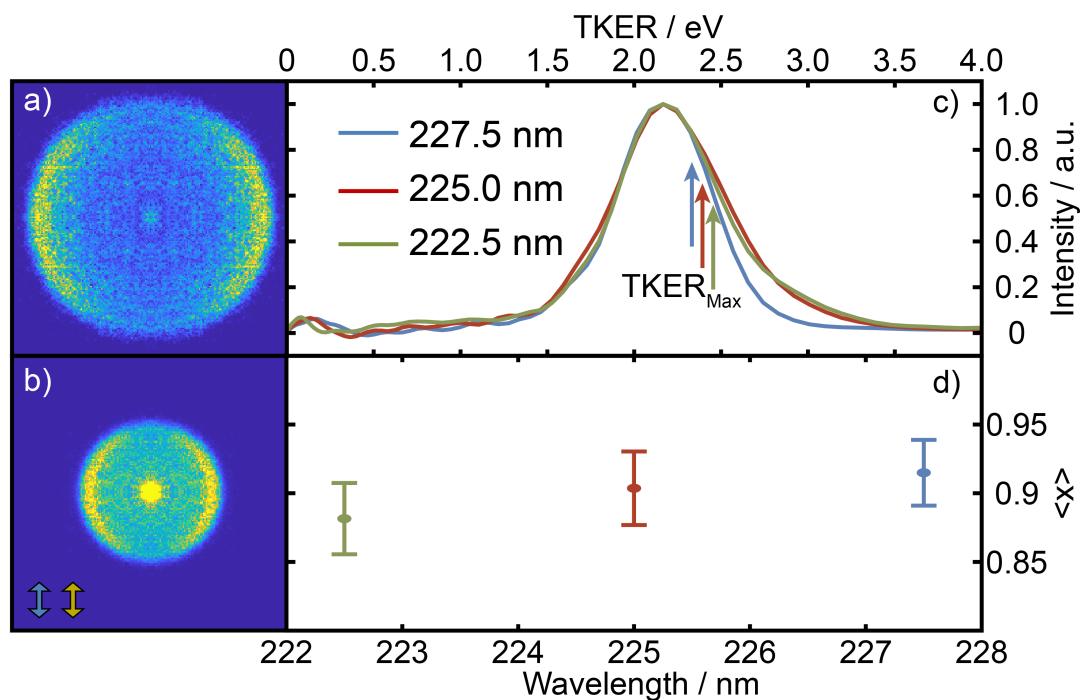
Figure 3.4: Panels a) and b) show crushed, raw ion images of the m/z 15 (CH_3^+) and 47 (CH_3S^+ ion signals following $\lambda = 227.5$ nm photodissociation of DMS and subsequent SPI at $\lambda = 118.2$ nm. Both polarisation vectors are aligned vertically in the image plane as indicated in the bottom left corner of panel b). Panel c) Shows the Total Kinetic Energy Release (TKER) distributions derived from the CH_3S photofragment following photodissociation at either 227.5, 225.0 or 222.5 nm according to the inset key with the TKER max values indicated for the corresponding pump wavelength. Panel d) shows the average available energy deposited into the kinetic energy of the photofragments as a function of pump wavelength.

all angles returns the respective speed distributions which are then converted to the total kinetic energy (TKER) distributions as shown in figure 3.4 c). The TKER distributions show a broad, unstructured peak with an average value of $\sim$2.1 eV and a fast edge at $\sim$2.6 eV. This is consistent with fast dynamical cleavage of the C–S bond on a dissociative potential energy surface. The lack of a tail on the distribution towards 0 TKER indicates that the products are formed in a narrow band of vibrational states. Previous studies[50] have compared the methyl ion images resulting from REMPI of the v=0 vibrational ground state and off-resonance multi-photon ionisation to sample all vibrational states. The distributions were found to match, implying that the methyl is formed predominantly in its vibrational ground state.

Our experiment gives us access to the kinetic energy distribution of not only the

methyl fragment but also that of the methyl sulfide and, as demonstrated in 3.4 c), the distributions from both fragments not only have matching centres but the shapes of the distributions also match. This indicates that, although the methyl sulfide may be formed with a different rovibrational state distribution than the methyl, the internal states are all ionised by 118.2 nm photons with the same ionisation efficiencies. Figure 3.4 charts the average fraction of available energy disposed into translational energy ($\langle x \rangle$) at the three chosen pump wavelengths. This is defined as the ratio of the average value of kinetic energy to the difference between the photon energy and the CH_3–SCH_3 bond enthalpy as shown below.

$$\langle x \rangle = \frac{\text{TKER}_{\text{average}}}{E_{\text{phot}} - D_0} \tag{3.3}$$

where $\text{TKER}_{\text{average}}$ is the average value of the TKER distribution, E_{phot} is the photon energy and D_0 is the bond dissociation energy. These show a general trend of decreasing fraction of translational energy as the photoexcitation energy increases which is consistent with prior observations.[51] This must be interpreted in conjunction with figure 3.4 c) which demonstrates that the peak of the TKER distribution does not change as the pump wavelength is changed. From this, we can deduce that as the molecule absorbs pump photons of higher energy, the extra energy is deposited as internal excitation of the fragments.

From the heats of formation listed in table 3.1 the D_0 value is 3.118 ± 0.019 eV. This gives a maximum allowable TKER value of 2.3 eV. From figure 3.4, the average energy disposed into kinetic energy is ~ 2.1 eV leaving 0.2 eV partitioned into internal degrees of freedom. From the kinematic argument this is likely to be predominantly partitioned into rovibrational excitation of the methyl sulfide fragment.

Figure 3.5 shows the relaxed potential energy cut along the C–S elongation coordinate of DMS. As discussed in section 3.3.1 the first excited state, shown in red, is electric dipole forbidden at C_{2V} geometries. This $\tilde{A}$ state correlates adiabatically with the ground state products at long CH_3–SCH_3 separations whereas the $\tilde{B}$ state is bound in the C–S elongation coordinate. The calculations are undertaken in the C_S point group and demonstrate that along the C–S stretching coordinate the $\tilde{A}$ and $\tilde{B}$ states lie close in energy and are both of the same $^1A''$ symmetry. This indicates a vibronic coupling between the two states in the Franck-Condon region which efficiently funnels flux from the $\tilde{B}$ state to $\tilde{A}$ state.
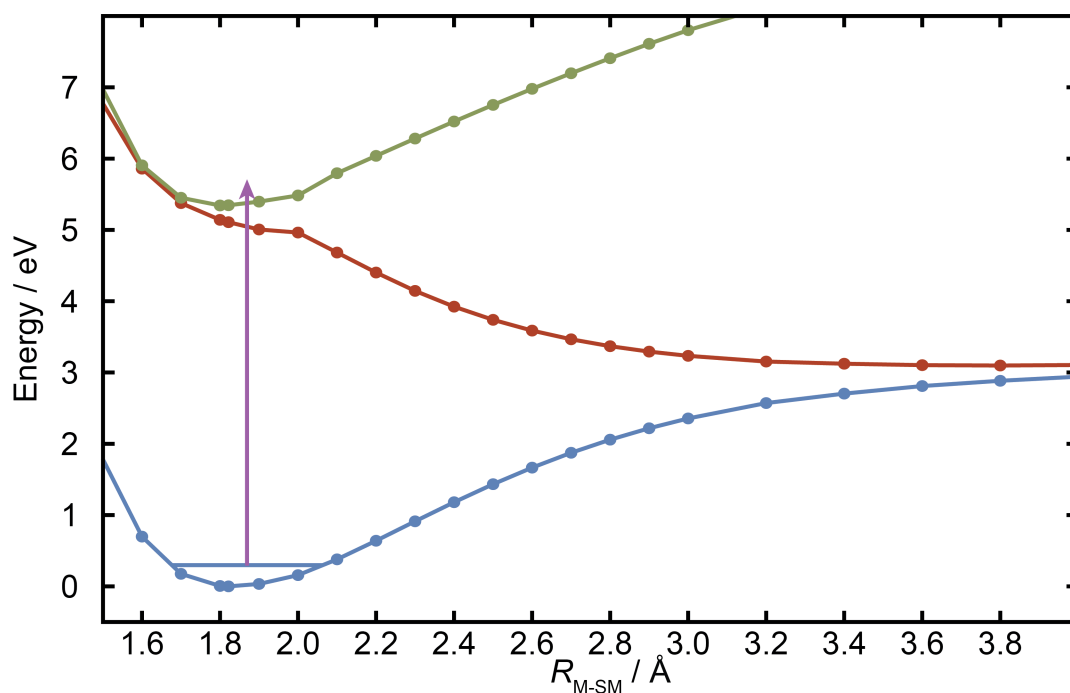
Figure 3.5: Relaxed potential energy cut along the M–S bond elongation coordinate for the ground ($^1A'$) state and first two electronically excited ($^1A''$) states in red and green, respectively. The purple arrow show the energy reached following photoexcitation at $\lambda = 227.5$ from the parent zero-point energy level calculated using the CBS-QB3 method as described in the experimental section.

3.3.4 Discrepancies in the Radial Distributions

The neutral CH_3 and CH_3S products are generated from a common photodissociation (equation 3.1) and, as such, their momentum distributions should match and the TKER distributions derived from either velocity distribution should be identical. This is one of the fundamental assumptions that underpins VMI experiments with a REMPI probe where only one photofragment is detectable as it allows measurement of one photofragment to report on not just its kinetic energy release but on the *total* kinetic energy release in a photodissociation. The momentum distributions, as displayed in figure 3.6, broadly match which supports the assumption that, to a first approximation, the product quantum states are all ionised with equal efficiency. Closer inspection of the momentum distributions show that the CH_3S^+ distribution is slightly broader than that of the corresponding CH_3^+ ions. This concerning mismatch is theorised to come from space charging effects at the point of ionisation. Unlike in REMPI experiments, where only one ionic species is formed in the inter-
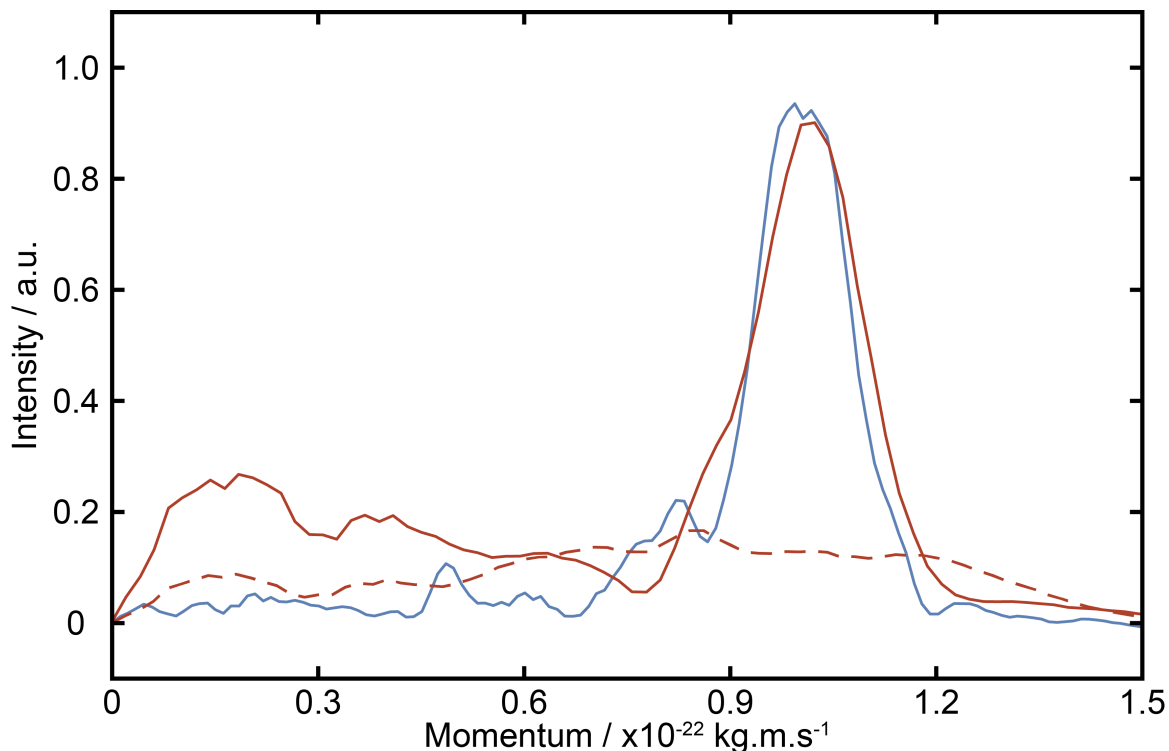
Figure 3.6: Normalised momentum distributions of methyl, methyl sulfide, and HCS in blue, red and dashed red, respectively following photodissociation of DMS at $\lambda = 227.5$ nm and subsequent ionisation at $\lambda = 118.2$ nm.

action region, universal ionisation creates a distribution of ionic species including a large number of parent ions (the relative yield of which is suppressed in figure 3.3 by reducing the detector gain before they arrive). In REMPI experiments performed under conditions where the ionisation laser is too intense, so called "space charging" effects can impact the resolution by the Coulombic interactions between the high density of charged species perturbing the nasecent velocity distributions of the neutral species. Single photon ionisation results in a similar effect. At the moment of ionisation, the CH_3 and CH_3S distributions can be considered as nested spherical Legendre polynomial distributions expanding around a nebula of parent molecules. As the field of 118.2 nm photons ionises both primary photofragments simultaneously (as well as parent molecules and any other photofragments produced in the experiment) there are Coulombic interactions between not just ions of the same type, but all nascent ions. As the ions are extracted by the ion imaging optics, the Newton spheres expand and the Coulombic interactions quickly fade as the ion distributions are separated by acceleration by the electric field. The CH_3^+ ions, as the fastest moving with the largest Newton sphere, escape the influence of the other ions most quickly and so their radial distribution is less affected leading to a less blurred, thinner radial distribution.

The CH_3S^+ spend more time interacting with the parent ions on top of their initial interactions with the CH_3^+ and so their radial distribution is further broadened. In section 3.3.2 we discussed the potential for the CH_3S photofragments to undergo dissociative ionisation to form $HCS^+ + H_2$. The momentum distributions shown in figure 3.6 are broad and the centre of the distribution is coincident with the centre of the CH_3S momentum distribution.

3.3.5 Fragment Angular Distributions

The expectations of momentum matching applied to the radial distributions must hold true to apply to the angular distributions as well. The ion images shown in figure 3.7 a) and b) correspond to a common pair of methyl and methyl sulfide photofragments arising from photodissociation at $\lambda = 227.5$ nm and ionisation at $\lambda = 118.2$ nm. The consistency of the conditions under which the ion images were acquired was maintained by monitoring both fragments simultaneously as outlined in the experimental section. The angular distributions of the fast rings in both images, which correspond to the same dissociation process as confirmed by the momentum matching shown in figure 3.6, should be described by fitting the same β value to the model for angular anisotropy shown in equation 1.29 in section 1.3.2. The angular distributions of the the methyl and methyl sulfide, in blue and red respectively, (integrated across the fast feature in the reconstructed central slice) are shown in figure 3.7 panel c) in a scatter plot and the fits to the model for photofragment angular distribution (equation 1.29) are shown in a solid line with the β values inset. Rather disturbingly, these do not match. This is qualitatively obvious from visual inspection of the distributions and confirmed by the best fit β parameter for the CH_3 and CH_3S fragments are -0.77 $\pm$ 0.03 and -0.50 $\pm$ 0.04, respectively.

The β value for the methyl fragment can be directly compared with the prior literature and is reassuringly consistent with previous values of -0.85 $\pm$ 0.05[49] and -0.70 $\pm$ 0.10[52] and supports these prior conclusions that the dissociation is prompt and that it follows an excitation with a transition dipole extending out of the plane defined by the C–S–C atoms in the parent DMS. The photodissociation process is identical in this experiment and as well as in the literature[49;52] (absorption of a single 227.5 nm linearly polarised generated from the SHG of a tuneable dye laser - see section 3.2) and so no suspicion is cast there. The ionisation step is, however, different and its interaction with the methyl and methyl sulfide photofragments may be different and it is here that suspicion is cast. In the previous literature the methyl fragment

Figure 3.7: Panels a) and b) show the methyl and methyl sulfide ion images, respectively, collected following photodissociation of DMS at $\lambda = 227.5$ nm and subsequent ionisation at $\lambda = 118.2$ nm. Both the photolysis and ionisation laser have their electric vectors aligned vertically in the plane of the image with $\phi = 0°$. Panel c) shows the angular distribution around the fast component in the methyl and methyl sulfide images in blue and red respectively alongside plots of the fit to the function outlined in equation 1.29.

was ionised by REMPI through the $4p_z\,^2A_2''$ Rydberg state at 286.3 nm while in these experiments it was ionised by a linearly polarised non-resonant single photon at $\lambda = 118.2$ nm. As the β value extracted for the methyl fragment is consistent between REMPI and SPI schemes, it is sensible to conclude that SPI at least has the potential to capture the angular distribution and does so effectively for methyl. Unfortunately, no REMPI scheme currently exists for the CH_3S fragment in order to make a direct comparison.

The representation of the photodissociation shown in figure 3.8 highlights how the electric vector of the UV light $\boldsymbol{\epsilon}_{phot}$ interacts with the parent transition dipole moment $\boldsymbol{\mu}_{DMS}$. The thick black single headed arrow demonstrates the dissociation vector for the C-S bond for the particular molecular conformation shown but the ensemble of molecular configurations can be distributed anywhere around the grey circle. With the electric vector of the light aligned parallel to the face of the detector this gives rise to a distribution characterised by a negative β value. As such, the forces which drive the fast C–S bond fission and the resultant velocity vectors of the CH_3 and CH_3S
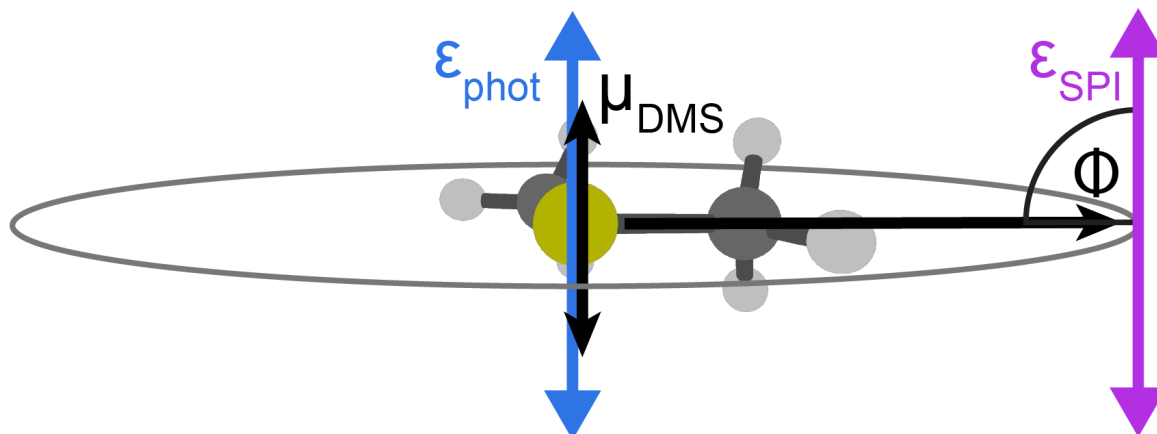
Figure 3.8: Schematic figure showing the relevant laser polarisations (with the photolysis laser in blue and the probe laser in purple) and transition dipole moments for the DMS molecule (as a double headed black arrow). The black single headed arrow shows the dissociation axis for the shown molecular conformation. The grey circle represents the plane into which the photofragments are preferentially distributed and into which the MS fragments are formed aligned.

fragments will be confined to the plane perpendicular to the polarisation vector of the light defined by the grey circle in figure 3.8. Furthermore, the impulsive force of the dissociation will act primarily on the sulfur atom causing the CH_3S fragments to be formed rotationally excited with the rotational angular momentum vector $\boldsymbol{J}_{CH_3S}$ aligned parallel to $\boldsymbol{\mu}_{DMS}$.

In a single photon ionisation process, the transition dipole moment modifies the wavefunction from a neutral state of the radical ($\Psi_{neutral}$) to a cationic continuum state (Ψ_{cation}) as shown in equation 3.4.

$$\boldsymbol{\mu}_{cation \leftarrow neutral} = \langle \Psi_{cation} | \, \hat{\mu} \, | \Psi_{neutral} \rangle \qquad (3.4)$$

In pump - probe experiments where the probe step is SPI there exists a strong preference for ionisation of fragments where the transition dipole moment between ($\Psi_{neutral}$) and (Ψ_{cation}) is aligned with the electric vector of the light. In this case, the ionisation efficiency will be sensitive to the angle between the SPI laser polarisation and $\mu_{cation \leftarrow neutral}$ and thus to the plane of the aligned photofragments. Analogous effects have been observed in REMPI processes where, with careful deconvolution of the anisotropy contributions of the resonant and ionisation steps, the exact alignment of the photofragments can be measured.[65] As SPI discriminates less in the range of systems it can ionise, one could imagine using this in broader studies of photofragment
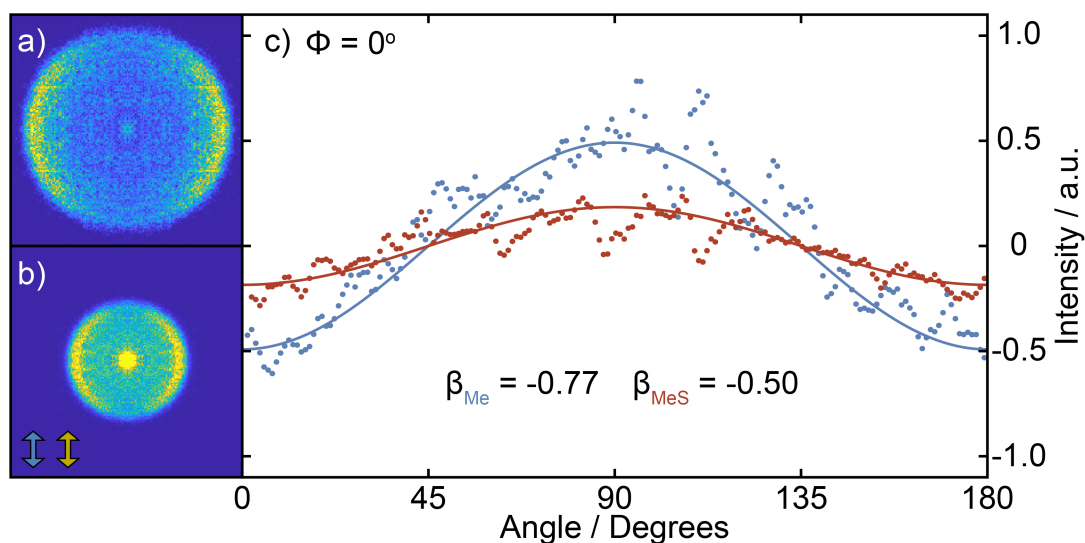
Figure 3.9: Panels a) and b) show the methyl and methyl sulfide ion images, respectively, collected following photodissociation of DMS at $\lambda = 227.5$ nm and subsequent ionisation at $\lambda = 118.2$ nm. The photolysis electric vector is aligned vertically in the plane of the image and ionisation laser has its electric vector aligned out of the plane of the image with $\phi = 90°$. Panel c) shows the angular distribution around the fast component in the methyl and methyl sulfide images in blue and red respectively alongside plots of the second order Legendre polynomials with the β values inset in the image.

alignment.

The pump polarisation was maintained parallel to the plane of the detector and the SPI polarisation was rotated through the xz plane, corresponding to the angle ϕ demonstrated in figure 3.8. Rotating the SPI polarisation to $\phi = 90$ degrees and repeating the same experiment leads to the ion images shown in figure 3.9 a) and b). The angular distributions for the CH_3 and CH_3S fragments under these conditions are shown in panel c in blue and red, respectively. The β parameter which describes the CH_3 distribution remains unchanged at $\beta = $ -0.77 $\pm$ 0.02 but, most interestingly, the CH_3S β parameter has changed from -0.50 $\pm$ 0.04 at $\phi = 0°$ to -0.75 $\pm$ 0.03 at $\phi = 90°$ thus demonstrating that the sampling of the aligned methyl sulfide fragment is sensitive to the polarisation of the SPI photon.

To more fully characterise the dependence, the ion images were recorded at various pump probe polarisation angles between $\phi = 0°$ and 90°. Figure 3.10 shows the trend as the angle between the pump and probe laser polarisation vectors is rotated through
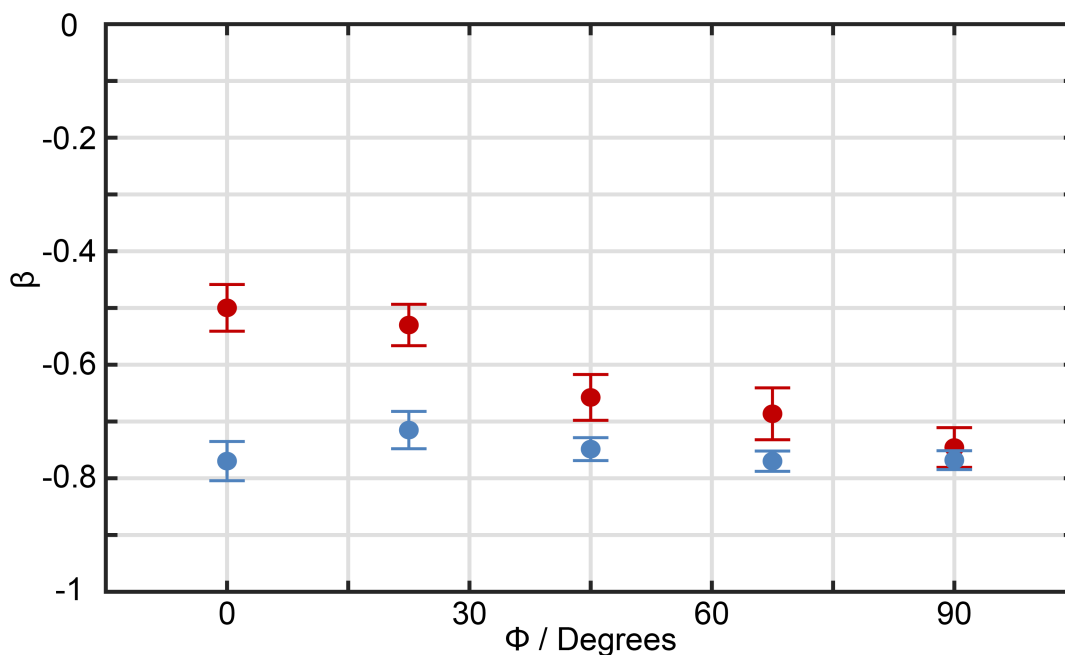
Figure 3.10: β parameters derived by fitting reconstructed images of m/z 15 (CH_3^+, blue) and 47 (CH_3S^+, red) ion signals following $\lambda = 227.5$ nm photodissociation of DMS and subsequent SPI at $\lambda = 118.2$ nm measured with $\boldsymbol{\epsilon}_{phot}$ parallel to x and $\boldsymbol{\epsilon}_{SPI}$ aligned at various ϕ to the x axis. The displayed error bars represent 2σ (95% confidence interval). Angular distributions and the best fits for CH_3^+ and CH_3S^+ data recorded at $\phi = 0°$ and 90° are shown in figure 3.7 c) and figure 3.9 c) respectively.

the angle ϕ. The red points, representing the β parameter for the CH_3S fragment, and the blue points, representing the β parameter that describes the CH_3 distribution, coalesce at $\phi = 90°$. This indicates that the angular distribution is being sampled completely as the result now agrees with the prediction of momentum matching.

As a sanity check, the ion images at $\phi = 0°$ and 90° were also recorded with the polarisation of the pump beam aligned orthogonal to the plane of the detector. As one of the underlying assumptions of VMI is that the photofragment distribution is cylindrically symmetric around the photodissociation axis, it is important to confirm that any issues in measuring the anisotropy do not represent a break in the cylindrical symmetry and that, if they do, the correction also restores the cylindrical symmetry.

Figure 3.11 panels a) and b) show the ion images collected with the electric vector of both the pump and probe lasers aligned out of the plane of the image, as demonstrated by the blue and yellow annuli respectively, in the bottom left corner of the methyl image. The associated angular distributions for the methyl and methyl sulfide

fragments are shown in panel c) in blue and red respectively along with their best fit β values inset. Panels d) and e) show the contrasting ion images with the pump polarisation alignment maintained orthogonal to the plane of the image, as indicated by the blue annulus, but with the probe laser polarisation aligned vertically in the plane of the image. Panel f) shows the angular distributions resulting from analysis of images d) and e) with the best fit β parameters inset as in panel c). Pleasingly, all four distributions are virtually flat as a function of θ with best fit β parameters close to 0 reflecting the isotropic distributions indicative of cylindrical symmetry around the pump laser axis.

3.4   Conclusions

Universal ionisation coupled to multi-mass velocity map ion imaging has been employed to monitor the outcome of the photodissociation of dimethyl sulfide following photodissociation at λ = 227.5, 225.0 and 222.5 nm. An interpretation has been given for the observed lack of change in the average kinetic energy deposited in the photofragments as a function of the pump wavelength based on imaging the methyl sulfide product which has never been imaged before. The average kinetic energy deposited into the fragments was found to not shift as a function of photodissociation wavelength implying that the extra energy was partitioned into internal degrees of freedom of the CH_3S fragment, consistent with the geometry of the molecule which will tend to couple the dissociation coordinate into rotational excitation of the methyl sulfide. Although the excitation is primarily to a diabatically bound state, cuts along the potential energy surface provide evidence for efficient vibronic coupling to a directly dissociative surface and hence a near limiting β value for the fragment recoil anisotropy.

The primary achievement of this chapter is a survey of the validity of single photon ionisation coupled to multimass imaging. Three issues have been identified which have to be considered when carrying out this type of experiment and they are as follows:

i) Dissociative ionisation   With universal ionisation and multi-mass imaging the experiment is sensitive to all species with ionisation potentials less than the energy of the VUV photon. As such, previously unobserved products are revealed such as the primary dissociation product methyl sulfide, as well as products of secondary dissociation, and dissociative ionisation of primary products, none of which were monitored
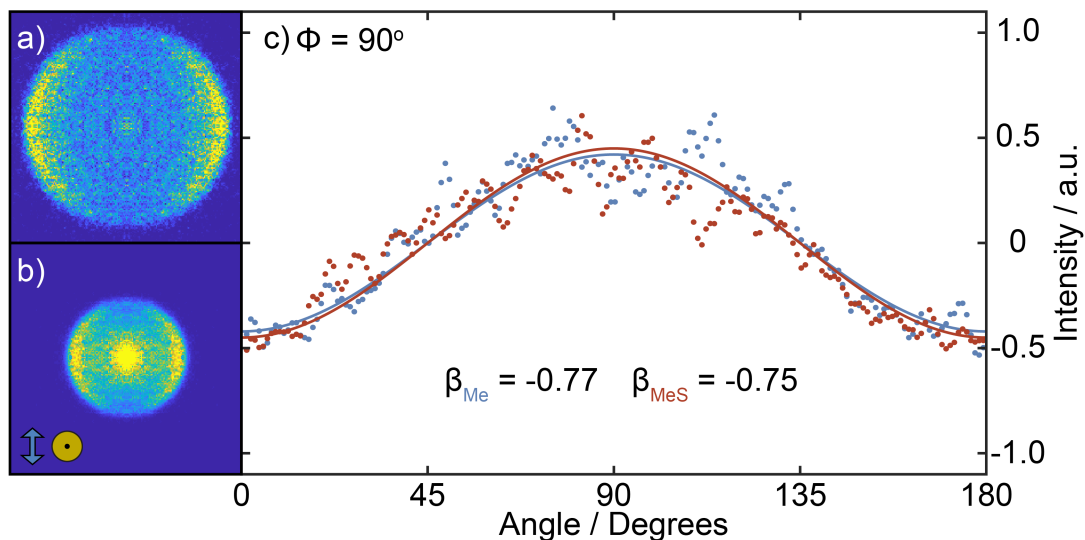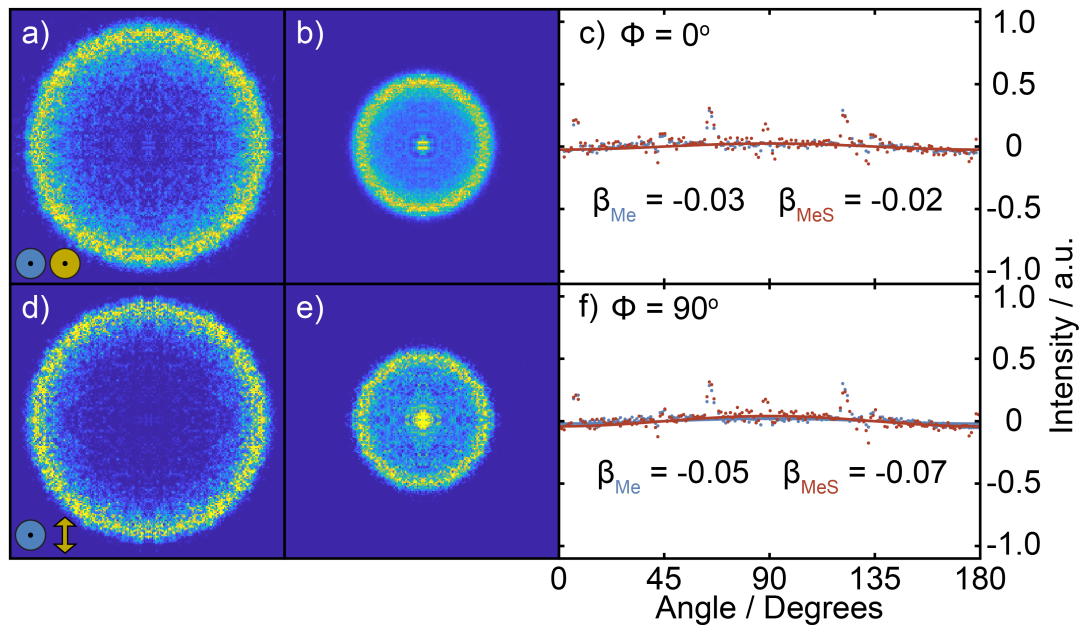
Figure 3.11: Panels a) and b) show the methyl and methyl sulfide ion images, respectively, recorded following photodissociation of DMS at $\lambda = 227.5$ nm and subsequent ionisation at $\lambda = 118.2$ nm. These were recorded with the electric vectors of both the pump and ionisation photons aligned out of the plane of the image with $\phi = 0°$. Panel c) shows the angular distributions of the fast components in the methyl and methyl sulfide in blue and red scatter plots respectively with their fits to a second order Legendre polynomial in solid lines with the β values inset. Panels d) and e) also show the methyl and methyl sulfide ion images, respectively, recorded following photodissociation of DMS at $\lambda = 227.5$ nm and subsequent ionisation at $\lambda = 118.2$ nm. These were recorded with the electric vector of the pump photons aligned out of the plane of the image and the electric vector of the ionisation photon aligned vertically in the plane of the image with $\phi = 90°$. Panel f) shows the angular distributions of the fast components in the methyl and methyl sulfide in blue and red scatter plots respectively with their fits to the model for fragment recoil anisotropy (equation 1.29) shown in solid lines with the corresponding β values inset.

in a REMPI experiment. In order to draw out quantitative information about the yields of products with respect to one another, care must be taken to account not just for the yield of one product but also to consider loss channels through further dissociation.

ii) Space Charging   Radial distributions of Newton spheres are liable to be blurred in a single photon ionisation experiment as a great number of ions are necessarily created in the interaction region. Furthermore, the blurring is not even handed for ions. Those born with greater kinetic energy or those which are lighter will escape the influence of the more central slower or heavier charged particles more quickly through a combination of their Newton sphere expanding more quickly and being separated by time of flight more effectively resulting in less blurring for them overall. Heavier and slower ions spend more time around the dense centre of charged parent ions suffering more significant velocity blurring.

iii) False Anisotropy Measurements   Much like REMPI schemes, which can be used to measure the degree of alignment of molecules to the ionisation light, single photon ionisation can demonstrate a significant sensitivity to fragments born confined in a plane perpendicular to the electric vector of the photodissociation light and which have a strong transition dipole between the neutral and cation states. To alleviate this, the extent to which the SPI step shows an alignment dependence must be checked and the experiment must be undertaken with the SPI photon polarisation aligned well with the transition dipole in order to prevent potential misreporting of β parameters.

The present chapter shows that all of these issues can be overcome, and that universal ionisation and multimass imaging offers an powerful extension and complement to traditional REMPI based VMI experiments. The next chapter shows how the technique enables the measurement of the preference for fission of one bond over another following photoexcitation - a quantification that would have been impossible with tradition VMI experiments.

Bibliography

[1] Y. T. Lee, J. D. McDonald, P. R. LeBreton, and D. R. Herschbach, Rev. Sci. Instrum. **40**, 1402 (1969), ISSN 0034-6748.

[2] D. M. Neumark, A. M. Wodtke, G. N. Robinson, C. C. Hayden, and Y. T. Lee, J. Chem. Phys. **82**, 3045 (1985), ISSN 0021-9606.

[3] G. E. Busch, J. F. Cornelius, R. T. Mahoney, R. I. Morse, D. W. Schlosser, and K. R. Wilson, Rev. Sci. Instrum. **41**, 1066 (1970), ISSN 0034-6748.

[4] S. J. Riley and K. R. Wilson, Faraday Discussion **53**, 132 (1972), ISSN 0301-7249.

[5] J. H. Ling and K. R. Wilson, J. Chem. Phys. **65**, 881 (1976), ISSN 0021-9606.

[6] J. Steadman, S. K. Cole, and T. Baer, J. Chem. Phys. **89**, 5498 (1988), ISSN 0021-9606.

[7] R. D. Bower, R. W. Jones, and P. L. Houston, J. Chem. Phys. **79**, 2799 (1983), ISSN 0021-9606.

[8] G. B. Park, B. C. Krüger, S. Meyer, A. M. Wodtke, and T. Schäfer, Phys. Chem. Chem. Phys. **18**, 22355 (2016), ISSN 1463-9076.

[9] N. Bjerre, R. Kachru, and H. Helm, Phys. Rev. A. **31**, 1206 (1985), ISSN 0556-2791.

[10] D. Townsend, S. A. Lahankar, S. K. Lee, S. D. Chambreau, A. G. Suits, X. Zhang, J. Rheinecker, L. B. Harding, and J. M. Bowman, Science **306**, 1158 (2004), ISSN 0036-8075.

[11] M. S. Quinn, D. U. Andrews, K. Nauta, M. J. T. Jordan, and S. H. Kable, J. Chem. Phys. **147**, 013935 (2017), ISSN 0021-9606.

[12] G. Bjorklund, IEEE J. Quantum Electron. **11**, 287 (1975), ISSN 0018-9197.

[13] R. Mahon, T. McIlrath, V. Myerscough, and D. Koopman, IEEE J. Quantum Electron. **15**, 444 (1979), ISSN 0018-9197.

[14] R. H. Page, R. J. Larkin, A. H. Kung, Y. R. Shen, and Y. T. Lee, Rev. Sci. Instrum. **58**, 1616 (1987), ISSN 0034-6748.

[15] N. P. Lockyer and J. C. Vickerman, Laser Chemistry **17**, 139 (1997), ISSN 0278-6273.

[16] G. Hilber, A. Lago, and R. Wallenstein, J. Opt. Soc. Am. B **4**, 1753 (1987), ISSN 0740-3224.

[17] D. A. Blank, N. Hemmi, A. G. Suits, and Y. T. Lee, Chem. Phys. **231**, 261 (1998), ISSN 0301-0104.

[18] N. Hemmi and A. G. Suits, J. Chem. Phys. **109**, 5338 (1998), ISSN 0021-9606.

[19] C. A. Taatjes, N. Hansen, D. L. Osborn, K. Kohse-Höinghaus, T. A. Cool, and P. R. Westmoreland, Phys. Chem. Chem. Phys. **10**, 20 (2008), ISSN 1463-9076.

[20] P. A. Willis, H. U. Stauffer, R. Z. Hinrichs, and H. F. Davis, Rev. Sci. Instrum. **70**, 2606 (1999), ISSN 0034-6748.

[21] P. A. Willis, H. U. Stauffer, R. Z. Hinrichs, and H. F. Davis, J. Phys. Chem. A. **103**, 3706 (1999), ISSN 1089-5639.

[22] D. R. Albert and H. F. Davis, Phys. Chem. Chem. Phys. **15**, 14566 (2013), ISSN 1463-9076.

[23] S. T. Tsai, C. K. Lin, Y. T. Lee, and C. K. Ni, Rev. Sci. Instrum. **72**, 1963 (2001).

[24] D. Townsend, W. Li, S. K. Lee, R. L. Gross, and A. G. Suits, J. Phys. Chem. A. **109**, 8661 (2005).

[25] K.-C. Lau, Y. Liu, and L. J. Butler, J. Chem. Phys. **123**, 054322 (2005), ISSN 0021-9606.

[26] M. Ahmed, D. S. Peterka, and A. G. Suits, Chem. Phys. Lett. **317**, 264 (2000), ISSN 0009-2614.

[27] M. A. Todt, D. R. Albert, and H. F. Davis, Rev. Sci. Instrum. **87**, 063106 (2016), ISSN 0034-6748.

[28] S. E. Sobottka and M. B. Williams, IEEE Trans. Nucl. Sci. **35**, 348 (1988), ISSN 0018-9499.

[29] K. A. Hanold, A. K. Luong, T. G. Clements, and R. E. Continetti, Rev. Sci. Instrum. **70**, 2268 (1999), ISSN 0034-6748.

[30] C. K. Ni and Y. T. Lee, Int. Rev. Phys, Chem. **23**, 187 (2004), ISSN 0144-235X.

[31] J. J. John, M. Brouard, A. Clark, J. Crooks, E. Halford, L. Hill, J. W. L. Lee, A. Nomerotski, R. Pisarczyk, I. Sedgwick, et al., J. Instrum. **7**, C08001 (2012), ISSN 1748-0221.

[32] T. Poikela, J. Plosila, T. Westerlund, M. Campbell, M. De Gaspari, X. Llopart, V. Gromov, R. Kluit, M. van Beuzekom, F. Zappon, et al., J. Instrum. **9**, C05013 (2014), ISSN 1748-0221.

[33] A. Nomerotski, S. Adigun-Boaye, M. Brouard, E. Campbell, A. Clark, J. Crooks, J. J. John, A. J. Johnsen, C. Slater, R. Turchetta, et al., Nucl. Instrum. Methods Phys. Res., Sect. A. **633**, S243 (2011), ISSN 0168-9002.

[34] A. T. Clark, J. P. Crooks, I. Sedgwick, R. Turchetta, J. W. L. Lee, J. J. John, E. S. Wilman, L. Hill, E. Halford, C. S. Slater, et al., J. Phys. Chem. A. **116**, 10897 (2012), ISSN 1089-5639.

[35] G. M. Roberts, J. L. Nixon, J. Lecointre, E. Wrede, and J. R. R. Verlet, Rev. Sci. Instrum. **80**, 053104 (2009), ISSN 0034-6748.

[36] C. Moeller and M. S. Plesset, Phys. Rev. **46**, 618 (1934), ISSN 0031-899X.

[37] T. H. Dunning, J. Chem. Phys. **90**, 1007 (1989), ISSN 0021-9606.

[38] H. Werner and P. J. Knowles, J. Chem. Phys. **82**, 5053 (1985), ISSN 0021-9606.

[39] K. Andersson, P. A. Malmqvist, B. O. Roos, A. J. Sadlej, and K. Wolinski, J. Phys. Chem. **94**, 5483 (1990), ISSN 0022-3654.

[40] K. Andersson, P. Malmqvist, and B. O. Roos, J. Chem. Phys. **96**, 1218 (1992), ISSN 0021-9606.

[41] G. P. F. Wood, L. Radom, G. A. Petersson, E. C. Barnes, M. J. Frisch, and J. A. Montgomery, J. Chem. Phys. **125**, 094106 (2006), ISSN 0021-9606.

[42] M. R. Nyden and G. A. Petersson, J. Chem. Phys. **75**, 1843 (1981), ISSN 0021-9606.

[43] H.-J. Werner, P. J. Knowles, G. Knizia, F. R. Manby, M. Schütz, P. Celani, W. Györffy, D. Kats, T. Korona, R. Lindh, et al., *MOLPRO, version 2018.1, a package of ab initio programs* (2018).

[44] G. Knizia, J. Chem. Theory Comput. **9**, 4834 (2013), ISSN 1549-9618.

[45] D. C. Frost, F. G. Herring, A. Katrib, C. A. McDowell, and R. A. N. McLean, J. Phys. Chem. **76**, 1030 (1972).

[46] P. Mollere, H. Bock, G. Becker, and G. Fritz, J. Organomet. Chem. **61**, 127 (1973), ISSN 0009-2975.

[47] R. A. Morgan, A. J. Orr-Ewing, M. N. R. Ashfold, W. J. Buma, N. P. L. Wales, and C. A. de Lange, J. Chem. Soc. Faraday Trans **91**, 3339 (1995), ISSN 0956-5000.

[48] B. Martinez-Haya, I. Zapater, P. Quintana, M. Menéndez, E. Verdasco, J. Santamara, L. Bañares, and F. J. Aoiz, Chem. Phys. Lett. **311**, 159 (1999), ISSN 0009-2614.

[49] P. Quintana, R. F. Delmdahl, D. H. Parker, B. Martinez-Haya, F. J. Aoiz, L. Bañares, and E. Verdasco, Chem. Phys. Lett **325**, 146 (2000), ISSN 0009-2614.

[50] B. Martinez-Haya, P. Quintana, L. Bañares, P. Samartzis, D. J. Smith, and T. N. Kitsopoulos, J. Chem. Phys. **114**, 4450 (2001), ISSN 0021-9606.

[51] J. Barr, I. Torres, E. Verdasco, L. Bañares, F. J. Aoiz, and B. Martínez-Haya, J. Phys. Chem. A **108**, 7936 (2004), ISSN 1089-5639.

[52] J.-H. Yoon, K. C. Woo, and S. K. Kim, Phys. Chem. Chem. Phys. **16**, 8949 (2014), ISSN 1463-9076.

[53] M. B. Williams, P. Campuzano-Jost, D. D. Riemer, C. Tatum, and A. J. Hynes, J. Photochem. Photobiol. **171**, 77 (2005), ISSN 1010-6030.

[54] S. Choi, K.-W. Choi, S. K. Kim, S. Chung, and S. Lee, J. Phys. Chem. A **110**, 13183 (2006), ISSN 1089-5639.

[55] S. Nourbakhsh, K. Norwood, H. Yin, C. Liao, and C. Y. Ng, J. Chem. Phys. **95**, 5014 (1991).

[56] B. Ruscic and J. Berkowitz, J. Chem. Phys. **97**, 1818 (1992), ISSN 0021-9606.

[57] R. T. Bise, H. Choi, H. B. Pedersen, D. H. Mordaunt, and D. M. Neumark, J. Chem. Phys. **110**, 805 (1999), ISSN 0021-9606.

[58] J. Berkowitz, G. B. Ellison, and D. Gutman, J. Phys. Chem. **98**, 2744 (1994), ISSN 0022-3654.

[59] B. Ruscic, J. Phys. Chem. A **119**, 7810 (2015), ISSN 1089-5639.

[60] D. H. Bross, *Active Thermochemical Tables* (2019), URL https://atct.anl.gov.

[61] B. Ruscic and J. Berkowitz, J. Chem. Phys. **98**, 2568 (1993).

[62] M. Aschi and F. Grandinetti, J. Chem. Phys. **111**, 6759 (1999), ISSN 0021-9606.

[63] R. K. Vatsa, C. Majumder, O. D. Jayakumar, S. K. Kulshreshtha, and J. P. Mittal, J. Chem. Sci. **113**, 129 (2001).

[64] R. A. Ingle, C. S. Hansen, E. Elsdon, M. Bain, S. J. King, J. W. L. Lee, M. Brouard, C. Vallance, R. Turchetta, and M. N. R. Ashfold, J. Chem. Phys. **147**, 013914 (2017), ISSN 0021-9606.

[65] A. J. Orr-Ewing and R. N. Zare, Annu. Rev. Phys. Chem **45**, 315 (1994).

Chapter 4

Quantifying Rival Bond Fission Probabilities Following Photoexcitation: C–S Bond Fission in *t*-butylmethylsulfide[1]

4.1 Introduction

A major aspiration in the field of chemical dynamics is to translate the ability to measure and understand the behaviour of excited molecules into a method of controlling the outcome of reactions, be this different product quantum states or molecular products. This ambition has been witness to a variety of clever approaches, from manipulating CIs using Stark fields to change the branching ratio into different product electronic states,[1–4] to pumping of vibrational overtones to enhance motion in particular reaction coordinates.[5] These methods are, so far, limited to smaller molecular systems where resonances are easily defined and associated with specific effects and thus become more approximate and less effective as the molecular complexity increases. Another, and altogether more pressing challenge, is to measure the outcomes of these competitive pathways quantitatively, accurately and, perhaps most importantly, generally.

This complete combination of control and quantification has been achieved once before in a seminal study by F. Fleming Crim's group on the photodissociation of partially deuterated water - HOD.[6–10] Photoexcitation of HOD can result in dissocia-

tion of either the O–H or O–D bonds. For a given molecule this depends on where the vibronic wavefunction collapses as it is projected onto the dissociative excited state.

This molecular system is ideal for exploring competitive bond fission as both radical photodissociation fragments (OD and OH) are amenable to detection via laser induced fluorescence - a technique which is both quantum state specific and, crucially, quantitative. The perfect experiment for photodissociation studies would allow unbiased detection of all photoproducts in a manner which is unaffected by fluctuations in experimental conditions and is generally applicable over a wide range and variety of interesting systems. This has been achieved in molecular systems which decompose into multiple ionic fragments from a prepared molecular di- or tri-cation.[11;12] As all charged fragments produced in one experimental cycle are detectable - after separation by mass in a time of flight mass spectrometer - true coincidences may be drawn from the experiment leading to quantitative information.[13–15] It is also possible to study the dissociation of radical species, which are generated as an anion precursor. The anion can be accelerated using electric fields to translational energies above which the particle can be detected by impact on a position sensitive detector regardless of whether or not the particle is charged. The electron is then photodetached from the anion to form a fast moving radical before quickly being photodissociated and, by virtue of the high translational speed of the anion precursor being carried through, the resulting neutral photofragments and neutral radical parent can be detected by impact upon a time and position sensitive detector. These experiments satisfy the requirement that all photoproducts are detected in an unbiased manner. However, the experiments outlined above are not extendable to other types of molecules, such as the most common case of closed shell neutral species. Coincidence experiments are also difficult to undertake, they require low signal levels, so that individual true coincidences can be picked out accurately, extremely low background signals and, consequently, long acquisition times - all of which leaves them susceptible to experimental drift.

As previously discussed in chapter 3, photofragment translation spectroscopy (PTS) has been widespread in its application to studying individual photodissociation channels. In the early PTS experiments ionisation was achieved using electron bombardment following time of flight (ToF) separation according to kinetic energy of the particle prior to detection by mass spectrometry.[16;17] This allows a time of flight kinetic energy spectrum to be recorded for each photofragment. This was later improved upon by ionisation using a second laser pulse counterpropagating with the pump laser beam

prior to mass spectrometric detection. In contrast to the electron bombardment, in which the energy resolution was ill defined and prone to causing unwanted secondary dissociation, laser based methods allowed for (universal) ionisation using highly energetic photons (single photon ionisation), a high density of less energetic photons (multiphoton ionisation) or a mild intensity of photons which are resonant with an electronic transition in the molecule (resonance enhanced multiphoton ionisation).

The resulting ions can be manipulated by velocity map imaging (VMI) electrostatic optics (as discussed in chapter 2.5) to simultaneously mass separate and map the velocity vectors of the photoproducts which are perpendicular to the axis of mass spectrometer detection.[18;19] The two dimensional detector which maps the products is typically monitored by a high spatial resolution camera which can only respond quickly enough to image one peak in the time of flight spectrum within a single laser shot. As discussed in section 2.5.3, the advent of modern fast framing cameras - such as the Pixel Imaging Mass Spectrometery (PImMS) camera used in these experiments - has unlocked the ability to monitor multiple different photoproducts produced by a single pump laser pulse. Crucially, the MCP/phosphor screen detectors employed in VMI experiments (as discussed in section 2.5.2) can report on the order of hundreds of events per experimental cycle accurately, giving them a distinct advantage over the delay-line detectors previously used in coincidence measurements as the MCP based detectors can accommodate high enough signal levels to complete a measurement before any significant experimental drift occurs.

The triumph of the work contained within this chapter is the determination of the branching ratio for competitive bond dissociation for a closed shell neutral molecule (here t-butylmethylsulfide (BSM)) which - crucially - does not ascribe itself to any "special cases" and so demonstrates a method which is, in principle, generalisable and extendable across a wide range of systems.

BSM can photodissociate by cleaving either of the C–S bonds, as shown in equation 4.1, to form two correlated pairs of photoproducts butyl and methyl sulfide (B + MS 4.1a) or butyl sulfide and methyl (BS + M 4.1b).

$$
\begin{aligned}
\text{BSM} + h\nu \quad &\rightarrow \quad \text{B + MS} & (4.1a) \\
&\rightarrow \quad \text{BS + M} & (4.1b)
\end{aligned}
$$

This study demonstrates how the branching ratios can be extracted through analysis

of the measured yields of M and MS products. There are three components which work together to enable this. Firstly, table 4.1 shows that the three of the four primary photofragments (t-butyl (B), methyl (M) and methanthiyl (MS) radicals) have ionisation potentials which are exceeded by a single $\lambda = 118.2$ nm photon (h$\nu = 10.48$ eV) so that all their recoil velocity distributions can be measured by VMI. A value for the ionisation potential of t-butylthiyl (BS) fragment could not be found, however it is expected to be similar to other thiyl fragments. Secondly, the branching fractions for the competitive bond dissociations can be determined solely through measurement of the M and MS photoproducts. The relative detection efficiencies can be calibrated by detection of M and MS following photolysis of dimethylsulfide (MSM)[20] - an internally symmetric thioether calibrant in which the M and MS photofragments are, necessarily, formed in a 1:1 ratio. Finally, the photofragments formed in each experimental cycle are detected simultaneously using a PImMS2 sensor.[21] This ensures that the entire Newton sphere associated with each photofragment of interest is captured simultaneously, protecting against experimental drift.

Sulfur atom containing organic systems, such as thioethers[22–24] and thioanisoles,[25–29] have been shown to follow complex photochemical pathways and, as such, are popular systems in which to investigate non-adiabatic couplings between different potential energy surfaces (PESs). The UV absorption spectrum of the prototypical thioether, MSM as shown in figure 3.2, shows the long wavelength broad absorption feature beginning at $\lambda < 240$ nm, a strong well-defined absorption band at $\lambda \approx 228$ nm and then semi-structured absorption to shorter wavelengths.[30;31] Drawing inspiration from H_2S, the most simple sulfide, two electronic transitions are ascribed to this absorption range.[32;33] These involve exciting an electron from the highest occupied molecular orbital (HOMO) - an out of plane non-bonding p orbital on the sulfur of b_1 symmetry - to either a Rydberg-like 4s sulfur centred orbital of a_1 symmetry or an antibonding σ^* orbital of b_2 symmetry across the C–S–C or H–S–H framework. These promotions result in excited states of overall $^1B_1$ and $^1A_2$ symmetry, respectively, at the ground state geometry of C_{2V} symmetry, as discussed in section 3.3.1. As one of the bonds elongates *en route* to dissociation, the symmetry is reduced to C_S and both excited states reduce to $^1A''$ symmetry making the previously electric dipole forbidden $B^1A_2 \leftarrow \tilde{X}^1A_1$ transition weakly allowed.

The aim of this chapter, beyond measuring the preferential bond fission ratio, is to rationalise the observed branching fraction by comparison with *ab initio* calculations of cuts of the potential energy surface along the two C–S coordinates.

Species	IP / eV	$\Delta_\mathrm{f}H$ (0 K) / eV
BSM	~8.3-8.5[34]	-1.257 ± 0.008[35]
BS		0.44 ± 0.08[35]
B	6.58 ± 0.01[36]	0.782 ± 0.007[37]
MSM	8.6903 ± 0.0009[38]	-0.22[39]
MS	9.262 ± 0.005[40]	1.346 ± 0.018[41]
M	9.843 ± 0.002[42]	1.552 ± 0.001[37]
S	10.360[43]	2.873 ± 0.003[44]

Dissociation Pathway	Bond Dissociation Energy (0 K) / eV	
	Literature	Calculated
BSM → BS + M	3.25 ± 0.08	3.162
BSM → B + MS	3.39 ± 0.03	3.095
MSM → M + MS	3.12 ± 0.02	3.142

Table 4.1: Values for the ionisation potentials (IP) and enthalpies of formation for MSM and BSM and relevant photofragments explored in this chapter alongside B–SM and BS–M bond dissociation enthalpies derived from these literature values. The dissociation energies calculated with the CBS-QB3 method and zero-point corrected as described in section 4.2 are also presented.

4.2   Experimental

The background on each individual component involved in this experiment is detailed in chapter 2 and will be cross referenced herein appropriately. The focus of this section will be to provide a narrative over the life of a molecule from its genesis in the experiment through to its demise upon detection and to explain the methods of analysis that follow. The samples in this chapter are either pure BSM, pure MSM, or a mixture of BSM and MSM (both Sigma-Aldrich, > 99% purity). The samples were loaded into a sealed test tube with a gas line valve and, in the case of the mixed samples, the ratio of liquids was calculated in accordance with Raoult's law[45] (equation 4.2) to produce a 2:1, 1:1, or 1:2 mixture in the vapour phase. The pure sample or mixture was further purified by removal of trapped gas by freeze-pump-thaw cycles until no bubbles were liberated upon thawing.

Raoult's law is defined as

$$P = p_A x_A + p_B x_B \tag{4.2}$$

where P is the total pressure, p_n is the partial pressure of component n and x_n is the mole fraction of n and the total pressure is a sum over the product of the partial
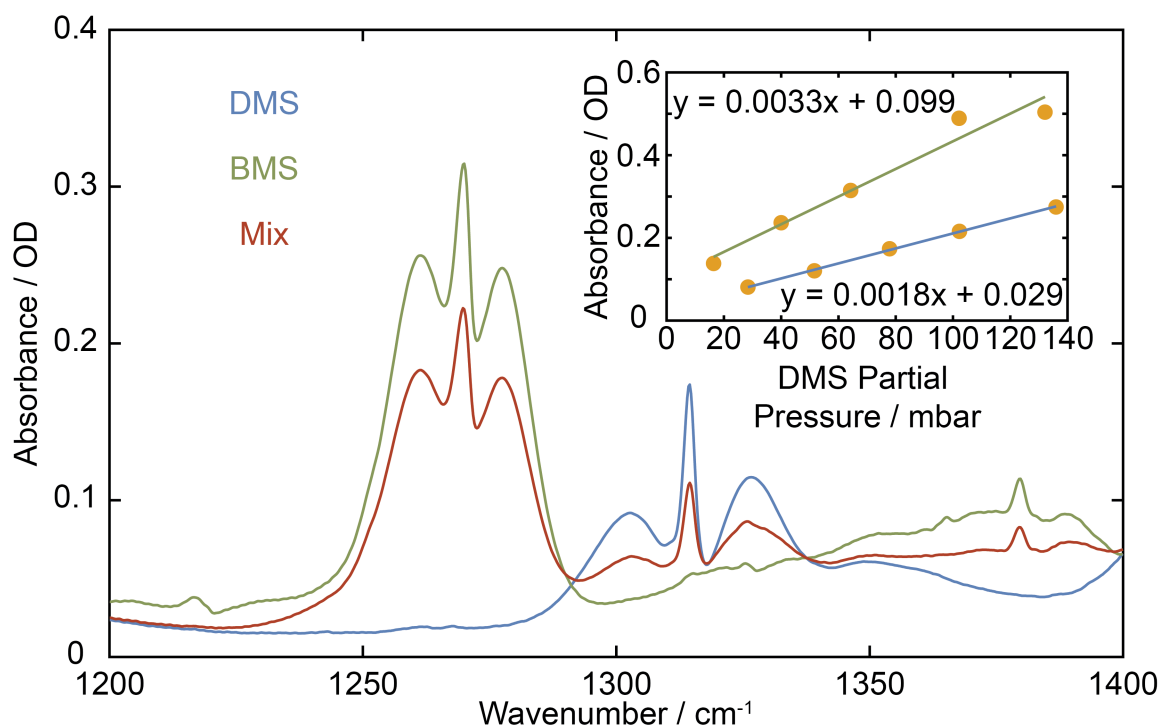
Figure 4.1: FT-IR spectra of pure MSM (blue), BMS (green) and an unknown mix of MSM and BMS (red) at pressures of 77.9, 64.3 and 79.4 mbar respectively. The inset panel shows calibration curves for MSM (blue) and BMS (green).

pressure and mole fraction of each component in the mixture.

The ratio was tested by recording Fourier Transform Infrared (FT-IR) spectra for vapours of pure MSM and BSM to identify unique IR signatures in each. The spectra were recorded at various pressures and calibration curves for absorbance of the unique features vs pressures of the pure samples was created. FT-IR spectra of the vapour drawn off the mixed sample were then recorded and the vapour phase ratios validated by comparison against the calibration curve. Representative vapour phase IR spectra of MSM and BMS are shown in figure 4.1 along an example mixed sample. Inset are the calibration curves for MSM and BMS in blue and green, respectively. The mixed spectrum shown in red was prepared as a test by a lab colleague. The absorbances in the mixed sample correspond to partial pressures of 45 mbar MSM and 36 mbar BMS corresponding to a 55:45 ratio. The vapour phase was drawn off in an aliquot sufficient to fill an evacuated glass bulb to 80 mbar and topped off with pure He to 800 mbar (10% concentration of sample). The bulb was then loaded behind a pulsed valve (Parker Hannifin General Valve Series 9) with a conical nozzle face plate. The sample was then supersonically expanded into a vacuum chamber held at $\sim 1 \times 10^{-7}$ mbar to form a molecular beam (section 2.3). The resultant beam was intersected by

a conical skimmer with a 1 mm orifice which selected the central coldest section of the beam to pass into a differentially pumped interaction chamber. The molecules then pass into the velocity mapping region of a set of ion optics (section 2.5) via a 3 cm orifice in the back of a repeller plate. The ion optics are oriented so that the time of flight axis is coincident with the axis of the molecular beam propagation, henceforth designated as the z axis.

The molecules are intersected by a photodissociation laser beam propagating perpendicular to the molecular beam. The photodissociation light is the linearly polarised frequency doubled output of a Sirah Cobra-Stretch dye laser loaded with Coumarin 450 dye (Exciton) and pumped by the third harmonic (355 nm) of a Nd:YAG laser. The photodissociation beam is focussed into the interaction region using a fused silica lens (focal length = 25 cm). After a 30 ns delay, the molecular beam is then intersected with an ionisation laser consisting of linearly polarised 118.2 nm (10.5 eV) photons. These were produced by focussing the third harmonic (355 nm) of a Nd:YAG laser into a tripling cell containing a phase matched mixture (1:11.5) of xenon and argon at a total pressureof 400 mbar. This acts to triple the frequency of the incident laser photons and the resultant divergent 118.2 nm beam was refocused to just short of the interaction region using a custom made Lithium Fluoride (LiF) lens (focal length = 30 cm). Ionisation using 118.2 nm (10.5 eV) photons which exceed the ionisation potentials of all relevant fragments, as shown in table 4.1. The nascent ions are then accelerated by the VMI optics, which separate them spatially according to velocity and separate them along the molecular beam axis (z) according to mass. Following this the ions enter a field free region in which, as they drift towards the detector, their mass separation in time of flight space and transverse propagation in the detector plane are exaggerated.

The ions then impact upon a position sensitive detector (section 2.5.2) consisting of a triple stack of Microchannel Plates (MCPs) coupled to a P47 phosphor screen. The bias across the three plates was held at 2300 V, too low to amplify signal, and then pulsed up to 2800 V using a Photek GM-MCP gating module. The scintillations on the phosphor screen resulting from ions impinging on the detector are recorded by a PImMS2 camera[21;46;47] set to a time resolution of 25 ns. For the given ion optics voltages, this equates to 8-10 time slices through any of the Newton spheres of interest.

The data were processed according to the centroiding algorithm[48] detailed in section 2.6.1 to reduce clusters of events in time and space to single ion events. Mass spectra were generated by binning all events according to arrival time (in time bins),

converting to m/z space by calibrating against the time of flight of known mass peaks and compensating the intensities according to an appropriate Jacobian transformation (as shown in appendix B.1). Ion images were created by plotting the (x, y) coordinates of events within a given mass peak into a two-dimensional array, any disproportionately intense pixels (caused by dark counts on the camera) were discarded and set to the average value of the neighbouring eight pixels. The resulting crushed ion image was reconstructed (section 2.6.4) using the Polar Onion Peeling algorithm[49] to recover the infinitesimal central slice. The image was transposed into a two dimensional array of polar coordinates. The radial distribution was extracted by integrating across all angles and then the angular distribution of features in the radial distribution was characterised by fitting to a second order Legendre polynomial (section 2.6.4). The corresponding velocities for a radius at a given mass was calibrated by monitoring the O^+ signals from the thoroughly characterised photodissociation of O_2 and REMPI of the $O(^3P)$ atom fragments at $\lambda = 225.67$ nm.[50]

The geometry of the BSM molecule was optimised on the ground state using Møller-Plesset second-order perturbation theory (MP2)[51] in the correlation consistent double zeta basis set (cc-pVDZ) by Dunning and coworkers.[52] Cuts along the C–S elongation coordinates of the potential energy surfaces were computed by fixing the C–S bond lengths, optimising all other geometries at the MP2 level and calculating the first two excited states of A'' symmetry using complete active space second-order perturbation theory (CASPT2)[53;54] using the augmented correlation consistent double zeta basis set (aug-cc-pVDZ)[52] using a reference wave function from a state-averaged complete active space self consistent field (SA-CASSCF) calculation. The active space for these calculations consisted of 6 electrons dispersed over five orbitals, the three highest valence orbitals (two σ orbitals and an out of plane p orbital) and the two lowest unoccupied orbitals (corresponding to the σ^* orbitals along the two C–S bonds) as shown in figure 4.2. A level shift of 0.5 hartrees was applied to the individual states treated with the CASPT2 calculation to improve convergence and protect against unwanted intruder states. The thermochemical calculations for the BS–M and B–SM bond enthalpies were computed using the complete basis set extrapolation methods (CBS-QB3)[55;56]. The MP2, CASSCF and CASPT2 computations were performed in Molpro 2018[57], whilst the CBS calculations were performed in Gaussian 16.[58]
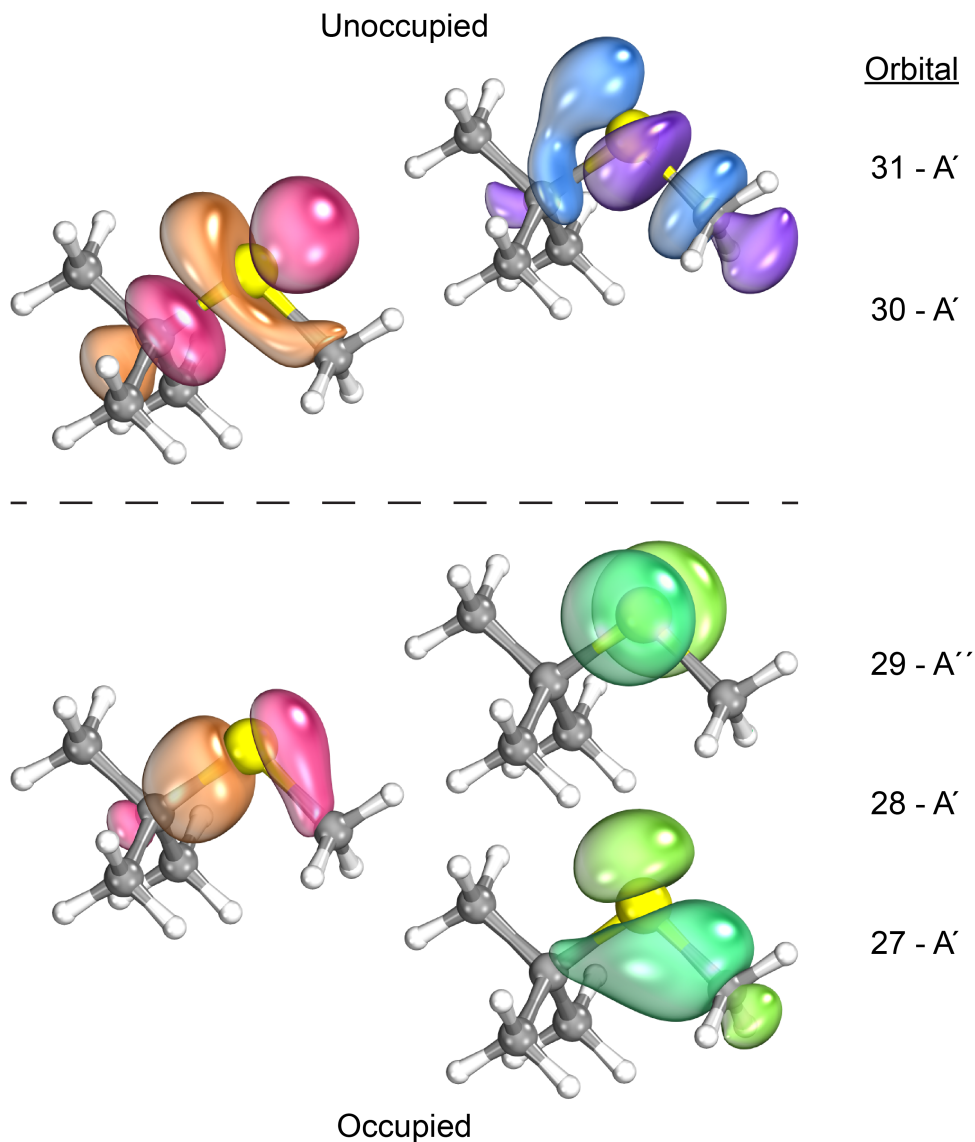
Figure 4.2: The three highest occupied molecular orbitals and two lowest unoccupied molecular orbitals of BMS. The orbitals were calculated at the complete active space self consistent field level with an aug-cc-pVDZ basis set based on a ground state geometry optimised at the MP2 level.

4.3   Results & Discussion

4.3.1   The photochemistry of *t*-butylmethylsulfide

Figure 4.3 shows the room temperature UV absorption spectrum of BSM vapour diluted in *n*-hexane to avoid saturation of the spectrum. It is similar in appearance to the MSM spectrum shown in the previous chapter, though less structured. The
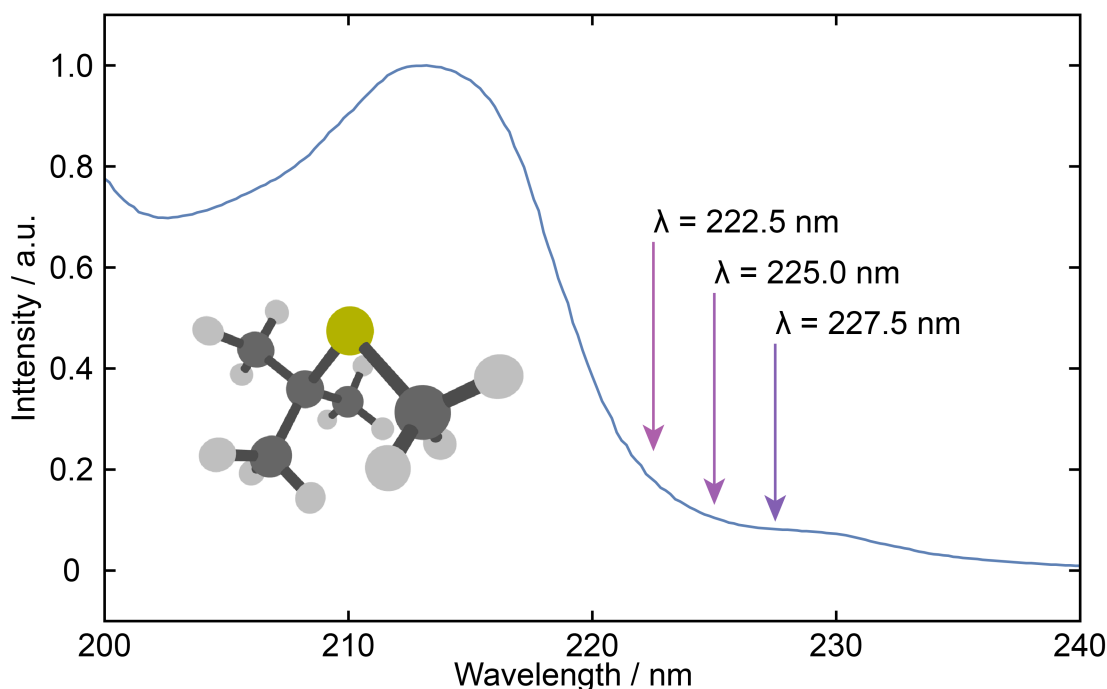
Figure 4.3: UV absorption spectrum of the vapour from a room temperature solution of BSM diluted in n-hexane recorded against a background of pure n-hexane vapour. The three coloured arrows at 227.5, 225.0 and 222.5 nm indicate the photolysis wavelengths used in this study.

absorption is concentrated at wavelengths less than 240 nm. The absorption onset begins with a plateau from $\sim$ 240 - 220 nm which is assigned to a combination of the $1^1A'' \leftarrow \tilde{X}$ and $2^1A'' \leftarrow \tilde{X}$ transitions.

The photoexcitation wavelengths in this work were chosen to be 227.5, 225.0, and 222.5 nm as indicated by the vertical arrows in figure 4.3 to represent the evolution across the two lowest A'' excited states. Figure 4.4 shows a mass spectrum of BSM following photodissociation at 225.0 nm and subsequent universal ionisation of all fragments using 118.2 nm photons in blue along with the mass spectra obtained under the presence of just the photolysis (green trace) or ionisation (red trace) lasers. The parent ion peak, located at m/z 104, is conspicuously absent from these traces. It is by far the dominant peak in the ion yield spectrum, however the sensitivity of the detector was only high for the time of flight window which included the photofragments in order to minimise damage to the detector from the strong parent signal. Strong two colour enhancement signals are apparent for peaks assigned to M^+ (m/z 15), MS^+ (m/z 47), B^+ (m/z 57) and BS^+ (m/z 89), which are all easily rationalised as
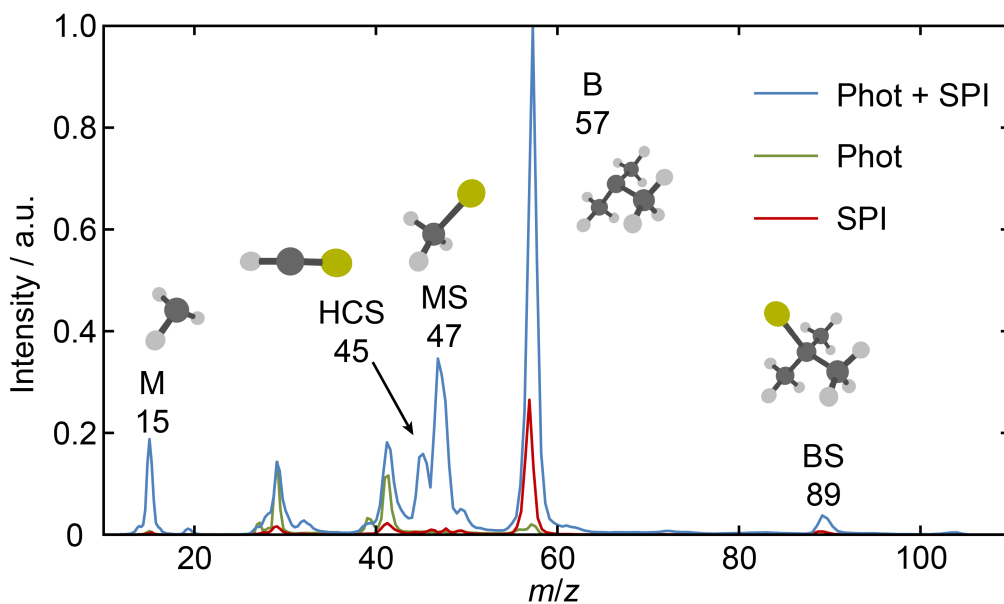
Figure 4.4: Mass spectra obtained from calibration of TOF spectra measured following photodissociation of jet cooled BSM at $\lambda = 225.0$ nm followed by single photon universal ionisation at $\lambda = 118.2$ nm. The blue trace represents the two colour spectrum obtained with both laser pulses while the green and red traces demonstrate those obtained with only the photodissociation or ionisation pulses, respectively. The parent ion at m/z 104 is suppressed by pulsing the detector sensitivity to high only for the time of flight period associated with the photofragments between m/z 10 to 60.

the products of dissociation along the rival C–S bond coordinates. As has previously been observed in MSM, there is a significant two colour component in the formation of HCS^+ (m/z 45) following unimolecular ejection of H_2 from MS^+ in the same manner discussed extensively in section 3.3.2. The peaks at m/z 29 and 41 are assigned to C_2H_5 and C_3H_5, respectively. These peaks are overlapped entirely by the photolysis laser induced spectrum indicating that their formation is dominated by the photolysis laser. As the ion distributions show no fast component, they are unlikely to have been formed following photodissociation. Therefore the proposed mechanism is that the BSM parent undergoes two photon non-resonant ionisation to form BSM^+ following which it dissociates on the cation surface to form $MS + B^+$. The nascent B^+ then absorbs another UV photon and has enough energy to further fragment. The ion images associated with the m/z 15 (M^+), 47 (MS^+), 57 (B^+) and 89 (BS^+) as shown in panels a), d), c) and b) of Figure 4.5, arranged so that the rows represent pairs of

Threshold energies (0 K)		/ eV
BSM	$\rightarrow$ MS + $\mathbf{B^+}$	9.965
	$\rightarrow$ ES + $C_3H_7^+$	10.88
	$\rightarrow$ PS + $\mathbf{C_2H_5^+}$	11.52
	$\rightarrow$ MS + $\mathbf{C_3H_5^+}$ + CH_4	11.905
	$\rightarrow$ ES + $\mathbf{C_3H_5^+}$ + H_2	12.33
	$\rightarrow$ MS + $\mathbf{C_2H_5^+}$ + C_2H_4	12.72
BSM^+	$\rightarrow$ MS + $\mathbf{B^+}$	~ 1.55
	$\rightarrow$ ES + $C_3H_7^+$	~ 2.47
	$\rightarrow$ MS + $\mathbf{C_3H_5^+}$ + CH_4	~ 3.50
	$\rightarrow$ ES + $\mathbf{C_3H_5^+}$ + H_2	~ 3.95
	$\rightarrow$ MS + $\mathbf{C_2H_5^+}$ + C_2H_4	~ 4.25
	$\rightarrow$ PS + $\mathbf{C_2H_5^+}$	~ 4.40

Table 4.2: Thermochemical threshold energies for dissociative ionisation of BSM and for the photodissociation of BSM^+ cations. Fragment species detected in the photolysis laser only ion TOF-MS are highlighted in bold. For reference the energies of one and two $\lambda = 225.0$ nm photons are, respectively 5.51 and 11.02 eV. MS, ES and PS are a shorthand for CH_3S, CH_3CH_2S and $CH_3CH_2CH_2S$, respectively.

photofragments. The left hand portion of the images represent the raw ion image of the crushed Newton sphere and the right hand side displays the infinitesimal central slice following reconstruction using the Polar Onion Peeling algorithm.[49] The B^+ image contains an intense central feature which is attributed primarily to the dissociative ionisation of the BSM parent. As table 4.1 shows, the ionisation potential of BSM is $\sim$8.3 - 8.5 eV, and can be overcome by either two pump photons (11.4 eV) or one probe photon (10.48 eV). This feature could also arise from UV photodissociation of the BSM^+ following two photon ionisation with the pump laser. The former situation, where three pump photons non resonantly ionise before photodissociating the parent ion is also attributed to the pump laser only signals in the mass spectrum at m/z 41, and 29. These are assigned as C_3H_5 and C_2H_5 respectively. Possible decomposition pathways for both dissociative ionisation of BSM and photodissociation of BSM^+ are shown in table 4.2. It should be noted that the inner 'ring' in the BS^+ image is an artefact. The intense signal levels in the centre of the B^+ image saturate the MCPs and they cannot recover in the ~ 1.25 μs between the two mass peaks arriving.[59] The signal levels can be reduced in order to avoid the saturation but these conditions are required to clearly measure the anisotropy component of the weak two colour component in the B^+ image.

Integrating the radial distribution originating from the centre of each image around
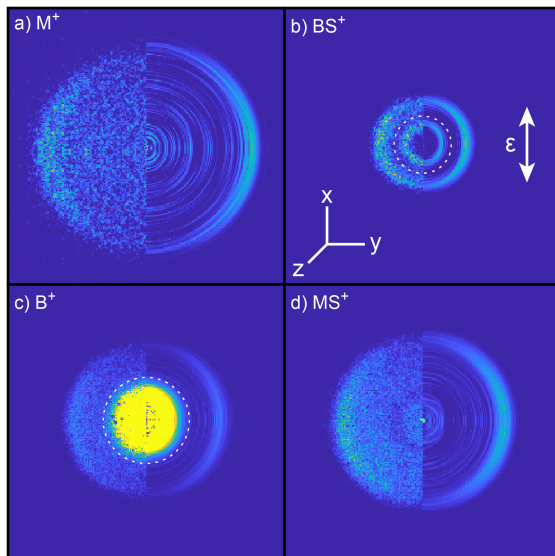
Figure 4.5: The left halves represent the crushed images of the m/z (a) 15 (M^+), (b) 89 (BS^+), (c) 57 (B^+) and (d) 47 (MS^+) ion time of flight peaks following λ = 225.0 nm photolysis of BSM and subsequent SPI at λ = 118.2 nm, with the ϵ vector of both pump and probe lasers aligned vertically in the plane of the images as indicated. The right hand half of the images show central slices through the corresponding symmetrised 3-D velocity distributions following reconstruction using Polar Onion Peeling. Signals inside the dashed rings in panels b) and c) are omitted from any analysis of the radial distribution of these images.

all angles returns the speed distributions which are readily converted to a momentum distribution, by multiplication by the mass, and to total kinetic energy release (TKER) distributions by multiplication by $\frac{1}{2}mv$ to yield kinetic energy and subsequent transformation to TKER as described in section 2.6.6. Figure 4.7 shows the momentum distributions of the two pairs of photofragments following C–S bond fission (*i.e.* M with BS and B with MS). The distributions broadly match well, with the peaks of the distributions sitting at the same momentum, implying that the efficiency of single photon ionisation for each species is not markedly quantum state dependent. The BS distribution is significantly broader than its partner M distribution which is assigned to a similar Coulombic blurring in the interaction region as discussed in section 3.3.4. Interestingly, the same disparity does not seem to affect the B and MS pair, which is understandable as, at the point of ionisation, both the B and MS Newton spheres are nested within the M and BS Newton spheres. Therefore they have interactions coming from either side which balance each other and so the distributions are blurred
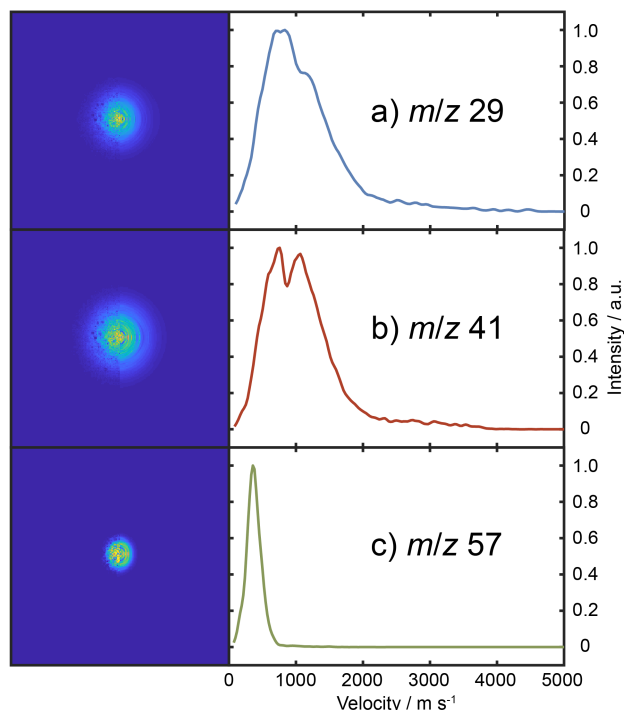
Figure 4.6: The left hand panels contain the ion images corresponding to the m/z 29 C_2H_5, m/z 41 C_3H_5, and C_4H_9 collected in the presence of only the pump UV laser beam. The right hand panel shows the corresponding velocity distributions.

by a similar amount. This is in contrast to the lightest Newton sphere (M) which is only subject to Coulombic forces pushing it outwards at the point of ionisation.

Figure 4.8 panels a) and b) show the TKER distributions - E_T - derived from the M, MS, B and BS photofragment distributions assuming momentum matching with the respective BS, B, MS and M photofragments. Indicated on the distributions by downward arrows are the maximum E_T values allowed given a photolysis energy of 5.57 eV (corresponding to a $\lambda = 225.0$ nm photon) and C–S bond enthalpies from the literature and from *ab initio* calculations (as shown in table 4.1) in dashed and bold lines respectively and assuming no partitioning of the energy into internal degrees of freedom. The E_T distributions peak close to the E_T maxima implying that the majority of the energy disposal is into translation and any internal excitation is most likely in the form of rovibrational excitation of the alkylthiyl photofragment. The angular distributions for the two pairs of photofragments, M paired with BS and MS paired with B, are shown in figure 4.8 panels c) and d) respectively along with the β values corresponding to the best fits of the angular distributions to equation 1.29. The angular distributions are represented as intensity *vs* θ where θ is the angle between the electric vector of photoexcitation light and the measured velocity vector of the

Figure 4.7: Normalised momentum distributions of the a) M and BS and b) B and MS fragments derived from images recorded following $\lambda = 225.0$ nm photodissociation of BSM and subsequent SPI at $\lambda = 118.2$ nm.

fragment. The angular distributions of the alkyl thiyl fragments are measured as less anisotropic than their alkyl fragment counter parts. This is explained by the fragments being formed aligned in a plane and the ionisation of the akyl thiyl fragments being sensitive to the electric vector of the VUV photons. This explanation is discussed in further detail in section 3.3.5.

4.3.2 Quantifying the branching ratios

We turn now to the competitive bond dissociation, the primary focus of this chapter. In order to measure the preference for fission of one C–S bond over another following photoexcitation, the proposed experiment is to load a molecular beam with both the asymmetric thioether to be characterised and a corresponding symmetric thioether in which the C–S bond fission forms a pair of photofragments common to the asymmetric thioether and recording the ion images of all photofragments simultaneously by using single photon ionisation and multimass imaging.

To deconvolute the contributions to each of these ion distributions from the mix, ion images were recorded for the photolysis of pure MSM and BSM monitoring the M, MS, and HCS fragments. HCS is included as a secondary photoproduct from MS and so must be counted in the overall yield of MS. The radial distributions of the M^+, MS^+ and HCS^+ ion images were fitted to Gaussian functions (or a sum of two Gaussian distributions in the case of HCS). The width and centres of the Gaussians, as well as the relative intensities of the two Gaussians used to fit the HCS distribution, were noted down for use in the basis functions while the absolute intensities, as the float
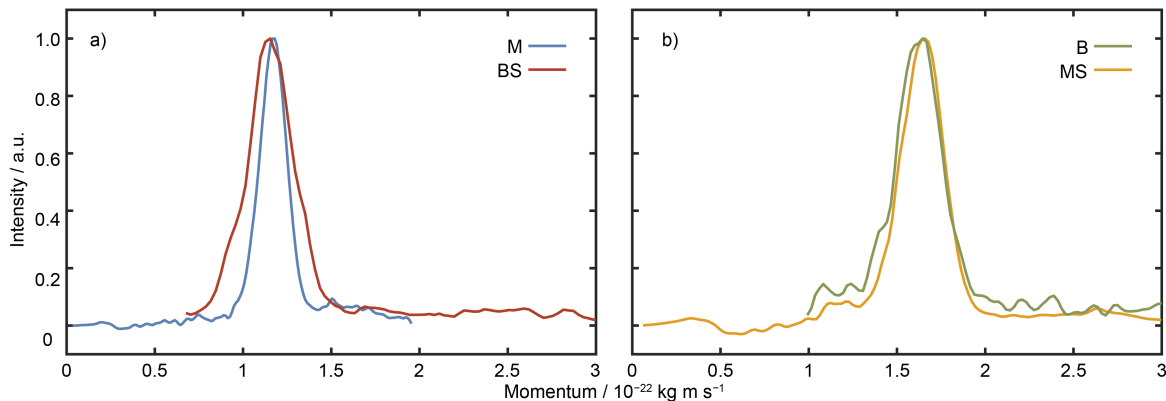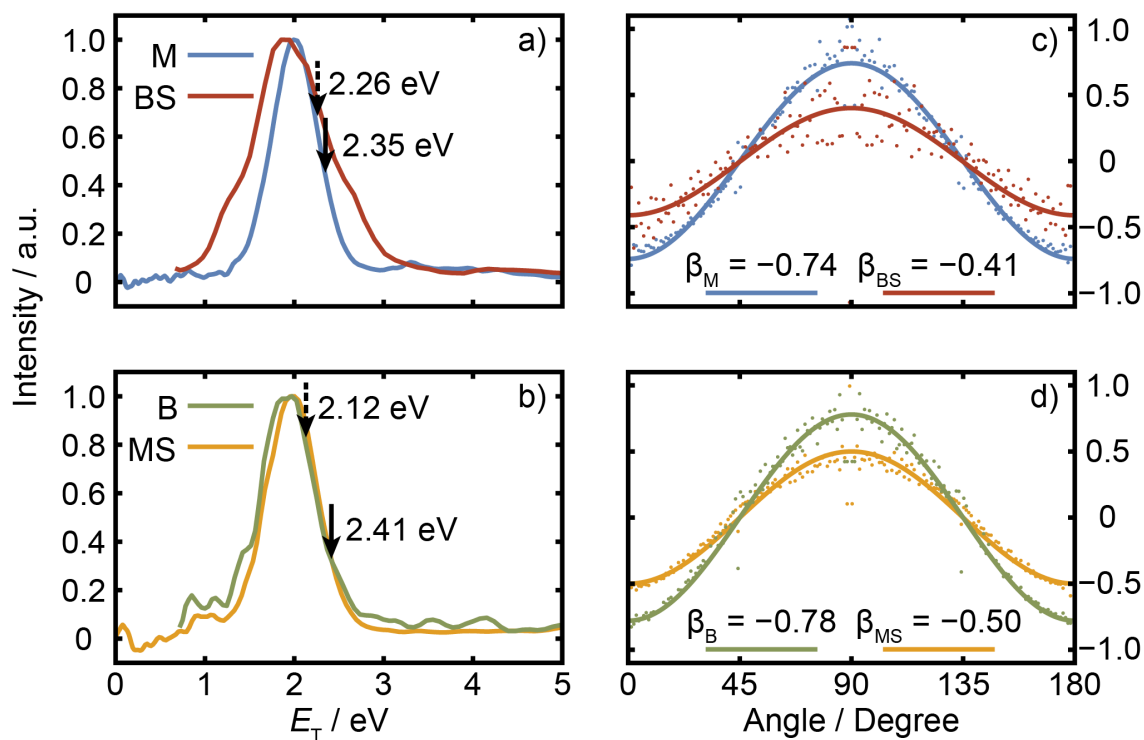
Figure 4.8: Normalised E_T distributions of the a) M and BS and b) B and MS fragment derived from the respective images recorded following $\lambda = 225.0$ nm photodissociation of BSM and subsequent SPI at $\lambda = 118.2$ nm. The solid and dashed arrows indicate the $E_{T(max)}$ values derives using, respectively, the *ab initio* bond strengths calculated in this work and the prior thermochemical data listed in table 4.1. Intensity *vs. θ* plots for the c) M and BS and d) B and MS products plotted on a common vertical scale that spans the full range required for a distribution characterised by an anisotropy parameter $\beta = -1$, with the best fit β values inset in the panel.

parameter for fitting the mixes, were disregarded. These functions and parameters formed basis sets for deconvoluting a mixed sample and basis sets were constructed for both MSM and BSM at each of the three different pump wavelengths used in this experiment, $\lambda = 227.5$, 225.0 and 222.5 nm. These parameters are given in tables 4.3 and 4.4 where μ corresponds to the centre of the Gaussian in pixels, σ to the width of the Gaussian in pixels, and A is the normalised intensity of the Gaussian. This process returns six functions one for each of the M, MS and HCS features arising from both MSM and BSM. The amplitudes of these six functions were allowed to float to fit the radial distributions derived from the ion images arising from a mixed sample. The resulting fitted functions are then integrated to return six intensity values for the
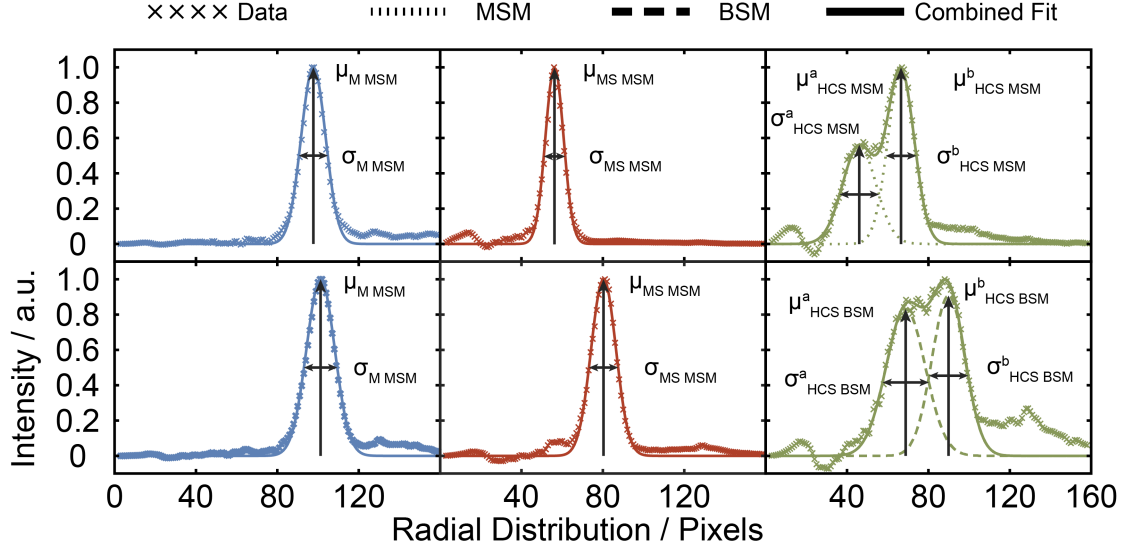
Figure 4.9: Radial distributions integrated over all angles for the central slices of the 3D velocity distributions of Methyl (m/z 15$^+$), Methyl Sulfide (m/z 47$^+$) and HCS (m/z 45$^+$) following photodissociation at $\lambda = 225.0$ nm and subsequent single photon ionisation at $\lambda = 118.2$ nm. The top row corresponds to fragments formed from the photodissociation of dimethyl sulfide and the bottom row corresponds to fragments formed from the photodissociation of t-butylmethylsulfide. All distributions are fitted to Gaussian distributions (or in the case of HCS - a sum of two Gaussian distributions) with their width and centre parameters indicated in the corresponding panels. The values for these parameters are shown in tables 4.3 and 4.4.

three photofragments from both samples as follows: I(M_{MSM}), I(M_{BSM}), I(MS_{MSM}), I(MS_{BSM}), I(HCS_{MSM}), and I(HCS_{BSM}).

The intensity of a given feature in an ion image can be defined by the following equation:

$$I_{frag,parent} = \sigma_{parent} P_{parent} \delta_{frag,parent} \phi_{frag,parent} \qquad (4.3)$$

where σ is the absorption cross section of the parent at the excitation photon energy, P is the partial pressure of the parent in the interaction region, δ is the detection efficiency of a given molecular species, and ϕ is the quantum yield of a fragment from the photodissociation process. For now we will ignore the HCS contribution to simplify the mathematics and then reintroduce it later.

The question now becomes, do we have all of the information in a simultaneous measurement of all the photofragments arising from the photodissociation of pure BSM to retrieve the branching ratio? To do so, the equations that give the intensity

		MSM					
	λ / nm	227.5		225.0		222.5	
M$^+$	μ / pixels	97.3		97.7		97.9	
	σ / pixels	5.3		6.0		5.9	
MS$^+$	μ / pixels	55.9		56.2		56.2	
	σ / pixels	3.6		4.5		4.2	
HCS$^+$	μ^{a}, μ^{b} / pixels	45.2	65.6	46.0	55.6	47.0	67.4
	σ^{a}, σ^{b} / pixels	7.7	6.5	8.3	6.5	10.2	6.5
	A$^{\text{a}}$, A$^{\text{b}}$	0.56	1	0.57	1	0.72	1

Table 4.3: Best fit parameters for the Gaussian functions used to describe the M$^+$, MS$^+$ and HCS$^+$ velocity distributions following photolysis of MSM at $\lambda = 227.5$, 225.0 and 222.5 nm with, in each case, subsequent SPI at $\lambda = 118.2$ nm.

of M and MS arising from photodissociation of BSM must be combined and rearranged to derive an expression for the ratio of the quantum yields of M and MS as shown in equations 4.4 and 4.5.

$$\frac{I_{M,BSM}}{I_{MS,BSM}} = \frac{\sigma_{BSM}}{\sigma_{BSM}} \frac{P_{BSM}}{P_{BSM}} \frac{\delta_M}{\delta_{MS}} \frac{\phi_{M,BSM}}{\phi_{MS,BSM}} \tag{4.4}$$

$$\frac{\phi_{M,BSM}}{\phi_{MS,BSM}} = \frac{I_{M,BSM}}{I_{MS,BSM}} \frac{\sigma_{BSM}}{\sigma_{BSM}} \frac{P_{BSM}}{P_{BSM}} \frac{\delta_{MS}}{\delta_M} \tag{4.5}$$

$$\frac{\phi_{M,BSM}}{\phi_{MS,BSM}} = \frac{I_{M,BSM}}{I_{MS,BSM}} \frac{\sigma_{BSM}}{\sigma_{BSM}}^{\nearrow 1} \frac{P_{BSM}}{P_{BSM}}^{\nearrow 1} \frac{\delta_{MS}}{\delta_M} \tag{4.6}$$

Since the terms that depend only on the parent cancel out, as shown in equation 4.6, the expression for the ratio of quantum yields can be reduced to an expression which depends exclusively on the ratio of the measured intensities and the relative detection efficiencies of the fragments as shown in equation 4.7.

$$\frac{\phi_{M,BSM}}{\phi_{MS,BSM}} = \frac{I_{M,BSM}\delta_{MS}}{I_{MS,BSM}\delta_M} \tag{4.7}$$

This demonstrates that there is still a question mark hovering over the relative detection efficiencies of the M and MS photofragments. The detector efficiency is a rather murky parameter which includes a variety of components that are not easily disentangled, these components include the absorption cross section/ionisation efficiency of the species and the sensitivity of the detector to the molecular species.

To characterise the detection sensitivities we must turn to the case of symmetric thioethers, here MSM. Crucially, in the case of symmetric thioethers, the ratio of

		BSM					
	λ / nm	227.5		225.0		222.5	
M$^+$	μ / pixels	101.2		101.3		101.3	
	σ / pixels	6.4		6.9		8.1	
MS$^+$	μ / pixels	80.9		80.3		79.3	
	σ / pixels	6.0		6.1		6.4	
HCS$^+$	μ^{a}, μ^{b} / pixels	68.7	90.2	68.8	89.9	67.8	89.3
	σ^{a}, σ^{b} / pixels	10.6	8.5	9.7	8.1	9.8	8.3
	A$^{\text{a}}$, A$^{\text{b}}$	0.95	1	0.92	1	0.94	1

Table 4.4: Best fit parameters for the Gaussian functions used to describe the M$^+$, MS$^+$ and HCS$^+$ velocity distributions following photolysis of BSM at λ = 227.5, 225.0 and 222.5 nm with, in each case, subsequent SPI at λ = 118.2 nm.

the quantum yields of M and MS must absolutely be 1 as any photodissociation event which produces an M fragment must also produce an MS. Thus, as is shown in equations 4.8a and 4.8b, the ratio of intensities becomes a direct measure of the detection efficiencies.

$$\frac{\delta_{MS}}{\delta_M} = \frac{I_{MS,MSM}}{I_{M,MSM}} \frac{\phi_{M,MSM}}{\phi_{MS,MSM}}^{\,1} \tag{4.8a}$$

$$\frac{\delta_{MS}}{\delta_M} = \frac{I_{MS,MSM}}{I_{M,MSM}} \tag{4.8b}$$

This expression can then be substituted directly back into equation 4.7 to yield equation 4.9.

$$\frac{\phi_{M,BSM}}{\phi_{MS,BSM}} = \frac{I_{M,BSM}}{I_{MS,BSM}} \frac{I_{MS,MSM}}{I_{M,MSM}} \tag{4.9}$$

Here, we can reintroduce the intensity of the HCS components by simply adding them to the intensity of the MS signals as they are produced exclusively following formation of MS. This is shown in equation 4.10.

$$\frac{\phi_{M,BSM}}{\phi_{MS,BSM}} = \frac{I_{M,BSM}}{(I_{MS,BSM} + I_{HCS,BSM})} \frac{(I_{MS,MSM} + I_{HCS,MSM})}{I_{M,MSM}} \tag{4.10}$$

The observed ratio will be the *absolute* branching fraction in the limit that $\phi_{MS,\,BSM}$ + $\phi_{M,\,BSM}$ = 1, which it is reasonable to assume is the case here given the implied fast dissociation demonstrated by the near limiting β values that characterise the fragment recoil anisotropies. There is an implicit assumption that the ability of the experiment to detect M generated by photodissociation of MSM is equal to its ability to detect M originating from photodissociation of BSM and for the corresponding pair of MS fragments, the validity of which deserves some unpacking. The ionisation efficiency of

the populated quantum states of M and of MS are assumed to be uniform. Regardless of the distribution of internal state the M or MS fragments are created in, the quality of the momentum matching shown in figure 4.7 supports the assumption that the M is being sampled equally as effectively as its paired BS co-fragment and this can be extended to the MS and B pair.

This high quality momentum matching has been previously demonstrated for M and MS following photodissociation of MSM as shown in the previous chapter (figure 3.6), and the similar photodissociation processes that occur in MSM and BSM must produce both the M from MSM and M from BSM in similar distributions of internal states with the same argument applying to the MS fragment. This needs to be taken into account when considering pairs of target and calibrant molecules in any experiment of this ilk. The efficiency of the detector to the different M and MS fragments is dependent on the component of their momentum perpendicular to the plane of the detector, as this is determined exclusively by the acceleration of the M^+ and MS^+ ions along the time of flight axis, it is valid to assume this will be almost entirely independent of the origin of the fragments.

Figure 4.10 panels a), c), and e) show the ion images of M, MS and HCS, respectively, following photodissociation of a 50:50 mixture of BMS and MSM at $\lambda = 225.0$ nm followed by ionisation at $\lambda = 118.2$ nm. As per the previous section, these fragments are formed following photoexcitation of the BMS and MSM either directly (M and MS) or via subsequent dissociative ionisation of a direct photoproduct (HCS). BS and B are also formed following photoexcitation of BMS but, as was shown earlier when MSM is the internal calibrant, these can be disregarded for the analysis of competitive bond dissociation. In principle, the B and BS images alone could be used for the experiment if BSB was used as an internal calibrant instead. As in figure 4.5 the left half of each image shows the raw, crushed, ion image while the right half of the image shows the central slice though the 3-D velocity distribution following reconstruction with the Polar Onion Peeling algorithm.[49] Panels b), d) and f) show the radial distribution of each reconstructed image in velocity space integrated across all angles. Each distribution is composed of four traces. The crosses represent the data, the contribution to the overall fit from the pertinent MSM basis function is shown in a dotted line, the contribution to the overall fit from the pertinent BSM basis function is shown by a dashed line and the overall fit to the distribution is shown as a solid line. The distributions are all normalised to the same maximum in the most intense distribution, MS.
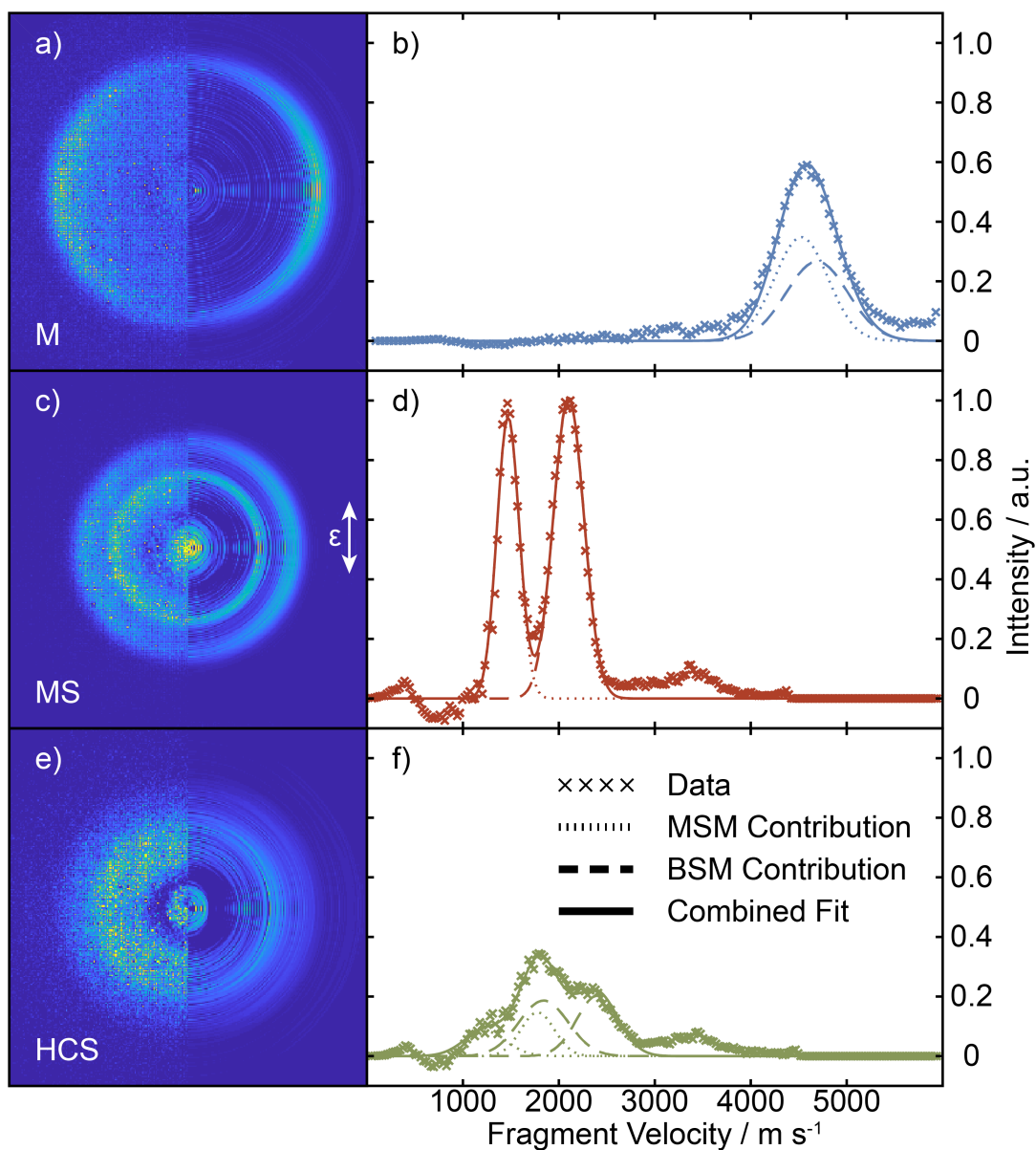
Figure 4.10: Velocity distributions derived by radial integration over all angles over the m/z a) 15 (M$^+$), b) 47 (MS$^+$) and c) 45 (HCS$^+$) ion signals following $\lambda = 225.0$ nm photolysis of a mixture containing equal partial pressures of BSM and MSM and subsequent SPI at $\lambda = 118.2$ nm, with the ϵ vector of both lasers aligned vertically in the plane of the images, along with the best-fit Gaussian functions used in determining the reported branching ratios. The left and right halves of the inset in each panel show the crushed and reconstructed central slice (after symmetrisation) images.

	Photolysis λ / nm		
	227.5 nm	225.0 nm	222.5 nm
N	21	22	21
$\frac{\phi_{MS,BSM}}{\phi_{M,BSM}}$	1.80 ± 0.33	2.14 ± 0.64	2.7 ± 1.3
$\phi_{MS,\,BSM}$ / %	64^{+4}_{-5}	68^{+5}_{-8}	73^{+7}_{-14}
$\phi_{M,\,BSM}$ / %	36^{+5}_{-4}	32^{+8}_{-5}	27^{+14}_{-7}

Table 4.5: Quantum yields for the B–SM and BS–M bond fission following UV excitation of BSM. The quoted uncertainties are 2σ values from fitting all N data sets recorded (for a range of different BSM/MSM mixing ratios) at the given wavelength.

The ion images of the M, MS, and HCS photofragments following photodissociation of a mixed sample were recorded at three different wavelengths and the results are summarised in table 4.5 and show that dissociation along the B–S bond is approximately twice as likely as cleavage of the M–S bond. These values were arrived at over more than twenty data sets (indicated by the values in the row designated N) which were dispersed over a range of ratios of the partial pressures of BSM and MSM against which the value was found to be entirely invariant. Although tempting to assign some meaning to the observed wavelength dependence of the values, the increasingly large uncertainties as the pump photon energy increases, preclude any significant comment about the effect of the pump photon energy on the branching ratio.

4.3.3   Rationalisation In Terms Of Potential Energy Surfaces

Figure 4.11 shows cuts through the relaxed potential energy surface of BSM along the two C–S elongation coordinates - $R_{\mathrm{B–SM}}$ and $R_{\mathrm{BS–M}}$ - calculated at the CASPT2 level. These calculations were performed by scanning along the relevant R coordinate in intervals of 0.1 Å at short R values and 0.2 Å at long R values, before relaxing the rest of the nuclear geometry by minimising the ground state energy and calculating the energy of the first three singlet states. In reality there exists a small Jahn-Teller splitting in the ground X^2E state of the MS product arising from the interaction of the degenerate 3p valence orbitals on the sulfur with the two degenerate e orbitals and single a_1 on the CH_3. This results in there being a lower energy geometry than that suggested by the C_{3V} symmetry. The Jahn-Teller splitting of 0.01 eV is relatively small as is the spin-orbit splitting of 0.045 eV.[60–62] These splittings are ignored in this calculation as the scale of the splittings is irrelevant on the energetic scale of the photoexcitation.[63] The ground A′ state is depicted in blue and the first and second

excited states of A″ symmetry are portrayed in red and green respectively in the C_S symmetry group. As in simpler sulfides and thioethers, such as H_2S[32;33] and MSM[24;64] (the PEC for which is shown in figure 3.5), the first two excited states are close lying in energy. The lower of these two excited states is dissociative along both the B–SM and BS–M bond elongation coordinates which are probed in this study.
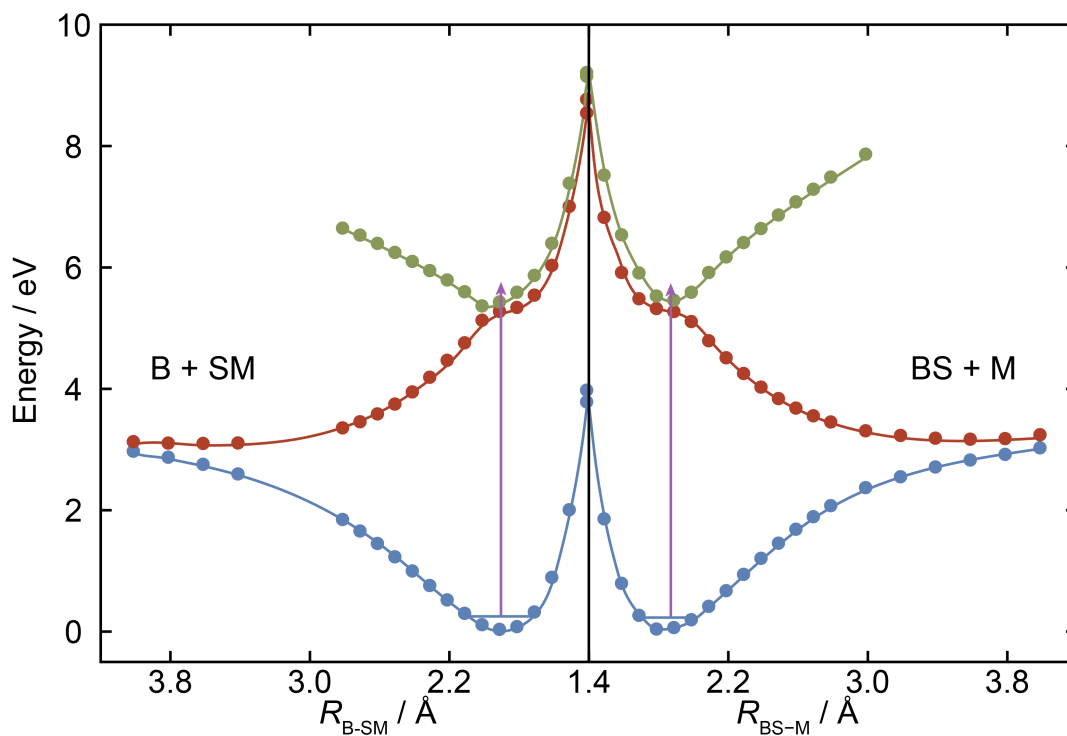
Figure 4.11: Relaxed PECs for the ground ($^1A'$, in blue) and first two excited ($^1A''$, in red and green respectively) states of BSM along the $R_{\text{B–SM}}$ and $R_{\text{BS–M}}$ bond extension coordinates (left and right halves, respectively). The purple arrows show the excitation energy reached by $\lambda = 225.0$ nm photoexcitation from the parent zero-point level.

As discussed in the introduction (section 1.2.3) the potential energy surfaces control the dynamics of all molecular processes. The motive for undertaking these calculations was to attempt to identify a key feature on the PESs that would explain why the dissociation was twice as likely to proceed through the B–SM channel than the BS–M channel. As shown in table 4.1, the calculated bond enthalpies predict that the B + MS pair is lower in energy and thus enthalpically favourable, in line with the observed preference. However, the bond enthalpies are within 0.067 eV of one another which is insignificant on the scale of the process. These bond enthalpies are both extremely similar to the calculated C–S bond dissociation energy for MSM

(3.142 eV) which is, in turn, in excellent agreement with the experimental value of 3.14 ± 0.04 eV. Note that the literature bond dissociation enthalpies for B–SM and BS–M, shown in table 4.1, show a larger discrepancy of 0.14 eV and the ordering is reversed in comparison to the calculated values. As the experimental enthalpy of formation of the BS radical[35;65] carries a relatively large uncertainty in comparison to the others this could contribute to the observed discrepancy and, in conjunction with the method of calculation being verified through the accurate characterisation of the MS–M enthalpy, leads us to give more weight to the present *ab initio* calculations.

The *ab initio* calculations of the ground state equilibrium geometry of BSM return equilibrium bond lengths of $R_{\text{B–SM(e)}} = 1.868\text{Å}$ and $R_{\text{BS–M(e)}} = 1.822\text{Å}$, respectively. The B–SM bond length is marginally longer, suggesting that it is commensurately marginally weaker, but this difference of 0.046 Å, although aligned with the observed bond dissociation preference, also seems like a minor effect that fails to fully account for the observed bond fission preference. Thus the potentials do not present any easy rationale for the observed bond dissociation preference. However, as the photoexcitation is to the diabatically bound A″ second excited state state (green in figure 4.11), and not directly to the dissociative A″ first excited state (red in figure 4.11, there are more subtle effects in play which might affect the outcome. The states are coupled by a seam of intersection along both elongation coordinates and one possible explanation is that the coupling in one coordinate is more efficient. The Landau–Zener formula (equation 1.15) provides a route to calculating the transition probability between the two states but due to the similarities in the potentials it is unlikely this will show a significant difference in the non-adiabatic transition coupling for the linear cuts. It is also possible that the coupling is stronger in a region of parameter space corresponding to the elongation of a different bond or change in angle of between the two C–S bonds. This tuning coordinate might be more readily explored in one C–S bond elongation coordinate over another. This would require a more complete characterisation of the potential energy surface outside the scope of this project. The UV absorption spectra of lighter thioethers, *e.g.* MSM as shown earlier in figure 3.2, shows structure deeper into the blue than just the lowest energy absorption into the $1^1\text{A}''/2^1\text{A}''$ state manifold. It is possible that a higher resolution UV-vis of jet cooled BMS than the room temperature one presented in figure 4.3 might also begin to show undulatory structure in the strong broad absorption feature centred around ~ 213 nm. This structure in the MSM and BSM is suggested to arise from short lived resonances in the $^1\text{A}''$ PESs and an analysis of the transition dipole moments of all of the initial

photoexcitations is required to inform the modelling of the non-adiabatic couplings that mediate the C–S bond extensions and subsequent dissociations.

4.4   Conclusions

This study demonstrates how the coupling of 'universal' single photon ionisation to a multi-mass imaging capability through the PImMS camera opens an avenue to measure the probability of one bond dissociation versus another. This is demonstrated in the UV photolysis of an asymmetric thioether t-butylmethylsulfide (BSM) at wavelengths $\lambda = 227.5$, 225.0 and 222.5 nm, where the preference for B–SM bond fission is approximately twice as likely as the breaking of the BS–M bond. While this technique achieves its goal of determining the relative quantum yields of the processes it is worth considering how extendable and how general the method might be. The method is dependent on a suitable internal calibrant that, under photodissociation, produces fragments that are common to the competitive dissociation channels (*i.e.* M and MS with BS–M and B–SM) which is to say that the target and calibrant molecules differ by only a single moiety. While in principle this is sufficient, due to current limitations on the spatial resolution of detectors capable of multiple mass imaging, these moieties must also differ significantly by mass to ensure that the signals are sufficiently separated on the detector to be resolvable. On the other hand, it is imperative that the moieties do not differ so much in mass that the lighter, faster photofragment might miss the detector (*e.g.* an H atom) when conditions are suitable to image the co-fragment, or that the detection efficiency of one of the fragments be so abundant in intensity to dwarf the cofragment.

The method also doesn't negate the need for a thorough investigation of the energetics of each individual photodissociation channel in the target and calibrant systems to understand the energy disposal into the products, or to ensure no alignment effects are in play which may or may not impact the analysis of the branching fractions as discussed in chapter 3.

It is worth noting that there is no *a priori* reason why the photoionisation efficiencies of all quantum states are equal at a given photoionisation wavelength. This can have a significant effect over the detection efficiencies when the SPI energy is close to the ionisation threshold as demonstrated in the case of measuring both ground and spin–orbit excited I atoms following photodissociation of methyl iodide.[66] To some extent this is guarded against by monitoring the photodissociation of both the target

and calibrant molecules simultaneously. More important is that the calibrant system is chosen so that under the same conditions its photofragments will be formed in a similar spread of quantum states via a similar photodissociation process. This is certainly true for the presented case of BSM and MSM and it seems reasonable to assert that this will be likely to hold true for any pair of molecules within a class of homologous systems.[67]

This work features an example where in an individual molecule one of two bonds will break and reports on the preference across an ensemble of molecules. However, three body fragmentation, where both bonds in a given molecule will break following absorption of a single photon is possible. With reference to the enthalpies of formation in table 4.1, the three body fragmentation of BSM is possible above 6.46 eV ($\lambda =$ 192 nm). The S atoms formed would be amenable to SPI at $\lambda = 118.2$ nm and so this method could, in principle, provide information on the three body dissociation including giving information on rival channels for three body decay.

Nevertheless, even taking into account these various caveats, given access to sufficiently high SPI energies this method should be directly extendable to a range of different systems such as the directly analogous oxygen ethers, unsaturated equivalents such as ketones and thioketones, but also to aromatic analogues such as anisoles and thioanisoles. Also worth considering is extension to amine systems where there are three potential bond fissions which could take place. There is no fundamental reason why this technique would not be applicable to these systems but it is easy to envisage that the equivalent maths shown in section 4.3.2 would be significantly more complicated, and the difficulties demonstrated here of deconvoluting the contribution from each pathway would be magnified. An initial approach might involve an amine where two of the three substituents are alike in order to make finding a suitable internal calibrant easier.

This concludes the work on coupling multi-mass imaging to single photon ionisation. The next chapter covers strong field ionisation as a means to induce Coulomb explosions in molecules with multi-mass imaging again applied to measure the velocities of all fragments produced in a Coulomb explosion.

Bibliography

[1] B. J. Sussman, D. Townsend, M. Y. Ivanov, and A. Stolow, Science **314**, 278 (2006), ISSN 0036-8075.

[2] M. E. Corrales, R. de Nalda, and L. Bañares, Nat. Commun. **8**, 1345 (2017), ISSN 2041-1723.

[3] A. Serrano-Jiménez, L. Bañares, and A. García-Vela, Phys. Chem. Chem. Phys. **21**, 7885 (2019), ISSN 1463-9076.

[4] K. I. Hilsabeck, J. L. Meiser, M. Sneha, J. A. Harrison, and R. N. Zare, J. Am. Chem. Soc. **141**, 1067 (2019), ISSN 0002-7863.

[5] S. S. Brown, R. B. Metz, H. L. Berghout, and F. F. Crim, J. Chem. Phys. **105**, 6293 (1996), ISSN 0021-9606.

[6] F. F. Crim, J. Phys. Chem. **100**, 12725 (1996).

[7] R. L. V. Wal, J. L. Scott, and F. F. Crim, J. Chem. Phys. **92**, 803 (1990), ISSN 0021-9606.

[8] I. Bar, Y. Cohen, D. David, S. Rosenwaks, and J. J. Valentini, J. Chem. Phys. **93**, 2146 (1990), ISSN 0021-9606.

[9] R. L. V. Wal, J. L. Scott, F. F. Crim, K. Weide, and R. Schinke, J. Chem. Phys. **94**, 3548 (1991), ISSN 0021-9606.

[10] I. Bar, Y. Cohen, D. David, T. ArusiParpar, S. Rosenwaks, and J. J. Valentini, J. Chem. Phys. **95**, 3341 (1991), ISSN 0021-9606.

[11] D. Reedy, J. B. Williams, B. Gaire, A. Gatton, M. Weller, A. Menssen, T. Bauer, K. Henrichs, P. Burzynski, B. Berry, et al., Phys. Rev. A. **98** (2018), ISSN 2469-9926.

[12] J. Rajput, T. Severt, B. Berry, B. Jochim, P. Feizollah, B. Kaderiya, M. Zohrabi, U. Ablikim, F. Ziaee, K. R. P, et al., Physical Review Letters **120** (2018), ISSN 0031-9007.

[13] R. E. Continetti, Annu. Rev. Phys. Chem. **52**, 165 (2001).

[14] E. N. Sullivan, B. Nichols, and D. M. Neumark, J. Chem. Phys. **148**, 044309 (2018), ISSN 0021-9606.

[15] E. N. Sullivan, B. Nichols, and D. M. Neumark, Phys. Chem. Chem. Phys. **21**, 14270 (2019), ISSN 1463-9076.

[16] Y. T. Lee, J. D. McDonald, P. R. LeBreton, and D. R. Herschbach, Rev. Sci. Instrum. **40**, 1402 (1969), ISSN 0034-6748.

[17] S. J. Riley and K. R. Wilson, Faraday Discussion **53**, 132 (1972), ISSN 0301-7249.

[18] D. W. Chandler and P. L. Houston, J. Chem. Phys. **87**, 1445 (1987), ISSN 0021-9606.

[19] A. T. J. B. Eppink and D. H. Parker, Rev. Sci. Instrum. **68**, 3477 (1997), ISSN 0034-6748.

[20] M. Bain, C. S. Hansen, and M. N. R. Ashfold, J. Chem. Phys. **149**, 081103 (2018), ISSN 0021-9606.

[21] J. J. John, M. Brouard, A. Clark, J. Crooks, E. Halford, L. Hill, J. W. L. Lee, A. Nomerotski, R. Pisarczyk, I. Sedgwick, et al., J. Instrum. **7**, C08001 (2012), ISSN 1748-0221.

[22] P. Quintana, R. F. Delmdahl, D. H. Parker, B. Martinez-Haya, F. J. Aoiz, L. Bañares, and E. Verdasco, Chem. Phys. Lett **325**, 146 (2000), ISSN 0009-2614.

[23] J. Barr, I. Torres, E. Verdasco, L. Bañares, F. J. Aoiz, and B. Martínez-Haya, J. Phys. Chem. A **108**, 7936 (2004), ISSN 1089-5639.

[24] J.-H. Yoon, K. C. Woo, and S. K. Kim, Phys. Chem. Chem. Phys. **16**, 8949 (2014), ISSN 1463-9076.

[25] J. S. Lim and S. K. Kim, Nat. Chem. **2**, 627 (2010), ISSN 1755-4330.

[26] G. M. Roberts, D. J. Hadden, L. T. Bergendahl, A. M. Wenge, S. J. Harris, T. N. V. Karsili, M. N. R. Ashfold, M. J. Paterson, and V. G. Stavros, Chem. Sci. **4**, 993 (2013), ISSN 2041-6520.

[27] K. C. Woo, D. H. Kang, and S. K. Kim, J. Amer. Chem. Soc. **139**, 17152 (2017), ISSN 0002-7863.

[28] S. L. Li and D. G. Truhlar, J. Chem. Phys. **147**, 044311 (2017), ISSN 0021-9606.

[29] Y. Shu and D. G. Truhlar, Chem. Phys. **515**, 737 (2018), ISSN 0301-0104.

[30] P. Limão-Vieira, S. Eden, P. A. Kendall, N. J. Mason, and S. V. Hoffmann, Chem. Phys. Letts. **366**, 343 (2002), ISSN 0009-2614.

[31] M. B. Williams, P. Campuzano-Jost, D. D. Riemer, C. Tatum, and A. J. Hynes, J. Photochem. Photobiol. **171**, 77 (2005), ISSN 1010-6030.

[32] B. Heumann, K. Weide, R. Dren, and R. Schinke, J. Chem. Phys. **98**, 5508 (1993), ISSN 0021-9606.

[33] D. Simah, B. Hartke, and H.-J. Werner, J. Chem. Phys. **111**, 4523 (1999), ISSN 0021-9606.

[34] K. Watanabe, T. Nakayama, and J. Mottl, J. Quant. Spectrosc. Rad. Transf. **2**, 369 (1962), ISSN 0022-4073.

[35] D. Griller, J. A. M. Simes, and D. D. M. Wayner, *Thermochemsitry of sulfur-centered intermediates in "Sulfur-centered reactive intermediates in chemistry and biology"*, vol. 197 (Springer US, 1990), 1st ed., ISBN 978-1-4684-5876-3.

[36] J. Dyke, N. Jonathan, E. Lee, A. Morris, and M. Winter, Physica Scripta **16**, 197 (1977), ISSN 0031-8949.

[37] D. H. Bross, *Active Thermochemical Tables* (2019), URL https://atct.anl.gov.

[38] S. Choi, K.-W. Choi, S. K. Kim, S. Chung, and S. Lee, J. Phys. Chem. A **110**, 13183 (2006), ISSN 1089-5639.

[39] S. Nourbakhsh, K. Norwood, H. Yin, C. Liao, and C. Y. Ng, J. Chem. Phys. **95**, 5014 (1991).

[40] B. Ruscic and J. Berkowitz, J. Chem. Phys. **97**, 1818 (1992), ISSN 0021-9606.

[41] R. T. Bise, H. Choi, H. B. Pedersen, D. H. Mordaunt, and D. M. Neumark, J. Chem. Phys. **110**, 805 (1999), ISSN 0021-9606.

[42] J. Berkowitz, G. B. Ellison, and D. Gutman, J. Phys. Chem. **98**, 2744 (1994), ISSN 0022-3654.

[43] A. Kramida, Y. Ralchenko, J. Reader, and N. A. Team, *NIST Atomic Spectra Database (version 5.6.1)* (2019), URL https://physics.nist.gov/asd.

[44] B. Nagy, P. Szakacs, J. Csontos, Z. Rolik, G. Tasi, and M. Kallay, J. Phys. Chem. A **115**, 7823 (2011), ISSN 1089-5639.

[45] F. M. Raoult, Comp. Rend. **104**, 1430 (1886).

[46] A. Nomerotski, S. Adigun-Boaye, M. Brouard, E. Campbell, A. Clark, J. Crooks, J. J. John, A. J. Johnsen, C. Slater, R. Turchetta, et al., Nucl. Instrum. Methods Phys. Res., Sect. A. **633**, S243 (2011), ISSN 0168-9002.

[47] A. T. Clark, J. P. Crooks, I. Sedgwick, R. Turchetta, J. W. L. Lee, J. J. John, E. S. Wilman, L. Hill, E. Halford, C. S. Slater, et al., J. Phys. Chem. A. **116**, 10897 (2012), ISSN 1089-5639.

[48] K. Amini, S. Blake, M. Brouard, M. B. Burt, E. Halford, A. Lauer, C. S. Slater, J. W. L. Lee, and C. Vallance, Rev. Sci. Instrum. **86**, 103113 (2015), ISSN 0034-6748.

[49] G. M. Roberts, J. L. Nixon, J. Lecointre, E. Wrede, and J. R. R. Verlet, Rev. Sci. Instrum. **80**, 053104 (2009), ISSN 0034-6748.

[50] B. Buijsse, W. J. van der Zande, A. T. J. B. Eppink, D. H. Parker, B. R. Lewis, and S. T. Gibson, J. Chem. Phys. **108**, 7229 (1998), ISSN 0021-9606.

[51] C. Moeller and M. S. Plesset, Phys. Rev. **46**, 618 (1934), ISSN 0031-899X.

[52] T. H. Dunning, J. Chem. Phys. **90**, 1007 (1989), ISSN 0021-9606.

[53] K. Andersson, P. A. Malmqvist, B. O. Roos, A. J. Sadlej, and K. Wolinski, J. Phys. Chem. **94**, 5483 (1990), ISSN 0022-3654.

[54] K. Andersson, P. Malmqvist, and B. O. Roos, J. Chem. Phys. **96**, 1218 (1992), ISSN 0021-9606.

[55] G. P. F. Wood, L. Radom, G. A. Petersson, E. C. Barnes, M. J. Frisch, and J. A. Montgomery, J. Chem. Phys. **125**, 094106 (2006), ISSN 0021-9606.

[56] M. R. Nyden and G. A. Petersson, J. Chem. Phys. **75**, 1843 (1981), ISSN 0021-9606.

[57] H.-J. Werner, P. J. Knowles, G. Knizia, F. R. Manby, M. Schütz, P. Celani, W. Györffy, D. Kats, T. Korona, R. Lindh, et al., *MOLPRO, version 2018.1, a package of ab initio programs* (2018).

[58] M. J. Frisch, G. W. Trucks, H. B. Schlegel, G. E. Scuseria, M. A. Robb, J. R. Cheeseman, G. Scalmani, V. Barone, G. A. Petersson, H. Nakatsuji, et al., *Gaussian16 Revision B.01* (2016), Gaussian Inc. Wallingford CT.

[59] J. L. Wiza, Nucl. Instrum. Methods **162**, 587 (1979), ISSN 0029-554X.

[60] A. V. Marenich and J. E. Boggs, J. Phys. Chem. A. **108**, 10594 (2004), ISSN 1089-5639.

[61] G. D. Bent, J. Chem. Phys. **89**, 7298 (1988), ISSN 0021-9606.

[62] T. A. Barckholtz and T. A. Miller, Int. Rev. Phys. Chem. **17**, 435 (1998), ISSN 0144-235X.

[63] A. Bouallagui, A. Zanchet, O. Yazidi, N. Jadane, L. Baares, M. L. Senent, and A. Garca-Vela, Phys. Chem. Chem. Phys. **19**, 31245 (2017), ISSN 1463-9076.

[64] M. R. Manaa and D. R. Yarkony, J. Am. Chem. Soc. **116**, 11444 (1994), ISSN 0002-7863.

[65] Y. D. Orlov, V. V. Turovtsev, and Y. A. Lebedev, Russ. Chem. Bull. **50**, 1570 (2001), ISSN 1066-5285.

[66] S. H. Gardiner, M. L. Lipciuc, T. N. V. Karsili, M. N. R. Ashfold, and C. Vallance, Phys. Chem. Chem. Phys. **17**, 4096 (2015), ISSN 1463-9076.

[67] M. N. R. Ashfold, G. A. King, D. Murdock, M. G. D. Nix, T. A. A. Oliver, and A. G. Sage, Phys. Chem. Chem. Phys. **12**, 1218 (2010), ISSN 1463-9076.

Chapter 5

Coulomb Explosion Imaging

5.1   Introduction

Thus far the results reported in this thesis have been confined to studying photofragmentation which has been one of the main *raisons d'être* of the velocity map imaging technique for much of its lifespan. Photofragmentation, however is not the only possible outcome of a photodissociation process, as the dissociation may result in a ring opening or isomerisation where the photoproduct is a structural isomer of the original molecule. Consider the thioethers which have been at the forefront of this thesis. The driving force for their photochemistry can be described in the framework of a nσ* type excitation where a non-bonding electron localised on the sulfur is excited to the diabatically bound S_2 excited state which quickly couples non-adiabatically to a dissociative S_1 state leading to photodissociation. It is well recognised that the photodissociation of small molecules is similar throughout classes of molecules,[1] and that this similarity extends between similar classes of system, i.e. amines and pyrroles or ethers and phenols. As a result, the C–S bond cleavage, which is the inevitable fate in the photodissociation of thiothers might reasonably be expected to dominate the photochemistry of thiophenes following an analogous $\pi\sigma$* excitation as shown in figure 5.1. It has been well established that the photochemistry of thiophenes is dominated by an optically bright transition from the ground electronic state to a $\pi\pi$* type excited state with the transition dipole moment lying in the plane of the ring.[2] In the case of 2-bromothiophene, this transition dipole moment points between the S and Br atoms.[3] At excitation wavelengths above $\sim$255 nm the $\pi\pi$* state quickly couples non-radiatively to a $\pi\sigma$* state along the C–Br bond which is consistent with observations of other aryl halides.[4] However at wavelengths below $\sim$255 nm the C–Br fragmen-
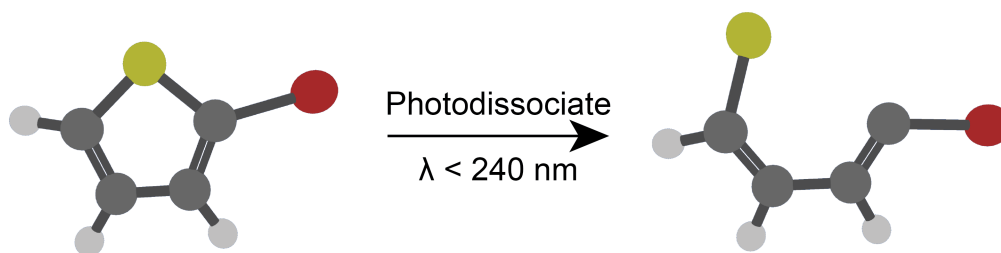
Figure 5.1: Schematic of the ring opening process predicted to occur in 2-bromothiophene following absorption of a single UV photon with a wavelength shorter than 240 nm (5.16 eV).

tation channel is deactivated and cleavage of the C–S bond is predicted to become the primary photodissociation channel.[3;5] This will lead a ring opened photoproduct which has the same mass as the parent and thus is inseparable by mass spectrometry. Beyond this, the photodissociation will not impart any velocity in an axis perpendicular to the time of flight axis which might be measured by VMI. To this end, a new technique for investigating unimolecular photochemical processes which do not result in fragmentation has emerged called Coulomb Explosion Imaging (CEI) which seeks to turn the VMI technique on its head; with the dissociation of the molecule acting as the probe, rather than being the dynamical process under investigation.

A Coulomb explosion involves the stripping of multiple electrons from a molecular species to create a highly charged parent. Molecular structure is, in a simple picture, a delicate balance of the repulsive forces between pairs of nuclei or pairs of electrons, and the attractive forces between nuclei-electron pairs. The more electrons that are ripped away, and the more highly charged cation state that is prepared, the more dominant the repulsive forces become. At some point for a given system, the charge state moves to a regime where the molecule is completely unstable and "explodes" sending charged molecular fragments or atoms racing away from one another. At the limit of this - where no electrons are left in the system, this process is well modeled as a purely classical interaction of like point charges. If one could instantaneously prepare a system in a charge state that is modelled by the classical regime and measure the asymptotic velocities of the particles then, in principle, the geometric structure at the moment of the Coulomb Explosion can be backed out. If this charge build up is faster than the nuclei can rearrange (*i.e.* a few tens of femtoseconds) then this can provide

a structural diagnosis of the transient state from which the Coulomb Explosion was initiated.

Coulomb explosions themselves are not an entirely new type of experiment having their roots in non-laser based methods since the 1970s. The earliest examples of Coulomb explosions were initiated by accelerating stable, singly charged, molecular ions to translation energies in the MeV range (in the region of a few percent of the speed of light) before colliding with a carbon or Formvar foil with a thickness on the order of tens of Å.[6–8] The foil is thin enough that the nuclei can pass through while the electrons are stripped by interaction with the electrons in the foil, with the stripping process projected to take approximately 100 attoseconds (the transit time through the foil taking on the order of a few hundred attoseconds). These experiments have proven invaluable for investigating the structures of a wealth of interesting molecular ions such as CH_4^+, in which a Jahn-Teller distortion was observed,[9] and $C_2H_3^+$,[10] in which a discrepancy between the experimentally derived structure and that which was predicted by theory was identified. This was eventually resolved when Marx and Parrinello demonstrated good agreement between the experimentally observed structure of $C_2H_3^+$ and the optimum structure of one of its electronically excited states.[11] This emphasises the issue which pervaded early Coulomb explosion experiments, the molecular ion of interest was not guaranteed to be prepared energetically 'cold'. To ensure the molecules are cold, the optimum medium to induce the explosion would be a freely expanded molecular beam where the molecules have had time to undergo a sufficient number of collisions to internally cool. This is incompatible with stripping the electrons using a thin foil as the neutral molecules cannot be accelerated to sufficiently high energies.

With the advent of modern modelocked and regeneratively amplified lasers which can produce pulses of light that last for only a few tens of femtoseconds with mJ pulse energies, molecules can be subjected to peak laser field intensities in the region of hundreds of terawatts per square centimetre. In this intensity regime, commonly referred to as the "strong-field" regime, non-linear processes begin to dominate the interaction and the intramolecular electrostatic interactions are distorted to allow electrons to rapidly tunnel out of their potential well and effectively form a highly charged state in a process known as tunnel ionisation (see section 1.9 for more detail). As well as allowing the Coulomb explosion to take place in a colder molecular beam allowing more control over the probe, this carries another advantage in that it abdicates the requisite for an ionic molecular precursor thus extending the technique

to neutral species. Although the Coulomb explosion process could, in principle, take place on a timescale up to a hundred times longer than that in a foil collision, this is still shorter than the typical period of nuclear motion.

As described thus far, Coulomb Explosion Imaging manifests as a probe of molecular structure but it is worth noting that its ability to characterise structure is far less refined than say NMR or microwave spectroscopy. The advantage of Coulomb Explosion Imaging (henceforth, CEI) is that when coupled to ultrafast laser pulses it provides an approximate measure of the structure with a timescale of a few tens of femtoseconds. This is, crucially, shorter than the timescale of evolving nuclear geometry on the excited state.

A significant amount of groundwork has been laid by a collaboration by the Brouard and Vallance groups at Oxford with, initially the Stapelfeldt group at Aarhus and later a consortium working primarily at the Deutsches Elektronen-Synchrotron. In the early days of this collaboration, Coulomb explosion imaging was demonstrated on a variety of equilibrium ground state molecules such as the 3,5-dibromo-3′,5′-difluoro-4′-cyanobiphenyl molecule shown in figure 5.2.[12–14] This molecule does not hold any particular interest for its chemical properties but is tailor made to demonstrate

Figure 5.2: Ground state structure of 3,5-dibromo-3',5'-difluoro-4'cyanobiphenyl.

a large molecule, with a large number of easily distinguishable atoms (such as F, Br and N) which act as so called marker atoms, to help elucidate the molecular structure. This represents a significant step up in size over previous molecules studied by CEI which have been restricted to small molecules, for example, H_2,[15;16] SO_2,[17] and small alkyl halides.[18;19]

Coulomb explosions can also be induced by extremely high energy photons which extract a core electron from the molecule, the subsequent Auger decay[20;21] releases further electrons resulting in a multiply charged species which can Coulomb explode. The Auger decay process is estimated to take place on a timescale of attoseconds to tens of femtoseconds[22] and so in principle better preserves the molecular structure
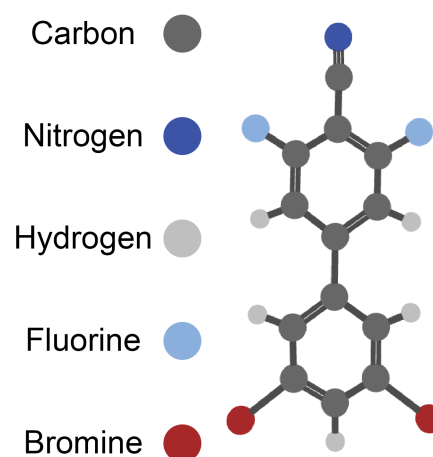
throughout the ionisation process prior to Coulomb explosion. A comparison of core ionisation and strong field ionisation approaches is demonstrated at the FLASH free electron laser at DESY on the Coulomb explosion of the difluoroiodobenzene molecule, a similarly marker laden polyatomic to the biphenyl molecule studied previously. The crucial observation from this comparison is that strong field induced Coulomb explosions have a significant preference for the explosion axis to be orientated along the polarisation axis of the multiphoton field. In contrast, the XUV pulse appears to have no significant orientation effect perhaps making it more suitable for unbiased structural diagnosis. It may, however, be the case that the initial XUV photoabsorption is just as likely to have an orientational dependence, and that this is just scrambled prior to dissociation by the intermediary Auger decay process.

The ability to determine the ground state structure can also be used to determine the ratio of structural isomers in a mixed sample as demonstrated by the study of substituted benzene rings such as difluoroiodobenzene or dihydroxybromobenzene where the positions of the fluorine atoms and hydroxy groups on the respective benzene rings are changed.[23] Prospectively, this might be used to disentangle the products of a photoisomerisation starting with an isomer pure sample *e.g.* cis-trans isomerisation.

Coulomb explosion imaging has also begun to be applied to excited state dynamics. Thus far this has been constrained to UV photodissociation dynamics, where, following an excitation with an ultrafast UV pulse, Coulomb explosions are initiated by a second ultrafast laser pulse (either in the infrared or XUV regions, as discussed earlier) which is time delayed from the excitation. The kinetic energy resulting from the Coulomb explosion of a given charged parent state into a pair of correlated products (e.g. AB^{2+} exploding into $A^+ + B^+$) is then tracked as a function of pump-probe delay in order to track the dynamics in time. The kinetic energy will be directly dependent upon the distance between A and B ($R_{A\text{--}B}$) and, as the molecule dissociates, the kinetic energy of the Coulomb explosion decreases. This provides an insight into the kinetics of the dissociation process (provided the dissociation timescale is longer than the instrument response function). This technique has successfully unravelled complex mechanisms such as the sequential dissociation of CH_2IBr into $CH_2Br + I$ followed by dissociation of CH_2Br into $CH_2 + Br$ following absorption of a second UV photon[24] and that there is competition between two and three body dissociation in CH_2ClI.[25]

By far, the most studied excited state process using Coulomb explosion imaging is the photodissociation of methyl iodide.[25--27] The $^3Q_0$ and $^1Q_1$ states of methyl iodide

encounter a conical intersection *en route* to fission of the C–I bond with the states correlating diabatically with the spin-orbit excited $^2P_{\frac{1}{2}}$ and ground state $^2P_{\frac{3}{2}}$ iodine atoms, respectively, with the CH_3 being formed exclusively in its ground electronic state $\tilde{X}$. The well defined excited state dynamics have positioned methyl iodide as a popular testing ground for a variety of new experimental techniques such as transient XUV absorption [28] or for exploring the effect of a weak IR field on manipulating conical intersections to control dynamics [29] and this is no doubt responsible for its prevalence in the Coulomb explosion imaging community.

The goal of this chapter is to outline early efforts to build a new experiment in Bristol capable of investigating excited state dynamics through time resolved Coulomb Explosion imaging. It covers the design of a simple beam path to produce both high intensity 800 nm probe laser pulses and much lower intensity 267 nm UV pulses in tandem for pump probe spectroscopy. The experiment is then tested on CH_3I and CF_3I which have been previously investigated and some preliminary reports are offered to suggest that the 2-bromothiophene system will be a suitable first effort for finally nailing down the ring opening process in isolated gas phase molecules.

5.2   Experimental

The experimental set up is described in detailed in chapter 2 and only an outline of the specific conditions for this chapter are provided here. The sample of interest, CH_3I (Sigma-Aldrich, stated purity > 99%), CF_3I (Sigma-Aldrich, stated purity > 99%) or 2-bromothiophene (Sigma-Aldrich, stated purity > 99%) was seeded in helium (5%, 800 mbar backing pressure) and the resultant mixture expanded through a pulsed valve in the source vacuum chamber. The central coldest part of the molecular beam was selected by a skimmer with a 1 mm orifice *en route* to the differentially pumped interaction region. Entering through a hole in the centre of the repeller plate of the VMI optics assembly, the molecular beam wass intercepted by the probe laser beam. This axis was defined as the z axis. The probe laser beam was formed taking the 5 mJ 800 nm 35 fs output (5W at 1 kHz) of a regenerative amplified Ti:Sapphire laser (Coherent Astrella-1K-USP) and splitting it via a beam splitter for independent pump and probe arms. The reflected probe beam entered a retroreflector mounted on a delay stage following which the intensity of the beam was then attenuated via a $\lambda/2$ waveplate thin film polariser pair. The temporal chirp acquired by the pulse in all these interactions was compensated for by reflecting the beam off four chirp corrective

mirrors. The mirrors also applied a pre-chirp to the pulse to account for the effects of optics further down the beam path. Following this the beam was manipulated to the chamber by purely reflective optics where it then passed through a focussing lens (f.l. = 20 cm) and a 2 mm thick window which coupled it into the vacuum system. The laser beam then intersected the molecular beam at right angles, with the laser beam defining the y axis with the polarisation of the laser oriented out of the plane formed by the laser and molecular beams - defining the x axis. The cations formed by the resulting Coulomb explosions or dissociative ionisation were accelerated along the z-axis by the VMI optics before entering the 46 cm field free drift region before striking a triple stack MCP detector coupled to a P47 phosphor screen (Photek VID340). The screen was imaged by a PImMS2 sensor[30–32] through a Nikon NIKKOR 55 mm macro-lens ($f/2.8$). The time resolution of the PImMS2 sensor was set to 25 ns which, for the ion optics voltages employed in this chapter, provided 5-7 time slices through each m/z peak of interest.

The PImMS data were first processed by centroiding the (x, y, t) data[33] according to the algorithm outlined in section 2.6.1 to reduce the clusters to single ion events. Mass spectra were generated by binning all events according to arrival time (in time bins), and converting to a mass spectrum by applying a time of flight calibration derived from the flight times of known fragments and compensating the intensities by an appropriate Jacobian transformation (section 2.6.2). Ion images were extracted by binning all the intensities in a given set of time bins associated with one mass peak into a 2d array according to their x, y coordinates. The radial distributions were extracted by taking the intensity of each pixel, converting its x,y coordinate into polar coordinates and binning it into a 1d array according to the returned radial value. The resulting radial distributions were scaled according to speed (by calibration as discussed in section 2.6.5) and converted into either a momentum distribution by multiplying by mass or, where the cofragment was known, into TKER space by squaring the velocities and multiplying by half the fragment mass and converting via the TKER equation (section 2.6.6) in the latter scenario, scaling the intensities by an appropriate Jacobian to compensate for the scaling with the square of velocity.

The recoil frame covariance analysis was executed using a piece of code written by colleagues at Oxford University which was modified from an earlier version which was reported in the literature.[34] There is also a thorough review of covariance as applied to a variety of spectroscopic techniques by Frasinski et al.[35] The mathematical foundations of covariance analysis are discussed in the introduction (section 1.2.9) but

the concept of doing this in the recoil frame requires further expansion here.

For each ion event detected there are two recorded variables, an x and y position. In the same vein as covariance between two vectors (say time of flight with time of flight) producing a covariance matrix, to fully expand the covariance between two matrices would require a four dimensional tensor product. As four dimensional tensors are conceptually complex and difficult to implement, the recoil frame represents a reduced dimensionality approach to simplify the analysis.

With reference to the covariance equation (first described in equation 1.19 but restated below) the basis of the algorithm involves generation of two independent components $\langle XY \rangle$ and $\langle X \rangle \langle Y \rangle$

$$\text{cov}(X, Y) = \langle XY \rangle - \langle X \rangle \langle Y \rangle \tag{5.1}$$

Within each laser shot there are a given number of particles detected in the mass window associated with X and another set of particles detected within the mass window for Y. Within this set of two lists of particles there will be both true and false coincidences. The definition of a true coincidence is a pair of different particles detected in the same laser shot and, crucially, originating from the same molecule. A false coincidence is the detection of a pair of different particles within the same laser shot but originating from different molecules. There is no *a priori* way to distinguish true and false coincidences.

We start with an empty matrix of a suitably large size with respect to the given two mass channels, called the $\langle XY \rangle$ matrix, and designate one mass channel as the reference and one as the sample. Within one laser shot, for every particle in the reference image, the x,y coordinates are converted to polar coordinates θ_{ref} and r_{ref} then for every particle in the sample image the sample x-y coordinates are converted to polar coordinates. For all sample particles the θ_{ref} value is subtracted from θ_{sample} to convert to the "recoil frame" and the resulting r_{sample}, θ_{sample}-θ_{ref} polar coordinate is converted back to cartesian coordinates and the intensity of the corresponding pixel in the $\langle XY \rangle$ matrix is increased by 1/M where M is the number of reference particles in this laser shot. This is then repeated for every particle in the reference image. Then this entire process is repeated for every laser shot to produce the final recoil frame $\langle XY \rangle$ matrix. To produce the $\langle X \rangle \langle Y \rangle$ matrix, the two ion images are accumulated in the conventional manner by summing over all laser shots without rotations in any coordinate spaces to produce $\langle X \rangle$ and $\langle Y \rangle$ and a blank matrix $\langle X \rangle \langle Y \rangle$ is constructed. For every pixel in the reference image $\langle X \rangle$, the polar coordinate of that pixel is

calculated then for each pixel in the sample image $\langle Y \rangle$, the polar coordinates are also calculated and the coordinates are transformed into the recoil frame by subtracting the θ for the current $\langle X \rangle$ pixel from the polar coordinate of every pixel in $\langle Y \rangle$ to transform $\langle Y \rangle$ into the recoil frame. The intensities of the recoil frame $\langle Y \rangle$ are deposited into the $\langle X \rangle \langle Y \rangle$ matrix after multiplying them all by the intensity in the current $\langle X \rangle$ pixel. This is repeated for every $\langle X \rangle$ pixel.

We now have an $\langle XY \rangle$ matrix and $\langle X \rangle \langle Y \rangle$ matrix however, due to the way the matrices are constructed, $\langle X \rangle \langle Y \rangle$ is overcounted by a factor of the number of laser shots (N) and so the intensity of each pixel must be divided by N before subtracting from $\langle XY \rangle$ to retrieve the covariance matrix.

5.3 Results

5.3.1 Methyl Iodide

As discussed, methyl iodide has long served as a popular system for benchmarking new experiments as both its ground state structure[36] and its excited state dynamics[37–39] have been thoroughly characterised. As such, it has proven one of the most popular test beds for new Coulomb explosion experiments in both its ground and excited states and the experiment at Bristol will be no different. Although the ambition is to use CEI as a probe of excited state dynamics, the initial experiments will characterise the Coulomb explosion of the ground state, in the spirit of walking before running.

Figure 5.3 shows the mass spectrum collected following strong field ionisation of methyl iodide by a 33 fs 178 μJ laser pulsed centred at $\lambda = 800$ nm with an intensity of approximately 274 TW cm^{-2}. By broadly considering the entire spectrum we can draw some initial conclusions. Five distinct peaks are observed (by considering the N_2^+ and O_2^+ peaks to have coalesced) with the highest charge on an individual fragment the I^{3+}. From this we can deduce that the minimum parent charge state reached is CH_3I^{3+}. The iodine is also monitored in I^{2+} and I^+ charge states where the signal is significantly higher implying that the lower charge states are more readily produced, although the spectrum does not tell us how many pathways might lead to their formation.

The mass resolution of the experiment when recorded through the PImMS camera is not sufficient to resolve the separate N_2^+ and O_2^+ peaks with the N_2^+ appearing as a shoulder to lower mass than O_2^+. This is assigned as an impurity in the experiment.
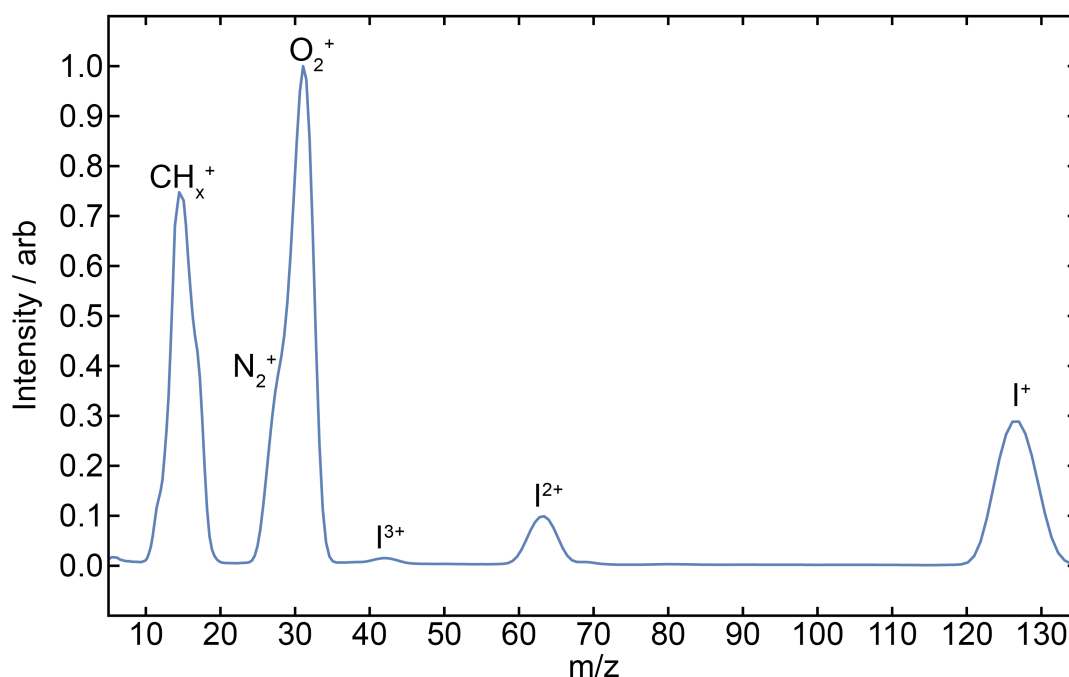
Figure 5.3: Mass spectrum obtained from calibration of TOF spectra measured following Coulomb explosion of jet cooled methyl iodide at by a 33 fs 178 μJ laser pulse centred at $\lambda = 800$ nm. The detector sensitivity is set to high for all photofragments within the figure frame.

The peak centered around m/z 15 is loosely assigned as CH_X where X can take any value between 3 and 0 implying that an H atom is easily lost in this violent strong field ionisation and that the mass resolution is not sufficient to resolve one Dalton differences in this region.

Although there is a significant contribution to the m/z from highly charged states of I, there is no evidence for higher ionised states of CH_x. This can be rationalised with reference to the molecular orbitals of the CH_3I molecule. A schematic of the molecular orbitals formed by overlapping the molecular orbitals of the CH_3 fragment with the atomic orbitals of I is shown in figure 5.4.

The three orbitals that make up the a_1 and e molecular orbitals of CH_x originate as the $2p$ orbitals of the central carbon. If we define the C–I bonding axis at z, the $2p_x$ and $2p_y$ orbitals of carbon are highly involved in bonding to the group orbitals of the three hydrogen atoms and form a degenerate pair significantly lower in energy than the a_1 orbital which started out life as a carbon $2p_z$ orbital. This $2p_z$ orbital is less involved in bonding to the three hydrogen group orbitals as it is out of plane as
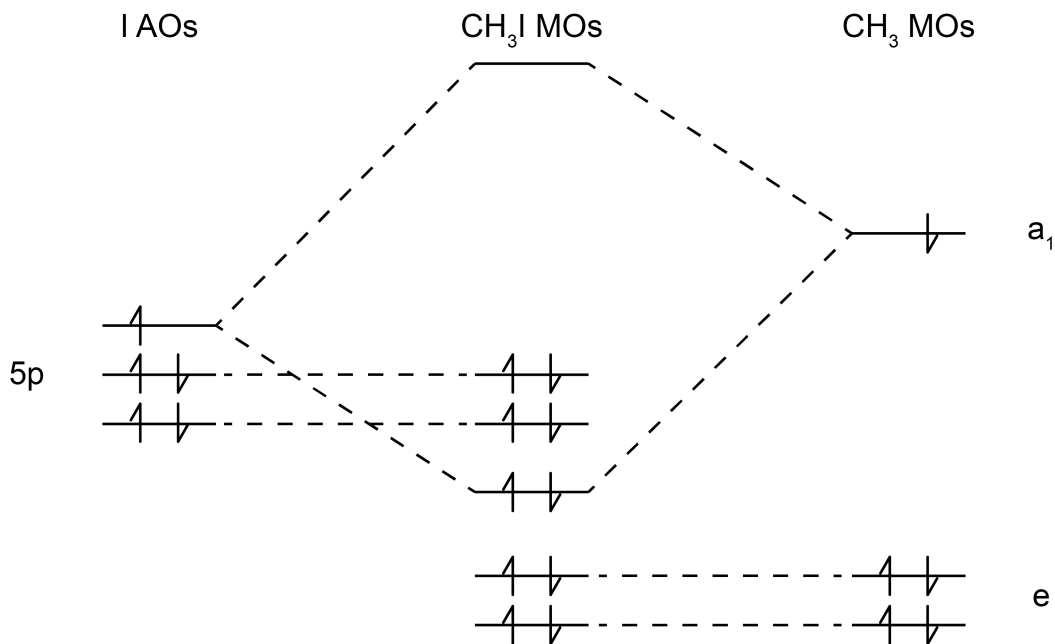
Figure 5.4: Schematic of the molecular orbitals involved in the bond formation or dissociation of the C–I bond in CH_3I derived by mixing the molecular orbitals of the CH_3 radical with the atomic orbitals of Iodine.

a result of which it is not lowered significantly in energy. When we bring these CH_3 orbitals together with the iodine atomic orbitals, the a_1 and e orbitals are energetically close to the $5p$ valence orbitals of the iodine. The CH_3 e orbitals are orthogonal to this interaction and so do not interact with the iodine. However the a_1 ($2p_z$ like) orbital can form a sigma bond with the iodine $5p_z$ orbital as shown. The iodine $5p_x$ and $5p_y$ orbitals again sit out of the CH_3–I bonding axis and so do not interact with the CH_3 fragment. Because of the stabilisation afforded by the CH_3 a_1 I $5p_z$ bonding interaction, the I $5p_y$ and I $5p_x$ non-bonding orbitals become the valence orbitals HOMO and HOMO-1. This would imply that, in a frozen electron picture, the first four charge states of methyl iodide, CH_3I^{1+} - CH_3I^{4+}, would all locally ionise on the iodine before the CH_3I^{5+} ionisation state might collapse to either CH_3^+ I^{4+} or CH_3 + I^{5+}. The observation of CH_3^+ in the absence of I^{4+} suggests that lower ionisation states must undergo electronic reorganisation to distribute the charge more evenly across the two fragments on a timescale less than 35 fs. These electronic relaxation processes are in fact predicted to take place on an attosecond timescale similar to other purely electronic processes.[22]

Figure 5.5 shows the ion image associated with the CH_x peak in the left hand panel,
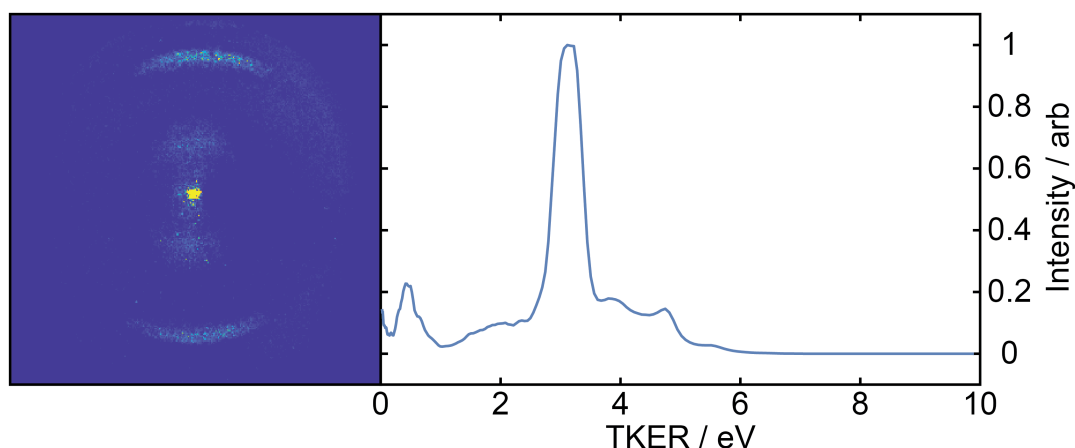
Figure 5.5: The left hand panel shows the ion image associated with the m/z 15 CH_3^+ fragment collected following the Coulomb Explosion of CH_3I in an 800 nm 33 fs laser field with an intensity of $\sim 3\text{x}10^{14}$ W cm^{-2} with the electric vector oriented vertically in the plane of the image. The right hand panel shows the TKER retrieved by integrating the radial distribution of the image around all angles and converting to TKER space assuming an Iodine co-fragment.

with its associated TKER spectrum in the right hand panel assuming an iodine co-fragment. There are two peaks in the TKER spectrum located at $\sim$0.5 eV and $\sim$3.1 eV respectively with the 3.1 eV peak being dominant. Assignment of these is helped by comparison with the I^+ ion image and the TKER spectrum of the I^+ yield assuming a CH_3 co-fragment as shown in the left and right panels of figure 5.6, respectively.

The I^+ TKER spectrum also shows peaks at 0.6 eV and 3.7 eV however both of these peaks are of similar peak intensity. This tends to confirm that there are two matched channels. Because these matched channels both result in 1+ charge states we can rule out their precursors as being a parent charge state of greater than 2+. Hence we can confidently assign the 3.7 eV TKER channel to the Coulomb explosion of CH_3I^{2+} into CH_3^+ and I^+ and the channel at 0.6 eV as the dissociative ionisation of CH_3I^+. There is a significant preference for the dissociative ionisation of CH_3I^+ to form $I^+ + CH_3$ as opposed to $I + CH_3^+$ which can be rationalised by reflecting on the molecular orbital diagram in figure 5.4. As previously discussed, the first four electrons in the HOMO and HOMO-1 are non-bonding electrons localised on the iodine driving a preference for I^+ formation.

Turning now to the more highly charged species, figure 5.7 shows the ion image corresponding to the I^{2+} peak at m/z 63.5 in the left hand panel with the TKER
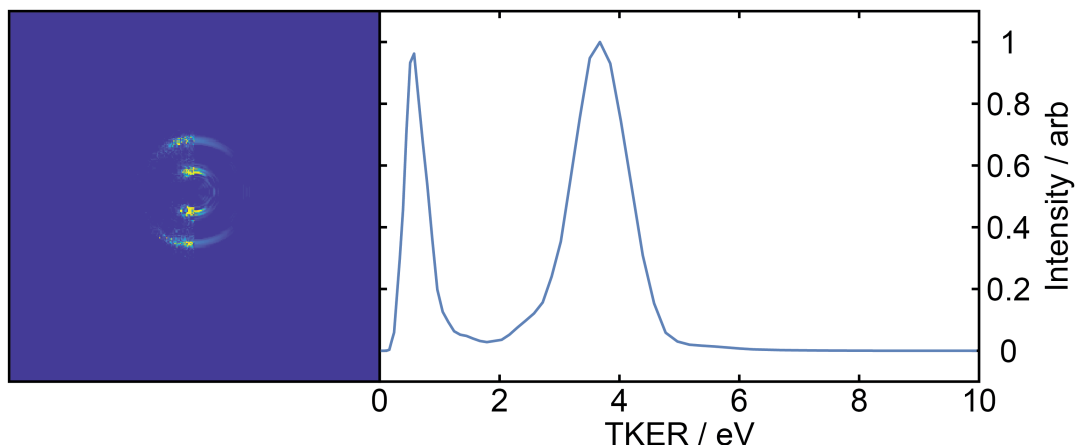
Figure 5.6: The left hand panel shows the ion image associated with the m/z 127 I^+ fragment collected following the Coulomb Explosion of CH$_3$I in an 800 nm 33 fs laser field with an intensity of $\sim 3 \times 10^{14}$ W cm^{-2} with the electric vector oriented vertically in the plane of the image. The right hand panel shows the TKER retrieved by integrating the radial distribution of the image around all angles and converting to TKER space assuming a CH$_3$ co-fragment.

spectrum in the right hand panel. The TKER spectrum was calculated assuming a CH$_3$ cofragment. This manifests as a broad single peak. The broadness of the peak and the slight shoulder on the lower energy side are suggestive of several features masked beneath. If we are correct that the assignment of the Coulomb explosion of CH$_3$I^{2+} into CH$_3^+$ and I$^+$ fragments has a kinetic energy of 3.67 eV then we can predict the kinetic energy into higher charged pairs of fragments within a simple classical model.

The potential energy interaction between two charged species is given by Coulomb's equation which takes the following form:

$$V(r) = \frac{1}{4\pi\epsilon_0 r} . Q_{Me} Q_I \tag{5.2}$$

where V is the potential energy of the interacting charged particles, ϵ_0 is the vacuum permittivity constant, r is the distance between the two interacting charged particles and Q_{Me} and Q_I are the charges on the relative species. Under the assumption that the strong field ionisation is instantaneous we can keep the r value constant at the point of formation for all species and calculate the potential interaction energy as linear with the product of Q_{Me} and Q_I. Hence, it stands to reason that the kinetic
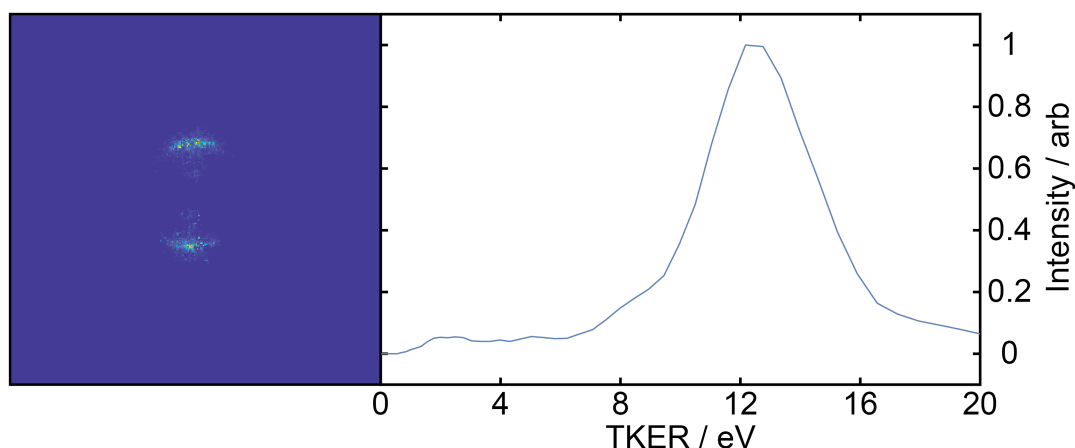
Figure 5.7: The left hand panel shows the ion image associated with the m/z 63.5 I^{2+} fragment collected following the Coulomb Explosion of CH_3I in an 800 nm 33 fs laser field with an intensity of $\sim 3x10^{14}$ W cm^{-2} with the electric vector oriented vertically in the plane of the image. The right hand panel shows the TKER retrieved by integrating the radial distribution of the image around all angles and converting to TKER space assuming a CH_3 co-fragment.

energy release associated with CH_3I^{3+} into a pair of 2+ and 1+ fragments should be $\sim$7.3 eV. This is quite a bit lower in energy than the peak in the spectrum and not convincingly covered by the broad peak. Alternatively, the I^{2+} peak may have originated from a CH_3I^{4+} and been formed alongside a CH_3^{2+} cofragment. This would have a predicted TKER release of 14.7 eV, which matches much better with the experimentally observed peak, although is not an entirely satisfying fit, bringing the simple Coulombic repulsion model in equation 5.2 into question.

Figure 5.8 shows the ion image for the I^{3+} peak at m/z 42.3 in the left hand panel with the TKER spectrum assuming a CH_3 cofragment in the right hand panel. This is perhaps the most complex of the spectra retrieved with multiple sub features contributing to its shape. A tentative, although perhaps optimistic, assignment would be to identify a feature at $\sim$11 eV which, by extension of the simple Coulombic model used thus far, corresponds to the expected value for the dissociation of CH_3I^{4+} into CH_3^+ and I^{3+}. I^{3+} could also be formed from CH_3I^{5+} as a pair with CH_3^{2+} which would appear at around 22 eV in the Coulomb model. There is some evidence for a shoulder on the distribution that might correspond to a peak originating from a 5+ parent charge state but much of the peak is centred significantly below 22 eV. Given how high a charge state would need to be prepared we can reasonably expect this to
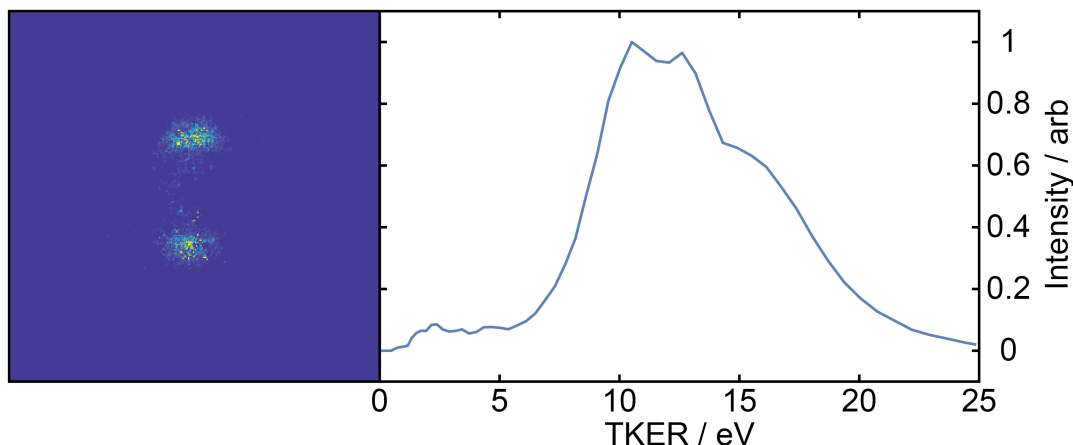
Figure 5.8: The left hand panel shows the ion image associated with the m/z 42.3 I^{3+} fragment collected following the Coulomb Explosion of CH_3I in an 800 nm 33 fs laser field with an intensity of $\sim 3x10^{14}$ W cm^{-2} with the electric vector oriented vertically in the plane of the image. The right hand panel shows the TKER retrieved by integrating the radial distribution of the image around all angles and converting to TKER space assuming a CH_3 co-fragment.

be a less intense minor product channel.

The peaks in the I^{2+} and I^{3+} TKER spectra should, of course, have corresponding peaks in the CH_3^+ and CH_3^{2+} spectra, but these are unobserved as their kinetic energies are too high to be recorded by the limited size of the detector.

The kinetic energy values of these peaks in the iodine spectra correlate quite well with the observations in the methyl iodide studies by Zhang[40], Corrales[41], Wang[42] or Liu[43], which are summarised in Table 5.1. If we take the kinetic energies for the various charge pairs reported in the literature and plot them against the total charge of the assignment, corresponding to Coulomb's law, then it returns a pleasingly straight line, giving credence to both the observations and assignments in these papers. By using this trend in the Zhang data, and rearranging Coulomb's law, equation 5.2 we can back out a value for the C–I bond length (r) at the point of ionisation. This returns an r value for the C–I bond length in methyl iodide of 4.6 Å. This is clearly wrong, as the literature value for the C–I bond in MeI is 2.132 $\pm$ 0.001 Å[44] but it is wrong in the way we might expect given the rather poor assumption required to apply the Coulomb model. The Coulomb model ignores the bonding interactions between the CH_3 and I systems given by the electron nuclei interactions and assumes they are point charges which have no counter forces to overcome en route to C–I bond fission.

Hence, we might expect the pure Coulombic repulsion model to underestimate the bond strength. In principle, the simple Coulombic explosion picture should become more valid at higher charge states as opposed to lower charge states where the bonding interactions are still significant on the scale of the repulsion energies.

I	This work	Zhang et al[40]	Liu et al[43]	Wang et al[42]	Corrales et al[41]	Assigned CH_3 charge
1+	0.39	0.43 ± 0.12	0.43	0.46	0.55	1
1+		0.65	0.86		1.06	2
2+	0.78	0.80 ± 0.07	0.85		1.06 ± 0.1	1
2+		1.32 ± 0.04	1.62			2
2+		2.15 ± 0.05	2.37	3.32		3
3+	1.22					1
3+	1.58	2.04 ± 0.08	2.22	2.58	4.26	2
3+		3.21 ± 0.05	3.60			3

Table 5.1: Kinetic energies (in eV) assigned to observed peaks in the I, I^{2+} and I^{3+} spectra and the equivalent observations from literature. The final column shows the assigned cofragment CH_3 charge state used to plot figure 5.9.

There is an interesting implication contained within all of this for the formation of CH_3I^{4+}. Two Coulomb explosion pathways are available, $CH_3I^{4+} \rightarrow CH_3^{2+} + I^{2+}$ and $CH_3I^{4+} \rightarrow CH_3^+ + I^{3+}$ (and its opposite charge pairing). In the simple Coulomb's law picture, these two pathways have different potential energies associated with the charge interaction.

With respect to the molecular orbital diagram in figure 5.4, we know that the first four electrons removed are likely to be the non-bonding electrons on the iodine. This introduces another complexity to the formation of any given fragment in a given charge state. The attosecond electronic rearrangement process not only enables the formation of Coulomb pairs below 4+ but must have some effect on the distribution within that given the propensity to rearrange into, for example, the 2+ and 2+ charge pair vs the two 1+ and 3+ charge pairs.
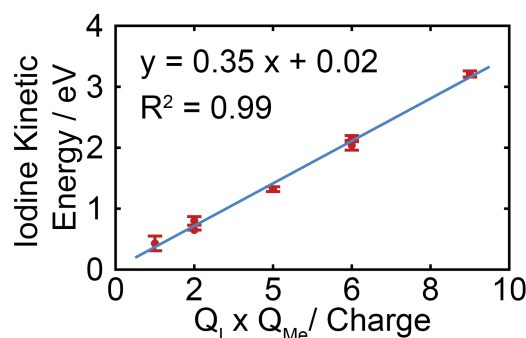

Figure 5.9: Kinetic energy values for observed peaks in the Zhang data[40] plotted against the product of the observed iodine charge state and the assigned CH_3 charge state. These are fitted to a linear model.
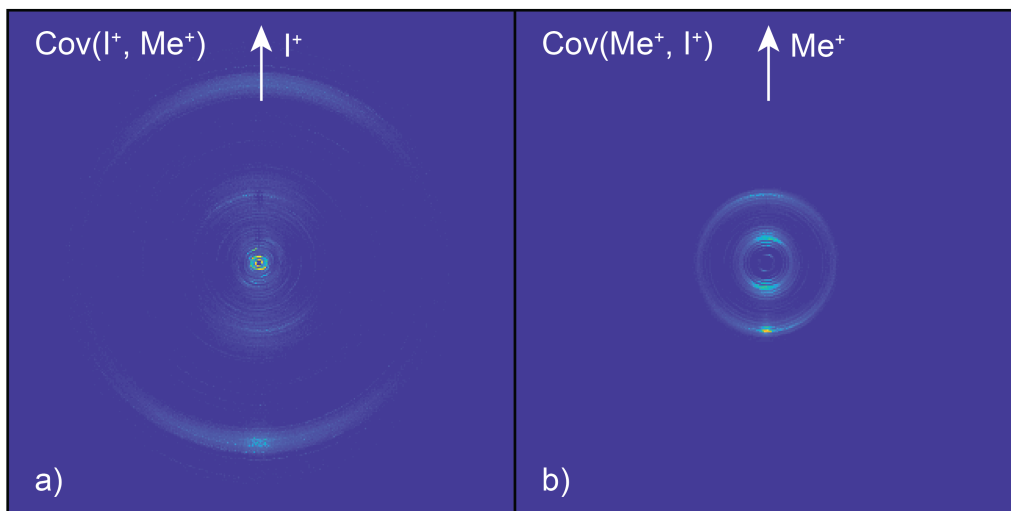
Figure 5.10: Recoil Frame Covariance images of the a) Me^+ recoiling with respect to I^+ oriented along the arrow pointing towards the top of the image, and b) and I^+ recoiling with respect to Me^+ oriented along the arrow pointing towards the top of the image. These are extracted from ion images collected following strong field ionisation initiated by a 33 fs 204 uJ light pulse centred at $\lambda = 800$ nm.

As we suspect there are common features in the Me^+ and I^+ images, we can use this as an opportunity to test the recoil frame covariance analysis. We can calculate the covariance matrix for either I^+ or Me^+ in the recoil frame of Me^+ or I^+ pointed directly upwards in the image shown. Given that methyl iodide is a linear molecule and the Coulomb explosion should retain that geometry as it explodes, we would expect to see intensity at 180 degrees from the vector which is produced in tandem with the reference ion. Both images have two rings, the inner of which is proposed to come from dissociative ionisation of CH_3I^+, and the outer ring from the Coulomb explosion of CH_3I^{2+} into CH_3^+ and I^+. If the assignment is correct, and the treatment of these images by recoil frame covariance analysis is valid, then the radial component of the covariance intensity should be confined to the outer ring, as the dissociative ionisation doesn't have a co-signal that should be detected in statistical significance.

Figure 5.10 panels a) and b) show the respective covariance matrices for I^+ and Me^+ with the recoil frame of the Me^+ and I^+, respectively, indicated by the white arrow. Both the Cov(Me, I) and Cov(I, Me) images contain features that represent the sample ion images from which they were constructed (which are shown in figures

5.5 and 5.6, respectively. They also have a significant portion of intensity oriented at 180 degrees in the recoil frame. The high intensity feature is at the same radius as the faster feature in both images and there is an absence of any comparable feature associated with the inner, slower feature. The round feature of high intensity at the bottom of the rings in both panels 5.10 a) and b) is what we expected from the recoil frame covariance analysis assuming our assignment of the peaks is correct. The residual features that resemble the original CH_3^+ and I^+ ion images (shown in the left hand panel of figures 5.5 and 5.6) are most likely an artefact. The recoil frame covariance is most effective when the ratio of true coincidences to false coincidences in the data is higher. In an ideal world, the subtraction of the $\langle X \rangle \langle Y \rangle$ is, of course, supposed to account for this uncorrelated data by subtracting off the expectation value for the false coincidences. However, where there are a large proportion of false coincidences, this may break down. The data set upon which these images were based recorded an average of 313 centroided data points per laser shot, which is quite high.

5.3.2 Trifluoroiodomethane

Figure 5.11 shows a preliminary mass spectrum collected following the strong field ionisation of CF_3I. There are a wealth of peaks in the mass spectrum showing that there is significant competition between the dissociation of the C–I and C–F bonds. The molecular orbital diagram for CF_3I is similar to CH_3I with the CF_3 orbitals slightly lower in energy and not worth reproducing. It has the same splitting of the bound p orbitals into a degenerate pair of e symmetry and an a_1 orbital for the spin unpaired electron. The iodine non-bonding orbitals are still the dominant valence orbitals and this is reflected in the mass spectrum as the only 2+ ion observed is iodine and a very small peak for I^{3+}.

The intensity of the CF_2I^+ is much less than the CF_3^+ peak and so we might assert that loss of the iodine from the parent is much more likely. This is in line with chemical intuition which predicts that typical C–F bond strength is much greater than C–I.

Figure 5.12 shows the ion images and respective momentum distributions for the I, CF_3, F and CF_2I fragments which, from the mass spectrum, have been estimated to come from the Coulomb explosions of the parent along either the C–I or C–F bond dissociation channels. As opposed to the CH_3I section, the radial distributions here have only been converted to momentum space rather than TKER. This is because the assignment of a co-fragment is complicated by multiple potential dissociation
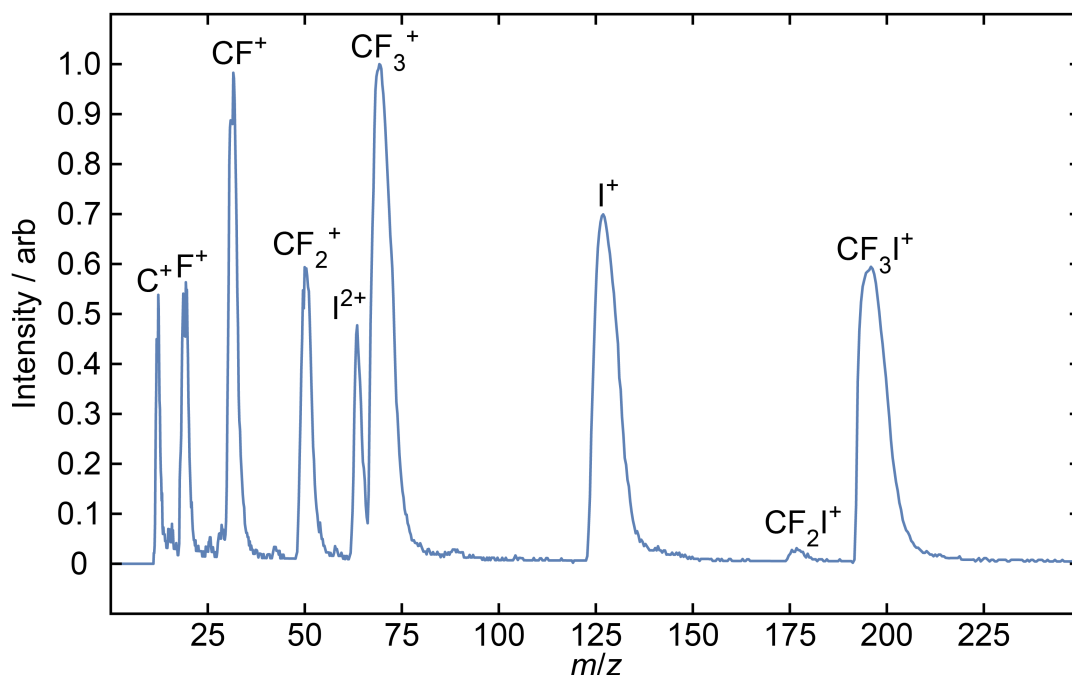
Figure 5.11: Mass spectrum obtained from calibration of TOF spectra measured following Coulomb explosion of jet cooled trifluoroiodomethane by a 33 fs 204 μJ laser pulse centred at $\lambda = 800$ nm. The detector sensitivity is set to high for all photofragments within the figure frame.

channels resulting in significantly different energy disposal. For example, as shown in the previous section, dissociation along C–I from CH_3I will have very similar energy disposal to dissociation along C–I from CH_2I or CHI as the absence of one hydrogen is a negligible difference in the overall mass. However, the difference in dissociation of C–I from CF_3I vs CF_2I or CFI will be much more significant. From the mass spectrum interpretation, the conclusion was drawn that the primary fission channel for the parent ion was $CF_3I \rightarrow CF_3 + I$. Were this the case, there would be a strong match between the momentum distributions of CF_3 and I. As can be seen by comparison between the distributions in figure 5.12 panels b) and c) there is no overlap. However, there is a momentum match between the F and CF_2I products, as shown by figure 5.12 panels a) and d). This is evidence that CF_3I molecules predominantly Coulomb explode through the other primary dissociation channel, along one of the C–F bonds.

There is a significant peak in the CF_3 momentum spectrum to lower momentum release, which must be responsible for the significant peak in the mass spectrum. The only plausible explanation for this in the absence of a momentum matched peak in the I distribution is that it is formed via dissociative ionisation of CF_3I^{1+}. The
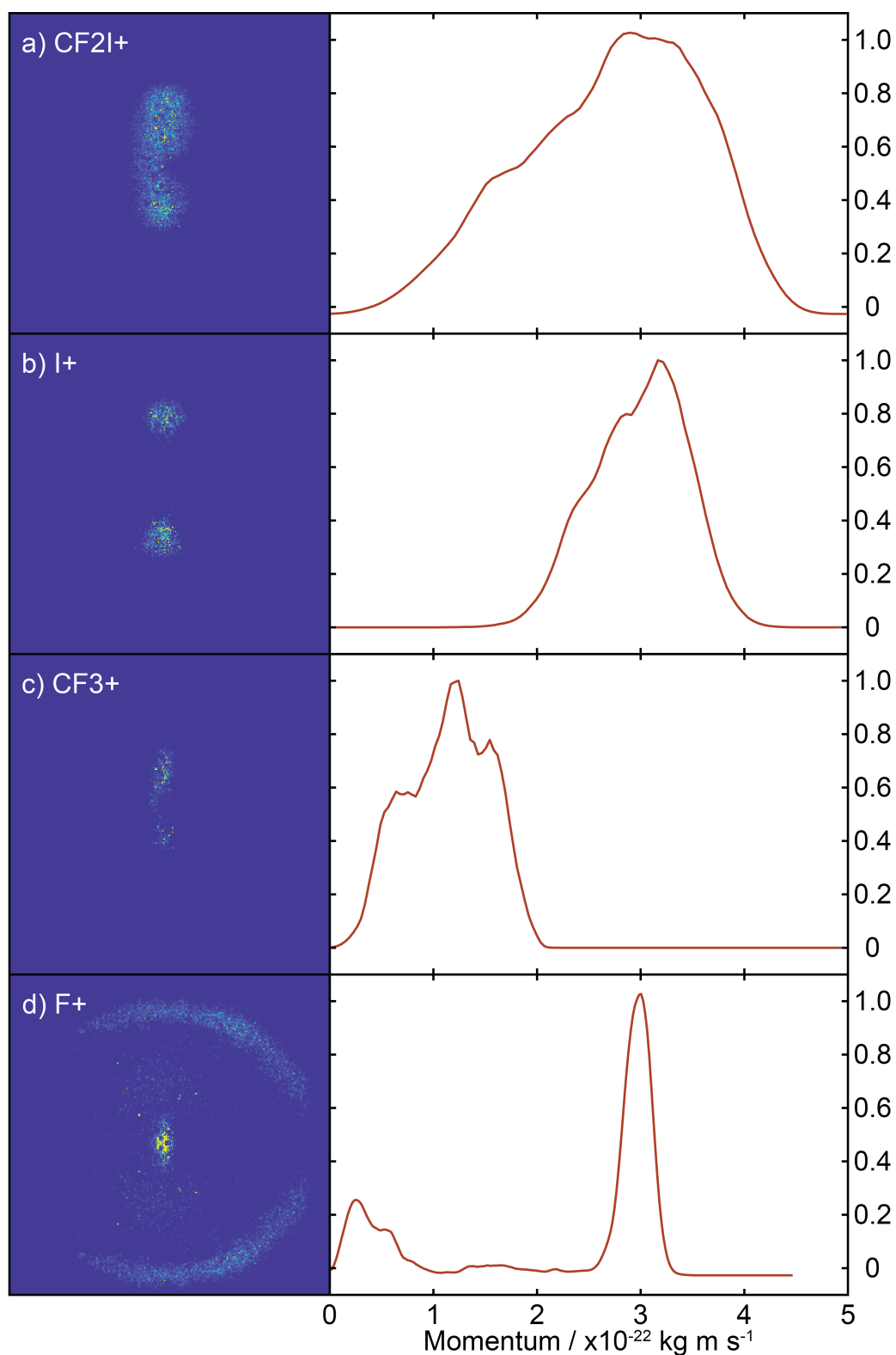
Figure 5.12: The left hand panels show the ion images associated with the m/z 177 (CF_2I^+), m/z 127 (I^+), m/z 69 (CF_3^+) and m/z 19 (F^+) and fragments collected following the strong field ionisation of CF_3I by a 204 µJ 33 fs laser field at $\lambda = 800$ nm. The right hand panel shows the momentum distribution retrieved by integrating the radial distribution of the image over all angles and converting to momentum space.
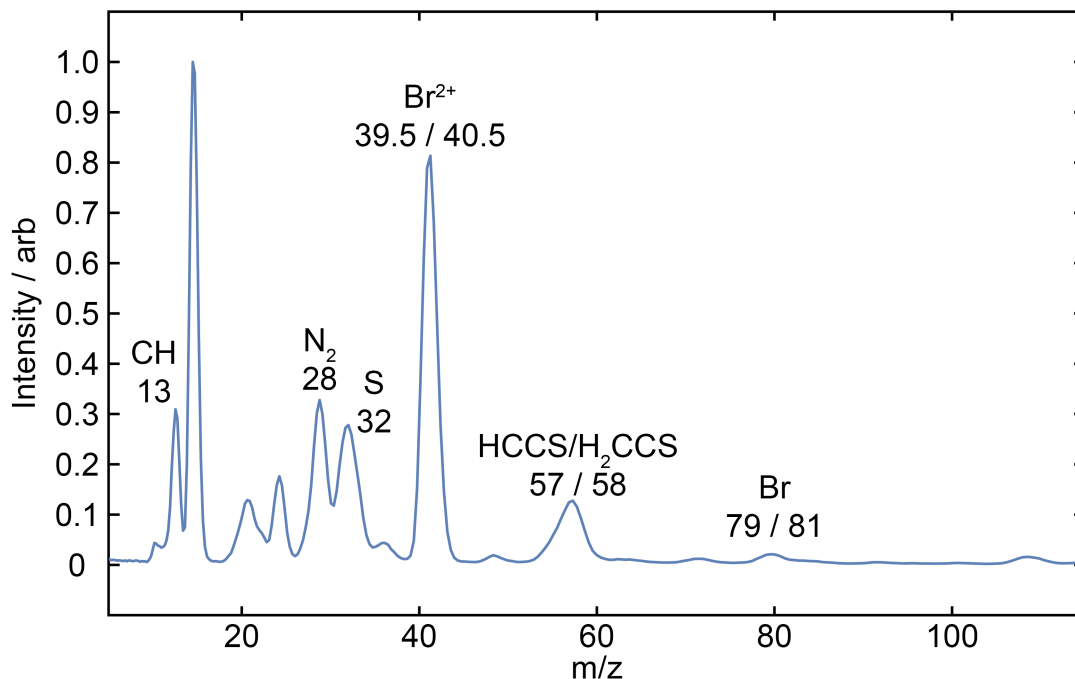
Figure 5.13: Mass spectrum obtained from calibration of the TOF spectra measured following Coulomb explosion of jet cooled 2-bromothiophene by a 33 fs 130 μJ laser pulse centred at $\lambda = 800$ nm.

dissociation dynamics of this species under strong field ionisation look to be quite complex and will only be revealed by examination of all mass peaks. Unfortunately, any other ion images in this experiment have too few data to extract reasonable radial distributions. The background of this data set was that it was a very preliminary one summed over only 2500 laser shots before the experiment had to be discontinued due to issues with the laser. As such it is difficult to draw too many conclusions but this looks to be a promising system with competing Coulomb explosion channels which can be properly characterised by a multi-mass ion imaging experiment. Furthermore, we might speculate that the momentum matching in the I^+ and F^+ TKER spectra, as shown in figure 5.12 b) and d) respectively, implies that three body dissociation to I^+, F^+ and CF_2. It is plausible that following a Coulomb explosion along the C–F bond in CF_3I^{2+}, the resultant CF_2I^+ fragment is formed highly internally excited and fragments along the C–I bond producing neutral CF_2.

5.3.3   2-Bromothiophene

Turning now to 2-bromothiophene which, as discussed in the introduction, is an ideal test case for a system whose photodissociation dynamics are challenging to unveil without Coulomb explosion imaging, figure 5.13 shows a mass spectrum collected following strong field ionisation of ground state 2-bromothiophene using a 33 fs 130 μJ laser pulse at 800 nm. There are a wealth of peaks in the mass spectrum many of which, unfortunately, are attributable to background signal. The broad peak at 57/58 is assigned to a combination of HCCS and H_2CCS and has been previously observed as a possible photofragment product of 2-bromothiophene.[5] The molecular orbital diagram for 2-bromothiophene is not as easily imagined as it is for methyl iodide (or the readily analogous trifluoromethyl iodide) but it is a very reasonable assumption that the non-bonding electrons on the bromine are the most easily ionised valence electrons. The carbon electrons will be further stabilised by the aromatic system, and therefore have much higher binding energies. The sulfur lone pair electrons are also exposed and sit out of the aromatic plane of the ring and so may also be a likely candidate for near valence electrons which might be first ionised.

The mass spectrum gives strong evidence for the bromine being readily ionised as it is the only mass which appears in its doubly charged state at $m/z = 40$. There are clear double peaks at m/z 28 and 32. The peak at m/z 32 is primarily assigned to S^+, and the fast feature in the corresponding ion image (5.14 a) gives credence to this assignment. The peak at m/z 28 is highly likely to be N_2 from background air and, correspondingly, it is likely that there is some contribution to the m/z 32 peak from O_2, with reference again to the m/z 32 ion image, there is a large central feature with little translational energy which is likely to be a manifestation of the O_2 contribution. The features at m/z 14 and m/z 15 are more difficult to assign. The initial impulse is to assign it as a blend of CH_2 and CH_3 respectively though neither of these groups are present in the ring closed form of 2-bromothiophene and so, if this is the correct assignment, they would have to come from a contaminant in the experiment. One other option is that it is a doubly ionised nitrogen molecule, although this seems implausible given the relatively high intensity of the m/z 14 in comparison to the m/z 28 peak.

This preliminary data on 2-bromothiophene were some of the earliest data collected and a crucial mistake was made in the collection, the electric vector of the light was oriented perpendicular to the plane of the detector. Once this was recti-
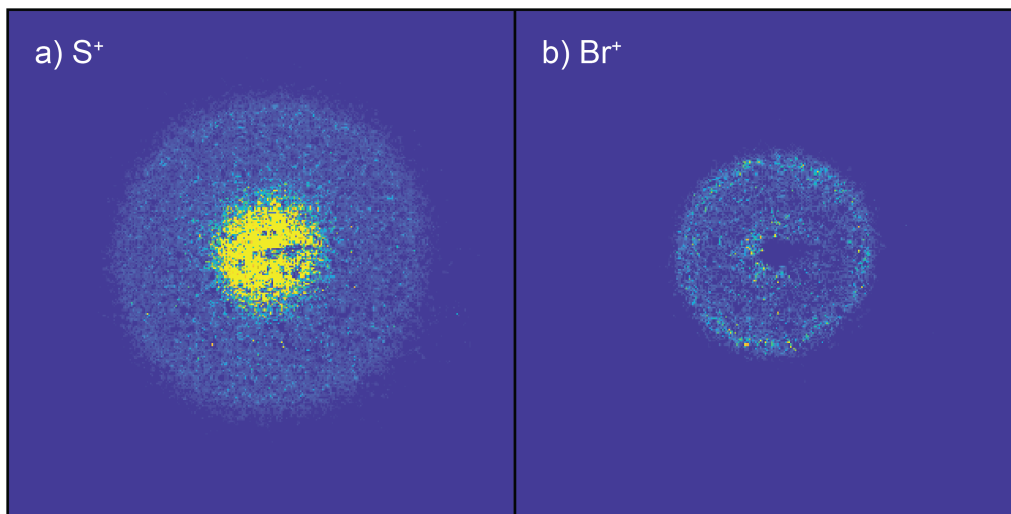
Figure 5.14: Ion images of the a) S^+ and b) Br^+ ions produced by strong field ionisation of jet cooled 2-bromothiophene using a 33 fs 130 μJ light pulse centred at $\lambda = 800$ nm. The electric vector of the light is oriented out of the plane of the image.

fied, a combination of laser issues and the imminent end of this author's time as a PhD student meant that the data could not be retaken in time for inclusion in this thesis. However, the data acquired still contain information that point optimistically to Coulomb explosion imaging holding great promise for probing the dynamics of 2-bromothiophene.

Figure 5.14 shows the ion images for the S^+ and Br^+ fragments following strong field ionisation of jet cooled 2-bromothiophene by a 33 fs 130 μJ laser pulse centred at $\lambda = 800$ nm with the electric vector of the light oriented out of the plane of the image. In strong field ionisation, the 800 nm photons are more likely to interact with molecules in which the most polarisable axis is aligned with the electric vector of the light - as was previously observed in difluoroiodobenzene.[14] In 2-bromothiophene the most polarisable axis lies in the plane of the ring and and pointing between the sulfur and the bromine atoms. Thus with the electric vector of the 800 nm oriented out of the plane, the sulfur and bromine ions can be ejected in any direction in the plane of the image. In accordance with this, the ion images are both isotropic and the dissociation axis is directed into the image. As such, the Newton sphere is not rotationally symmetric in an axis parallel to the plane of the detector and the radial component does not hold any information about the kinetic energy release and thus
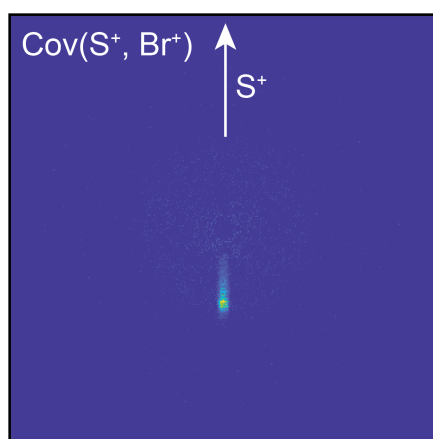
Figure 5.15: Recoil Frame Covariance image of the Br^+ recoiling with respect to S^+ oriented along the arrow pointing towards the top of the image. These are extracted from ion images collected following strong field ionisation initiated by a 33 fs 130 uJ light pulse centred at $\lambda = 800$ nm.

is not analysed further.

Figure 5.15 shows the covariance image for Br^+ in the recoil frame of S^+. Unlike in the comparable recoil frame images between Me^+ and I^+ following strong field ionisation of methyl iodide, there is only the slightest hint of an artefact remaining from the original ion image. The covariance image is not a central dot and, instead is smeared towards the centre of the image. This is consistent with the orientation of the Newton sphere with respect to the detector as the disc type features, where at all radii there will be correlated signal. The positive covariance is exclusively located at the bottom of the image implying that the Br^+ ions preferentially recoil at 180 degrees from the S^+ ions. The angle of covariance at 180 degrees is also consistent with the orientations of the Coulomb exploded molecules. From the perspective of the detector, the molecules will all be oriented with the plane of the ring perpendicular to the plane of the detector. Therefore, as the S and Br ions explode in the plane of the ring, the velocities which will be measured for a truly correlated pair will be 180 degrees from one another - as observed.

5.4 Conclusions

This chapter demonstrates the implementation of a new Coulomb explosion imaging experiment in the Bristol laser group. Three molecular systems have been surveyed, and the capabilities of the PImMS camera have been extended by applying recoil frame covariance analysis, a statistical technique which is only valid when multi-mass imaging. Standard Coulomb explosion imaging enables measurement of the distance between two fragments at the point when the explosion was initiated. The recoil frame covariance enables determination of the angle between two particles enabling more complete structural determination.

While this lays a solid groundwork for future experiments, there are a few aspects which must be tackled first. The level of air contamination must be reduced. Strong field ionisation is completely indiscriminate with respect to which molecules are ionised as opposed to something like a REMPI scheme which is product selective or single photon ionisation which can be semi selective against species with ionisation thresholds higher than the photon energy. As a result, there is significant contribution to the data from unwanted oxygen and nitrogen. Not only can this contaminate any coincident peaks (*e.g* sulfur and molecular oxygen) but can be responsible for signal levels which are damaging to the detector if sustained. This was a significant struggle in trying to collect some of the data for this chapter.

Future ambitions might be to try to refine the experiment by attempting to distinguish 2- and 3-bromothiophene from their recoil frame covariance images. Following this the experiment should be extended to time resolved pump-probe studies with a UV pump photon. Methyl iodide should again serve as the testing ground for checking that the excited state dynamics are being probed and tracked accurately and, following this, the predominance of a ring opening channel in 2-bromothiophene at excitation wavelengths lower than 240 nm might be proven once and for all.

Bibliography

[1] M. N. R. Ashfold, G. A. King, D. Murdock, M. G. D. Nix, T. A. A. Oliver, and A. G. Sage, Phys. Chem. Chem. Phys. **12**, 1218 (2010), ISSN 1463-9076.

[2] F. Zhang, Z. Cao, X. Qin, Y. Liu, Y. Wang, and B. Zhang, Acta Phys.-Chim. Sin. **24**, 1335 (2008), ISSN 1872-1508.

[3] B. Marchetti, T. N. V. Karsili, O. Kelly, P. Kapetanopoulos, and M. N. R. Ashfold, J. Chem. Phys. **142**, 224303 (2015), ISSN 0021-9606.

[4] A. G. Sage, T. A. A. Oliver, D. Murdock, M. B. Crow, G. A. D. Ritchie, J. N. Harvey, and M. N. R. Ashfold, Phys. Chem. Chem. Phys. **13**, 8075 (2011), ISSN 1463-9076.

[5] R. A. Ingle, C. S. Hansen, E. Elsdon, M. Bain, S. J. King, J. W. L. Lee, M. Brouard, C. Vallance, R. Turchetta, and M. N. R. Ashfold, J. Chem. Phys. **147**, 013914 (2017), ISSN 0021-9606.

[6] D. S. Gemmell, Chem. Rev. **80**, 301 (1980), ISSN 0009-2665.

[7] D. S. Gemmell, Nucl. Instrum. Methods Phys. Res **191**, 425 (1981), ISSN 0167-5087.

[8] Z. Vager, R. Naaman, and E. P. Kanter, Science **244**, 426 (1989), ISSN 0036-8075.

[9] Z. Vager, T. Graber, E. P. Kanter, and D. Zajfman, Phys. Rev. Lett. **70**, 3549 (1993), ISSN 0031-9007.

[10] Z. Vager, D. Zajfman, T. Graber, and E. P. Kanter, Phys. Rev. Lett. **71**, 4319 (1993), ISSN 0031-9007.

[11] D. Marx and M. Parrinello, Science **271**, 179 (1996), ISSN 0036-8075.

[12] C. S. Slater, S. Blake, M. Brouard, A. Lauer, C. Vallance, C. S. Bohun, L. Christensen, J. H. Nielsen, M. P. Johansson, and H. Stapelfeldt, Phys. Rev. A. **91**, 053424 (2015), ISSN 1050-2947.

[13] L. Christensen, J. H. Nielsen, C. S. Slater, A. Lauer, M. Brouard, and H. Stapelfeldt, Phys. Rev. A. **92**, 033411 (2015), ISSN 1050-2947.

[14] K. Amini, R. Boll, A. Lauer, M. Burt, J. W. L. Lee, L. Christensen, F. Braue, T. Mullins, E. Savelyev, U. Ablikim, et al., J. Chem. Phys. **147**, 013933 (2017), ISSN 0021-9606.

[15] A. Giusi-Sazor, F. H. Mies, L. F. DiMauro, E. Charron, and B. Yang, J. Phys. B: At. Mol. Opt. Phys **28**, 309 (1995).

[16] A. Rudenko, T. Ergler, B. Feuerstein, K. Zrost, C. D. Schroeter, R. Moshammer, and J. Ullrich, Chem. Phys. **329**, 193 (2006), ISSN 0301-0104.

[17] F. Legare, K. F. Lee, I. V. Litvinyuk, P. W. Dooley, S. S. Wesolowski, P. R. Bunker, P. Dombi, F. Krausz, A. D. Bandrauk, D. M. Villeneuve, et al., Phys. Rev. A. **71**, 013415 (2005), ISSN 1050-2947.

[18] J. Gagnon, K. F. Lee, D. M. Rayner, P. B. Corkum, and V. R. Bhardwag, J. Phys. B. **41**, 215104 (2008), ISSN 0953-4075.

[19] M. Pitzer, M. Kunitski, A. S. Johnson, T. Jahnke, H. Sann, F. Sturm, L. P. H. Schmidt, H. Schmidt-Bocking, R. Dorner, J. Stohner, et al., Science **341**, 1096 (2013), ISSN 0036-8075.

[20] P. Auger, Compt. Rend. **177** (1923).

[21] A. H. Roos, J. H. D. Eland, J. Andersson, R. J. Squibb, D. Koulentianos, O. Talaee, and R. Feifel, Sci. Rep. **8**, 16405 (2018), ISSN 2045-2322.

[22] R. W. Howell, Int. J. Radiat. Biol. **84**, 959 (2008), ISSN 0955-3002.

[23] M. Burt, K. Amini, J. W. L. Lee, L. Christiansen, R. R. Johansen, Y. Kobayashi, J. D. Pickering, C. Vallance, M. Brouard, and H. Stapelfeldt, J. Chem. Phys. **148**, 091102 (2018), ISSN 0021-9606.

[24] M. Burt, R. Boll, J. W. L. Lee, K. Amini, H. Kockert, H. Vallance, A. S. Gentleman, S. R. Mackenzie, S. Bari, C. Bomme, et al., Phys. Rev. A. **96**, 043415 (2017).

[25] F. Allum, M. Burt, K. Amini, R. Boll, H. Kockert, P. K. Olshin, S. Bari, C. Bomme, F. Brausse, B. C. de Miranda, et al., J. Chem. Phys **149**, 204313 (2018).

[26] K. Amini, E. Savelyev, F. Braue, N. Berrah, C. Bomme, M. Brouard, M. Burt, L. Christensen, S. Dsterer, B. Erk, et al., Struct. Dyn. **5**, 014301 (2018), ISSN 2329-7778.

[27] M. E. Corrales, J. Gonzalez-Vazquez, R. de Nalda, and L. Bañares, J. Phys. Chem. Lett. **10**, 138 (2019), ISSN 1948-7185.

[28] A. R. Attar, A. Bhattacherjee, and S. R. Leone, J. Phys. Chem. Lett. **6**, 5072 (2015), ISSN 1948-7185.

[29] M. E. Corrales, R. de Nalda, and L. Bañares, Nat. Commun. **8**, 1345 (2017), ISSN 2041-1723.

[30] A. Nomerotski, S. Adigun-Boaye, M. Brouard, E. Campbell, A. Clark, J. Crooks, J. J. John, A. J. Johnsen, C. Slater, R. Turchetta, et al., Nucl. Instrum. Methods Phys. Res., Sect. A. **633**, S243 (2011), ISSN 0168-9002.

[31] J. J. John, M. Brouard, A. Clark, J. Crooks, E. Halford, L. Hill, J. W. L. Lee, A. Nomerotski, R. Pisarczyk, I. Sedgwick, et al., J. Instrum. **7**, C08001 (2012), ISSN 1748-0221.

[32] A. T. Clark, J. P. Crooks, I. Sedgwick, R. Turchetta, J. W. L. Lee, J. J. John, E. S. Wilman, L. Hill, E. Halford, C. S. Slater, et al., J. Phys. Chem. A. **116**, 10897 (2012), ISSN 1089-5639.

[33] K. Amini, S. Blake, M. Brouard, M. B. Burt, E. Halford, A. Lauer, C. S. Slater, J. W. L. Lee, and C. Vallance, Rev. Sci. Instrum. **86**, 103113 (2015), ISSN 0034-6748.

[34] J. D. Pickering, K. Amini, M. Brouard, M. Burt, I. J. Bush, L. Christensen, A. Lauer, J. H. Nielsen, C. S. Slater, and H. Stapelfeldt, J. Chem. Phys. **144**, 161105 (2016), ISSN 0021-9606.

[35] L. J. Frasinski, K. Codling, and P. A. Hatherly, Science **246**, 1029 (1989), ISSN 0036-8075.

[36] S. L. Miller, L. C. Aamodt, G. Dousmanis, C. H. Townes, and J. Kraitchman, J. Chem. Phys. **20**, 1112 (1952), ISSN 0021-9606.

[37] M. Shapiro and R. Bersohn, J. Chem. Phys. **73**, 3810 (1980), ISSN 0021-9606.

[38] K. Tsukiyama, B. Katz, and R. Bersohn, Chem. Phys. Lett. **124**, 309 (1986), ISSN 0009-2614.

[39] M. Shapiro, J. Phys. Chem. **90**, 3644 (1986), ISSN 0022-3654.

[40] D. Zhang, S. Luo, H. Xu, M. Jin, F. Liu, B. Yan, Z. Wang, H. Liu, D. Jiang, A. Eppink, et al., Eur. Phys. J. D. **71**, 148 (2017), ISSN 1434-6060.

[41] M. E. Corrales, G. Gitzinger, J. González-Vázquez, V. Loriot, R. de Nalda, and L. Bañares, J. Phys. Chem. A. **116**, 2669 (2012), ISSN 1089-5639.

[42] Y. Wang, S. Zhang, Z. Wei, and B. Zhang, J. Phys. Chem. A. **112**, 3846 (2008), ISSN 1089-5639.

[43] H. Liu, Z. Yang, Z. Gao, and Z. Tang, J. Chem. Phys. **126**, 044316 (2007), ISSN 0021-9606.

[44] H. Matsuura and J. Overend, J. Chem. Phys. **56**, 5725 (1972), ISSN 0021-9606.

Chapter 6

Conclusions

6.1 Summary

This thesis explores the implementation of single photon ionisation as a form of universal ionisation, and deals with the opportunities and some of the pitfalls associated with this technique and presents an experiment utilising this to measure competitive bond dissociation in t-butyl methyl sulfide. This reveals significant preference for the dissociation of one bond with respect to another and calculations of potential energy surface cuts are presented in an attempt to rationalise this behaviour.

A Coulomb explosion imaging experiment is then presented and benchmarked by comparison with methyl iodide and trifluoromethyl iodide as a means for determining structure on an ultrafast timescale. This is then applied to preliminary ground state studies of 2-bromothiophene in preparation for experiments which characterise the photoinduced ring opening of thiophenes.

Chapter 3 details the implementation of a single photon ionisation source for multi-mass velocity map imaging and discusses aspects of single photon ionisation that affect how the data is recorded and analysed. The ability to ionise the parent molecule with a single photon was observed to open up a dissociative ionisation channel for the parent molecule which was competitive with the fragments formed by UV photodissociation in terms of yield. Furthermore, the VUV photon was observed to dissociatively ionise the neutral photoproducts such as CH_3S of interest to secondary products HCS and H_2. This pathway is particularly important if one wishes to take advantage of multi-mass imaging's ability to provide quantitative information about the relative yield of photoproducts.

Analysis of angular distributions gathered following single photon show that in

single photon ionisation experiments the ionisation step is sensitive to the alignment of the transition dipole to the electric vector of the light. This is particularly important when the photofragments are formed aligned and care must be taken to ensure the angular distribution is reported correctly. By careful consideration of the dissociation dynamics at play, the enthalpies of formation of species, and by ensuring that the polarisation of the VUV ionisation photons are aligned to maximally sample the photoproduct angular distribution, all these issues can be compensated or corrected for.

Chapter 4 represents a landmark achievement in the study of excited state dynamics where we have successfully measured the preference for one bond to dissociate over another following photoexcitation using a novel method which is extendable to other systems. This builds on seminal work by the group of Fleming Crim[1] in which they measured the preference for O–H or O–D cleavage in HOD by measuring the yield of the OD and OH fragments via laser induced fluorescence. We report a 2:1 preference for cleaving the t-butyl sulfur bond over the methyl sulfur bond in *t*-butyl methyl sulfide following photoexcitation in the wavelength 222.5 - 227.5 nm.

The results are then compared with high level multireference calculations of cuts along the two C–S coordinates of the *t*-butyl methyl sulfide potential energy surface. The calculations show no simple rationalisation for the observed branching ratio. There is no significant enthalpic difference between the two product pairs and neither channel has an obvious potential barrier. The gradients of the potential energy surface along the two bond coordinates are also similar at the point of vertical excitation. Combined, these lead to the conclusion that the preference is most likely due to the degree of non-adiabatic coupling between the dissociative first excited state and the bound second excited state to which the excitation occurs.

Chapter 5 gives a historical overview of the Coulomb explosion process, its expansion to an imaging technique and its application to studying molecular structure. An overview of the Coulomb explosion imaging experimental setup is given which includes a transition away from nanosecond lasers, as used in the single photon ionisation experiments in this thesis, to femtosecond lasers which are capable of reaching the high intensities required for strong field ionisation. The system is benchmarked by studying the methyl iodide and trifluoromethyl iodide molecules which have been thoroughly investigated by CEI in the past. These data are also used as a testing ground for the recoil frame covariance analysis technique as a probe of molecular structure. The technique correctly identifies the 180° angle between the I^+ and CH_3^+

The CEI technique is then applied to 2-bromothiophene in its ground electronic state. The mass spectra reveal that the CEI technique is extremely sensitive to molecular oxygen, presumably due to O_2 being efficiently singly ionised in the strong field regime. Due to O_2 having the same mass as sulfur, this precludes thorough studies of sulfur containing compounds until the level of O_2 contamination in the sample is reduced. However, qualitative experiments were possible and the recoil frame covariance analysis technique was applied, demonstrating that it recovers the ground state structure of 2-bromothiophene.

6.2 Reflection and Future Work

This thesis work set out to address two longstanding problems in chemical dynamics - the quantification of competitive bond dissociation following photoexcitation and implementation of Coulomb explosion imaging for tracking molecular structure on the excited state. Both projects have their successes and failures and both lay a solid groundwork for future investigation.

On the first point, I consider this to be a resounding success in terms of the main goal of quantifying the photofragmentation branching ratios in a manner which is, in principle, extendable to a wide range of molecular systems.

The ability to measure the relative yield of photoproducts opens up a wealth of possibilities for new systems of interest. In the same theme as the *t*-butyl methyl sulfide studied here, thioanisole is a tempting follow up system for further testing of the thioanisole potential energy surfaces which have been thoroughly calculated.[2;3] The conical intersection in thioanisole between the bound first excited singlet state and the dissociative second singlet excited state, as shown schematically in figure 6.1, is located approximately 0.2 eV above the excitation from the ground electronic state to the lowest vibrational level in the first excited state. This is in contrast to the seam of intersection which lies at the same energy as the lowest energy excitation to the near degenerate first and second excited electronic states in t-butylmethylsulfide, also shown schematically in figure 6.1. From this we might expect that there might be stronger dependence of the branching ratio on the excitation wavelength as it is scanned across the energy at which the CI becomes accessible.

The method could also be extended further to include a pre excitation infrared pulse to enhance dissociation along a given bond by pumping an overtone of the stretching vibration of that bond. This has been demonstrated in the past on HOD[4–7]
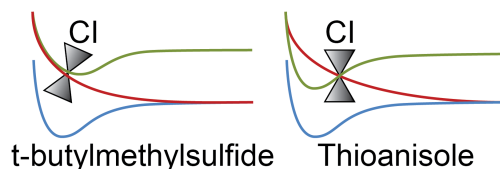
Figure 6.1: Comparison of CIs in thioethers and thioanisole.

and offers a route to controlling the excited state chemistry.

The method could also be applied to the photodissociation of atmospherically relevant molecules. Accurate quantification of the relative yields of radicals following photodissociation is crucial to help quantify and explain the various mechanisms contributing to the observed concentration of these radicals in the atmosphere. An example with relevance to the systems in this thesis might be the role that thioethers play in photooxidation reactions with nitric oxide radicals as shown in scheme 6.1.[8–10]

$$CH_3SCH_3 \xrightarrow{h\nu} CH_3 + CH_3S + NO \rightarrow CH_3SNO \tag{6.1}$$

The implementation of Coulomb explosion imaging was partially successful with a suite of results demonstrating the experiment's ability to characterise the ground state structure of methyl iodide, trifluoromethyl iodide and 2-bromothiophene. The full ambition of this project was to prove that this could be used to chart complex excited state evolution in gas phase photochemical reactions such as photo induced ring opening or photoisomerism. Unfortunately, this goal is yet to be realised but the ground state results hold great promise for being able to differentiate the ground state from the excited state structure in pump-probe experiments. However, there are potential issues. The CEI process is not state selective and so in a pump-probe experiment both the ground and excited state molecules are exploded and detected. Since the fraction of molecules in the excited state is unlikely to be more than a few percent, careful background subtraction will be required to deconvolute the two samples. This will involve recording the background on a shot to shot basis to ensure the signal and background measurements are sampled as similarly as possible. In the workup, the recoil frame covariance images for the signal and background will have to be separately calculated and then the difference taken. This analysis is now beginning to be regularly imlpemented on data collected at cutting edge national facilities.[11]

Extension of this technique to other systems also holds great promise. If ring opening is indeed a viable mechanism in thiophenes it may be active in other heterocyclic systems as well, such as nitrogen or oxygen containing heteroaromatics. These hold

more biological relevance and as such may play a part in the balance of photodamage and photoprotection. Another exciting consequence of a thorough understanding of photo induced ring opening is to be able to exploit it in molecular synthesis, either to expand the ring with new components or to open the ring into a linear linker between moieties. Excited state CEI could also be used to study photoisomerisation between cis and trans alkenes, for example this holds great promise for probing further into the mechanics of vision[12] or for understanding and designing new photoswitches.[13,14]

Bibliography

[1] F. F. Crim, J. Phys. Chem. **100**, 12725 (1996).

[2] Y. Shu and D. G. Truhlar, Chem. Phys. **515**, 737 (2018), ISSN 0301-0104.

[3] S. L. Li and D. G. Truhlar, J. Chem. Phys. **147**, 044311 (2017), ISSN 0021-9606.

[4] R. L. V. Wal, J. L. Scott, and F. F. Crim, J. Chem. Phys. **92**, 803 (1990), ISSN 0021-9606.

[5] I. Bar, Y. Cohen, D. David, S. Rosenwaks, and J. J. Valentini, J. Chem. Phys. **93**, 2146 (1990), ISSN 0021-9606.

[6] R. L. V. Wal, J. L. Scott, F. F. Crim, K. Weide, and R. Schinke, J. Chem. Phys. **94**, 3548 (1991), ISSN 0021-9606.

[7] I. Bar, Y. Cohen, D. David, T. ArusiParpar, S. Rosenwaks, and J. J. Valentini, J. Chem. Phys. **95**, 3341 (1991), ISSN 0021-9606.

[8] D. F. Sheraton and F. E. Murray, **59**, 2750 (1981), ISSN 0008-4042.

[9] H. Niki, P. D. Maker, C. M. Savage, and L. P. Breitenbach, Int. J. Chem. Kinet. **15**, 647 (1983), ISSN 0538-8066.

[10] D. Grosjean and R. Lewis, Geophys. Res. Lett. **9**, 1203 (1982), ISSN 0094-8276.

[11] F. Allum, M. Burt, K. Amini, R. Boll, H. Kockert, P. K. Olshin, S. Bari, C. Bomme, F. Brausse, B. C. de Miranda, et al., J. Chem. Phys **149**, 204313 (2018).

[12] D. Polli, P. Altoè, O. Weingart, K. M. Spillane, C. Manzoni, D. Brida, G. Tomasello, G. Orlandi, P. Kukura, R. A. Mathies, et al., Nature **467**, 440 (2010).

[13] M. Suda, Y. Thathong, V. Promarak, H. Kojima, M. Nakamura, T. Shiraogawa, M. Ehara, and H. M. Yamamoto, Nat. Commun. **10** (2019), ISSN 2041-1723.

[14] M. T. Richers, D. D. Tran, J. Wachtveitl, and G. C. R. Ellis-Davies, Chem. Comm. **54**, 4983 (2018).

Appendix A

Computational Data

Species	Vibrational wavenumbers / cm^{-1}	ZPE / eV
M	3282, 3282, 3103, 1403, 1403, 505	0.80
MS	3106, 3082, 3011, 1472, 1370, 1338, 866, 703, 589	0.95
MSM	3125, 3124, 3107, 3100, 3030, 3028, 1488, 1480, 1473, 1464, 1371, 1346, 1054, 993, 953, 914, 729, 677, 261, 184, 184	2.05
B	3074, 3074, 3069, 3030, 3027, 3027, 2923, 2914, 2914, 1493, 1492, 1489, 1471, 1471, 1469, 1423, 1396, 1396, 1292, 1292, 1093, 1006, 1006, 970, 936, 936, 756, 380, 379, 259, 133, 132, 132	3.12
BS	3110, 3108, 3104, 3087, 3083, 3079, 3022, 3016, 3014, 1515, 1498, 1489, 1487, 1483, 1472, 1428, 1399, 1394, 1213, 1207, 1189, 1019, 992, 970, 934, 921, 792, 576, 385, 370, 363, 289, 274, 259, 234, 222	3.25
BSM	3122, 3117, 3106, 3104, 3099, 3088, 3081, 3077, 3038, 3026, 3019, 3015, 1518, 1504, 1503, 1491, 1489, 1483, 1479, 1467, 1430, 1401, 1401, 1355, 1240, 1236, 1193, 1049, 1040, 972, 971, 967, 938, 931, 806, 707, 570, 418, 401, 361, 315, 300, 271, 266, 225, 214, 175, 62	4.30

Table A.1: Harmonic wavenumbers for the fundamental vibrational modes of the ground states of M, MS, B, BS and BMS used in establishing the zero-point corrections to the absolute and relative dissociation energies reported in Table 1 and the zero-point energies associated with the disappearing modes in the bond fissions shown in figure 4.11.

Appendix B

Derivations

B.1 Time of Flight to Mass Jacobian Transformation

$$t = a\sqrt{m} + b \tag{B.1}$$

$$m = (\frac{t-b}{a})^2 \tag{B.2}$$

$$f(m)dm = f(t) \ dt \tag{B.3}$$

$$f(m) = f(t) \ \frac{dt}{dm} \tag{B.4}$$

$$f(m) = f(t) \ \frac{d}{dm}t \tag{B.5}$$

$$f(m) = f(t) \ \frac{a}{2\sqrt{m}} \tag{B.6}$$

$$f(m) \propto \frac{f(t)}{\sqrt{m}} \tag{B.7}$$

$$\tag{B.8}$$

B.2 Velocity to Energy Jacobian Transformation

$$E = \frac{1}{2}mv^2 \tag{B.9}$$

$$v = \sqrt{\frac{2E}{m}} \tag{B.10}$$

$$\tag{B.11}$$

$$f(E)dE = f(v)\, dv \tag{B.12}$$

$$f(E) = f(v)\, \frac{dv}{dE} \tag{B.13}$$

$$f(E) = f(v)\, \frac{d}{dE}v \tag{B.14}$$

$$f(E) = f(v)\, \frac{d}{dE}\sqrt{\frac{2E}{m}} \tag{B.15}$$

$$f(E) = f(v)\, \frac{d}{dE}2^{\frac{1}{2}}E^{\frac{1}{2}}m^{-\frac{1}{2}} \tag{B.16}$$

$$f(E) = f(v)\, \frac{\sqrt{2}}{2}E^{-\frac{1}{2}}m^{-\frac{1}{2}} \tag{B.17}$$

$$f(E) = f(v)\, \frac{1}{\sqrt{2mE}} \tag{B.18}$$

$$f(E) \propto f(v)\, \frac{1}{\sqrt{E}} \tag{B.19}$$

$$\tag{B.20}$$

Appendix C

Acronyms

AO Atomic Orbital

BO Born-Oppenheimer

CASSCF Complete Active Space Self Consistent Field

CASPT2 Complete Active Space Second Order Perturbation

CCD Charge Coupled Device

CI Conical Intersection

CMOS Complementary Metal Oxide Semiconductor

CSF Configuration State Functions

GTO Gaussian Type Orbital

HF Hartree Fock

LCAO Linear Combination of Atomic Orbitals

LIF Laser Induced Fluorescence

MCP Microchannel Plate

MPI Multiphoton Ionisation

MO Molecular Orbital

MP2 Möller Plesset Perturbation Theory

MRCI Multireference Configuration Interaction

PES Potential Energy Surface

PImMS Pixel Imaging Mass Spectrometry

PTS Photofragment Translational Spectroscopy

REMPI Resonance Enhanced Multiphoton Ionisation

SPI Single Photon Ionisation

STO Slater Type Orbital

ToF Time of Flight

UV Ultraviolet

VMI Velocity Map Imaging

VUV Vacuum Ultraviolet